Understanding the structure–performance relationship of carbon-based photocatalysts by soft X-ray spectroscopy

im

Fachbereich Physik

der Freien Universität Berlin

eingereichte Dissertation

zur Erlangung des akademischen Grades

des Doktors der Naturwissenschaften (Dr. rer. nat.)

vorgelegt von

REN Jian

Berlin, Deutschland

August 2019

Erstgutachter:

Dr. Tristan PETIT

Nachwuchsgruppenleiter im Institut Nanospektroskopie, Helmholtz-Zentrum Berlin für Materialien und Energie GmbH (HZB), Deutschland

Zweitgutachter

Prof. Dr. Holger DAU

Professor des Fachbereich Physik, Freie Universität Berlin, Deutschland

Tag der Einreichung: 27.08.2019
Tag der Disputation: 27.11.2019

The work described in this dissertation was carried out in Helmholtz-Zentrum Berlin für Materialien und Energie GmbH (HZB), and funded by Freigeist Fellowship from the Volkswagen Foundation (No. 89592).

Abstract

Increasing global energy demand drives the development of clean energy sources that will help reduce the consumption of fossil fuels. Solar energy can be converted to chemical energy via artificial photosynthesis but this requires photocatalytic material with low cost and high efficiency. Carbon nanomaterials that can be used either as photocatalysts or as photoabsorbers, have attracted attention as cheap and stable nonmetal nanomaterials with tunable electronic properties. In this dissertation, two typies of carbon nanomaterials, carbon dots and polymeric carbon nitride have been studied with a strong focus on the influences of surface chemistry and heteroatom dopants on their electronic and chemical properties. To this aim, a variety of spectroscopic techniques, with incident energies ranging from soft X-ray, ultraviolet to infrared, have been employed.

The first experimental report on electronic structure of carbon dots studied by synchrotron-based X-ray absorption and emission spectroscopies is presented in this work. The charge-transfer between carbon dots and water has been further studied using *in-situ* X-ray spectroscopy. The modification on the surface chemistry induced by water and the hydrogen bonding environment of carbon dots dispersion have been also probed by *in-situ* infrared spectroscopy. The influence on their fluorescence and photocatalytic applications are then analyzed on the basis of experimental results. For polymeric carbon nitride photocatalyst, particular attention was given to the influence of heteroatoms doping on their electronic structure. Using advanced characterization techniques, the dopant species, and changes of band-gap structure are revealed. Finally, an example of the structure-performance relationship study was presented on highly efficient polymeric carbon nitride photocatalysts.

This research highlights how advanced spectroscopy techniques may open new perspective for deeper understanding of carbon nanomaterials, especially carbon dots and polymeric carbon nitride. Furthermore, promising pathways to achieve more effective carbon nanomaterials for energy applications are also provided.

Zusammenfassung

Der steigende weltweite Energieverbrauch fördert die Entwicklung von sauberen Energiequellen, wodurch der Verbrauch an fossilen Brennstoffen reduziert wird. Durch künstliche Photosynthese kann Sonnenenergie in chemische Energie umgewandelt werden, aber dafür werden preiswerte Photokatalysatoren mit hoher Effizienz benötigt. Kohlenstoffnanomaterialien sind preiswerte, stabile und Metall-freie Nanomaterialien mit durchstimmbaren elektronischen Eigenschaften, die entweder als Photokatalysatoren oder als Photoabsorber genutzt werden können. Für diese Dissertation wurden zwei Familien von Kohlenstoffnanomaterialien untersucht, nämlich sogenannte „carbon dots" und polymerisches Carbonitrid, wobei ein große Aufmerksamkeit darauf gerichtet wurde, inwiefern die elektronischen und chemischen Eigenschaften durch die Oberflächenchemie und die Dotierung mit Heteroatomen beeinflusst werden. Dafür wurde eine Vielzahl an spektroskopischen Methoden angewendet, bei der die Anregungsenergie des einfallenden Lichts vom weichen Röntgenbereich über ultraviolett bis hin zu infrarot variierte.

Diese Arbeit stellt den ersten experimentellen Bericht über die elektronische Struktur von „carbon dots", die mittels Synchrotron-basierter Röntgenabsorptions- und Röntgenemissions-spektroskopie untersucht wurde. Weiterhin wurde der Ladungstransfer zwischen „carbon dots" und Wasser mit Hilfe von *in-situ* Röntgenspektroskopie untersucht. Auch die Veränderungen an der Oberfläche von „carbon dots", die durch Wasser und Wasserstoffbrückenbindungen hervorgerufen werden, wurden mittels *in-situ* IR-Spektroskopie untersucht. Der Einfluss auf ihre Fluoreszenzeigenschaften und photokatalytische Anwendungen wurden auf Basis dieser experimentellen Ergebnisse analysiert. Bei polymerischem Carbonitrid wurde der Einfluss von Dotierung mit Heteroatomen auf die elektronische Struktur genauer untersucht. Mit Hilfe fortschrittlicher Charakterisierungstechniken werden die Dotierungsspezies und Veränderungen in der Struktur der Bandlücke aufgedeckt. Anhand von hocheffizienten Photokatalysatoren aus polymerischem Carbonitrid wurde die Struktur-Performance-Beziehung untersucht.

Diese Doktorarbeit zeigt auf, wie fortgeschrittene Spektroskopiemethoden neue Perspektiven für ein tieferes Verständnis von Kohlenstoffmaterialien eröffnen können, insbesondere von „carbon dots" und polymerischem Carbonitrid. Darüber hinaus beleuchtet sie deren vielversprechendes Potential für Energieanwendungen.

Content

Chapter 1

Introduction

Content

From primitive society, agricultural society, industrial society to the current information age, graphite, carbon black, diamond, carbon fiber, and many other natural or synthetic carbon materials have played important roles in promoting social progress. The continuous advancement of the science and technology has also expanded the family of carbon materials. In the past three decades, fullerenes, carbon nanotubes, and graphene have been consecutively discovered. These carbon nanomaterials and their derivatives have offered new possibilities for the development of materials science and nanotechnology. The outstanding electrical, mechanical and thermal properties, together with the rich abundance in the earth make these carbon nanomaterials become promising candidates for high-performance energy conversion and storage applications.

1.1 Carbon Nanomaterials for Artificial Photosynthesis

1.1.1 General Concept of Semiconductor-based Photocatalysis

With the dramatic increase in fossil energy consumption, the exploration of alternative energy sources and the development of efficient materials for energy conversion and storage are pressing issues. [1] Mimicking the process of natural photosynthesis—capturing the energy from light to convert CO_2 and water into hydrocarbon fuels by photocatalysis or photoelectrocatalysis, artificial photosynthesis has attracted tremendous attention in recent years. [2–4]

Depending on the chemical nature of catalyst, artificial photosynthesis can be classified into different types, such as homogeneous metal complex catalysis, heterogeneous semiconductor catalysis, and enzymatic biocatalysis. [5,6] Among these various types of artificial photosynthesis, the one based on semiconductor photocatalysts shows great potential for practical applications due to the high stability and the recyclability of catalysts, and easy separation of catalysts from substrates. [7–10] In addition, the semiconductor-based photocatalysis is superior to other types of artificial photosynthesis in the efficient absorption of incident light. The light absorption of a semiconductor catalyst is decided by the bandgap between the valence band (VB) and conduction band (CB), which can be flexibly adjusted by modifying the semiconductor. [11]

In general, a semiconductor-based photocatalytic process (**Figure 1.1**) involves the following steps: electrons are excited from VB to CB by absorbing the light with higher energy than the bandgap, then the electrons in the CB and the holes remained in the VB transfer to the catalyst surface, and participate in the redox reactions of the adsorbed species on the surface. [4,12]

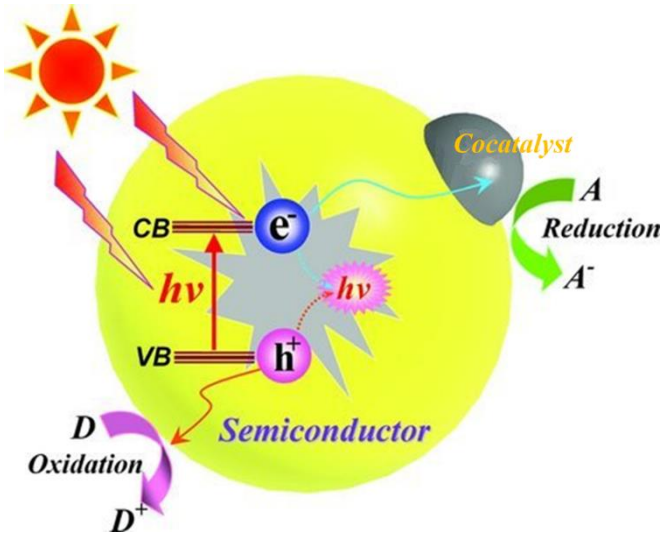

Figure 1.1 Schematic illustration of a typical semiconductor-based photocatalytic process. VB, valence band; CB, conduction band; $h\nu$, light energy. Reproduced with permission from ref. [12], copyright 2012 Wiley-VCH.

Table 1.1 Some typical reactions involved in photocatalytic water splitting and CO_2 reduction. [13]

Reaction	Potential [V, v.s. SHE][a)]	Equation
$2H^+ + 2e^- \rightarrow H_2$	−0.41	1.1
$2H_2O + 2h^+ \rightarrow H_2O_2 + 2H^+$	+1.76	1.2
$H_2O + 2h^+ \rightarrow \frac{1}{2}O_2 + 2H^+$	+0.82	1.3
$H_2O_2 + h^+ \rightarrow \cdot O_2^- + 2H^+$	+1.30	1.4
$\cdot O_2^- + h^+ \rightarrow O_2$	−0.08	1.5
$CO_2 + e^- \rightarrow \cdot CO_2^-$	−1.90	1.6
$CO_2 + H^+ + 2e^- \rightarrow HCO_2^-$	−0.49	1.7
$CO_2 + 2H^+ + 2e^- \rightarrow HCOOH$	−0.61	1.8
$CO_2 + 2H^+ + 2e^- \rightarrow CO + H_2O$	−0.53	1.9
$CO_2 + 4H^+ + 4e^- \rightarrow HCHO + H_2O$	−0.48	1.10
$CO_2 + 6H^+ + 6e^- \rightarrow CH_3OH + H_2O$	−0.38	1.11
$CO_2 + 8H^+ + 8e^- \rightarrow CH_4 + 2H_2O$	−0.24	1.12

a) V, volts; SHE, standard hydrogen electrode.

For photocatalytic water splitting and CO_2 reduction, the main difference is the peculiar surface reactions among the four steps described above. Some possible reactions related to

photocatalytic water splitting and CO_2 reduction are summarized in **Table 1.1**. [13]

Thermodynamically, the alignment between the band edges position of semiconductor and the electrochemical potentials is a prerequisite for determining whether a specific redox reaction can occur. **Figure 1.2** displays the band-edge positions of some typical semiconductors. The semiconductor, which is capable for water splitting, should possess the CB edge more negative than the reduction potential of H_2O (Equation 1.1), and the VB edge more positive than the potential for the H_2O oxidation to O_2 (Equation 1.2–1.5). Similarly, to achieve photocatalytic CO_2 reduction, the CB edge should be more negative than the reduction potential of CO_2 (Equation 1.6–1.12) and the VB edge should also be more positive than the oxidation potential of H_2O. In the case of CO_2 photoreduction, multiple electron transfer reaction involves up to eight electrons and protons to form formic acid, formaldehyde, methanol, and methane. A photocatalytic reaction can be accomplished by using a single catalyst or by a combination of materials such as composites or heterojunctions. In the hybrid photocatalyst consisting of more than one component, the redox potential should be aligned with the individual material's band-edge position. Over the past several years, the materials applied in the field of artificial photosynthesis has also been greatly enriched, not solely confined to the conventional semiconductors (examples shown in **Figure 1.2**), but also extended to novel abundant, metal-free nanomaterials.

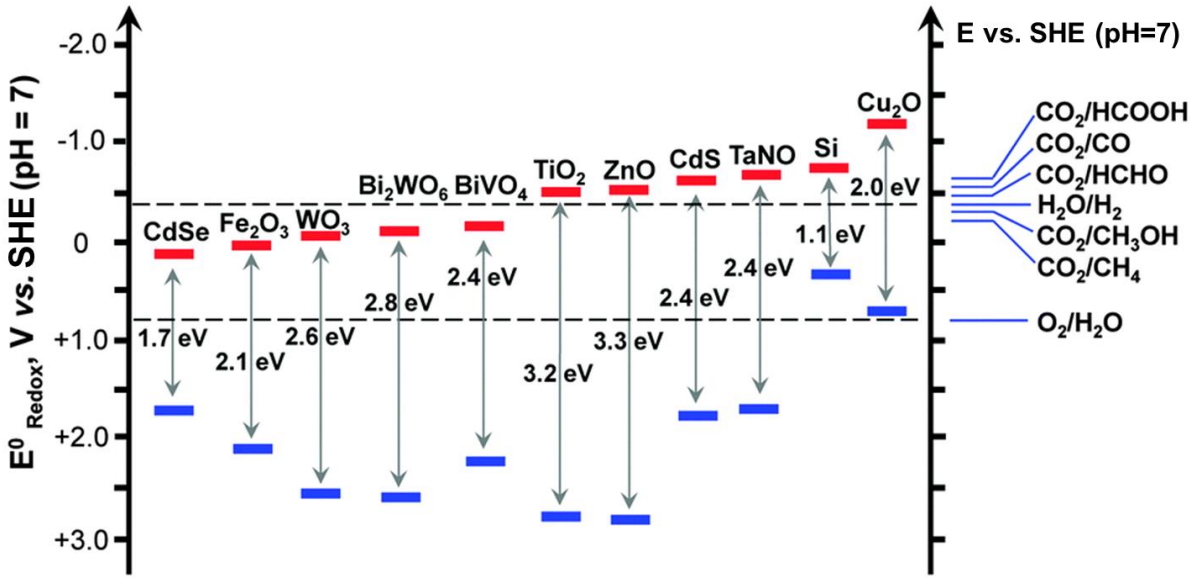

Figure 1.2 Band-edge positions of semiconductor photocatalysts relative to the energy levels of various redox couples. Reproduced from ref. [14] with permission from the Royal Society of Chemistry.

1.1.2 Novel Photocatalysts Based on Carbon Nanomaterials

Carbon nanomaterials are predominantly composed of abundant element carbon and have richly diverse electronic properties. Various carbon nanomaterials, covering a wide range from

0D to 3D nanostructures, have been regarded to have significant roles for artificial photosynthesis. Owing to the superior conductivity and ultrahigh electron mobility, fullerene carbon nanotubes and graphene are always used to form a Schottky barrier junction with semiconductor photocatalysts, where electrons can flow from the semiconductor into the carbon nanomaterials to adjust the Fermi levels. [15] In this case, the carbon nanomaterials play the similar role as the metal cocatalysts loaded on the semiconductor photocatalysts, accumulating the photogenerated electrons, promoting the separation of electrons and holes, and meanwhile enhancing multi-electron reactions. [16–18] Nanodiamond on the other hand, although also a member of carbon nanomaterials family, has a large bandgap that make it possible to utilize deep ultraviolet and induce the photocatalytic reduction. [19]

Among them, with the rise of graphene, the preparation of graphene-based composites for photocatalysis has attracted special attention. In the addition to the advantage mentioned above, its unique two dimensional (2D) conjugated structure and a large theoretical specific surface area (~2630 m^2 g^{-1}), [20,21] make graphene an important building block for the construction of hybrid photocatalysts.

A typical example is TiO_2/graphene heterostructured composite, which have shown in both photocatalytic hydrogen evolution and CO_2 reduction. The first report of TiO_2/graphene hybrid photocatalyst was applied as an efficient photocatalyst for H_2 production, which showed 1.9 times enhancement in the photocatalytic H_2 evolution over TiO_2 by graphene. [22] The high and selective activity for CO_2 photoreduction was realized using the 2D sandwich-like TiO_2/graphene hybrid nanosheets due to the promoted electron transfer from TiO_2 to graphene via Ti–O–C bonds. [23] However, it shows no improvement in the photocatalytic activity of a simple mechanical mixture of TiO_2 and graphene because the photogenerated charge transfer between TiO_2 and graphene is suppressed by the poor contact between graphene and TiO_2. [24] These results suggest that the interfacial interaction between graphene and semiconductor plays an important role for the charge-transfer property in the graphene-based photocatalytic materials.

Nevertheless, graphene's potential application as a semiconductor photocatalyst has been limited because of its metal-like conduction. This problem has stimulated growing interest in synthesizing various derivatives or analogues of graphene that might exhibit desirable physical and electronic properties, including a tunable band structure. Manipulation of the electronic properties can be achieved by tuning the size and dimension, or incorporating dopants.

When 2D nanosheets shrink to 0D nanodots, some different properties starts to emerge, and therefore, the carbon dots (CDs) have added a new perspective to graphene-based

photocatalytic materials. [25,26] For example, the CDs are fluorescent and have an extended visible absorption band, unlike the pristine graphene (can only absorb UV light, λ < 330 nm). [27,28] The unique optical properties endow the CDs' applicability mostly as a photosensitiser to photocatalyst, which will be presented in detail in Section 1.1.3

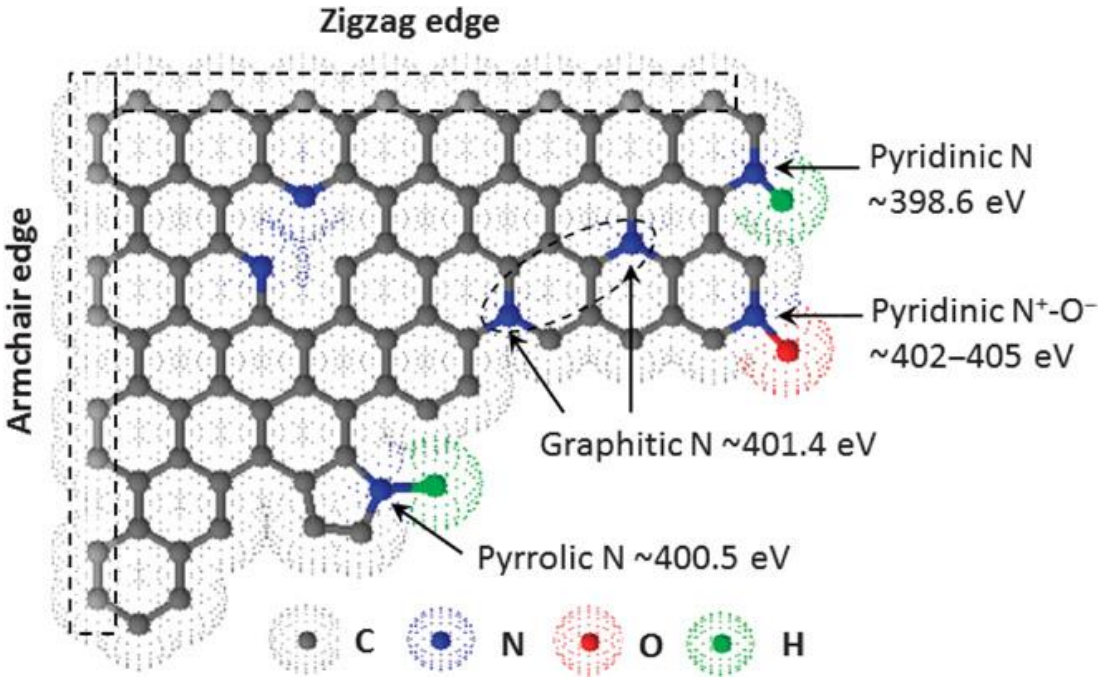

Figure 1.3 Scheme illustration of nitrogen species in nitrogen-containing graphitic carbons. The numbers shown in the figure are the corresponding reported XPS binding energies. Reproduced with permission from ref. [29], copyright from 2015 American Association for the Advancement of Science.

Heteroatom doping strategy actually represents another effective approach to modulate the band-gap of carbon nanomaterials. As a neighboring atom in the Periodic Table, nitrogen is one of the most common dopants applied in carbon nanomaterials, leading to various types of nitrogen species (**Figure 1.3**). In addition to amino and nitro groups, three types of carbon-nitrogen bonds can also be formed upon nitrogen doping. Graphitic N (or quaternary N) is the nitrogen atom bonded with three carbon atoms like the substitution of one carbon atom for nitrogen in the graphene structure. Both pyridinic N and pyrrolic N are bonded with two carbon atoms in a heterocyclic ring, but sit respectively within a hexagon and a pentagon structure. As shown in **Figure 1.3**, graphitic and pyridinic N are sp^2 hybridized and pyrrolic N is sp^3 hybridized. Different types of hybridization of nitrogen atoms would affect the spin charge density and electron configuration of adjacent carbon. Generally, the introduction of nitrogen into carbon nanomaterials leads to improved electrical conductivity and enhanced electrochemical activity.

Polymeric carbon nitride (PCN) has become the most typical representative of metal-

free photocatalyst, which can be considered as an organic graphene analogue possessing a very high nitrogen content dominated by graphitic- and pyridinic-nitrogen. In the section 1.1.4, the study of PCN's application in photocatalysis will be briefly reviewed.

Despite the pristine graphene shows outstanding electronic properties, the fabrication of graphene-based nanocomposites is necessary for most applications. In order to promote the integration with other materials, various chemical functionalities or molecules must be introduced to the graphene's surface. However its low dispersibility in both aqueous and organic solutions restricts the manufacture and processing of graphene-based functional materials. [30] Moreover, the strong van der Waals interactions between pristine graphene nanosheets drive them to form bulk-like agglomerates. [31] Thus, the proper surface modification and passivation of graphene without destroying its electronic structure is crucial, which provides a potential approach to maximize its application, and is also considered definitely feasible for graphene derivatives.

1.1.3 Carbon Dots

Carbon Dots (CDs) commonly refer to a type of 0D carbon nanomaterials with a size less than 10 nm, consisting of a carbogenic core stabilized with ligands and/or surface groups. [32,33] The graphitic, amorphous or polymeric core determines the type of CDs, and the surface chemistry control the colloidal stability and enables subsequent functionalization required for many applications. [34,35] **Figure 1.4** shows four different types of CDs. Polymer nanodots can be regarded as aggregated or crosslinked polymer fragments. [36] Carbon nanodots are always spherical without a crystal lattice, but carbon quantum dots possess obvious crystal lattices. Graphene quantum dots consist of few-layered graphene sheets with a lateral dimension much larger than the height. [26,34] In order to simplify the discussion, the above-mentioned four different kinds of nanosized carbon materials are hereafter collectively referred to as the "CDs".

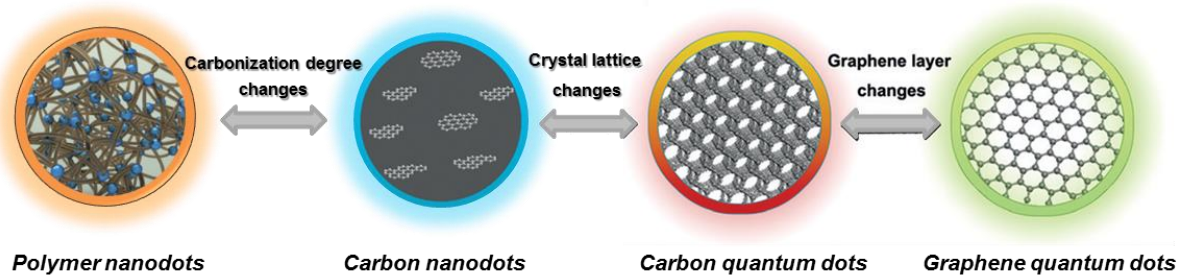

Figure 1.4 Scheme of different CDs. Reproduced with permission from ref. [36], copyright 2015 Wiley-VCH.

Since the first preparation of CDs in 2004, [37] various efforts have been made on

synthesizing high-quality CDs. Generally, CDs can be obtained via two different synthesis routes, "top–down" or "bottom–up". The top–down approach uses electrochemical etching, laser ablation, or arc-discharge to cut bulk carbon nanomaterials into nanosized CDs. [26] This approach can provide CDs with clean surface and high crystallinity and is mainly used to prepare graphene quantum dots. The bottom–up approach uses organic molecules (glucose, citric acid, and ascorbic acid, etc.) or polymers as a precursor to prepare CDs through hydrothermal treatment, alkali/acid assisted ultrasonic treatment or pyrolysis thermal oxidation. [26,33] These "bottom–up" methods usually endow CDs with a rich assortment of surface functional groups, such as oxygen-containing groups, amino-based groups or polymer chains. The physicochemical properties of CDs can be tuned by these surface functionalities, which provides CDs a wide range of applications in biological imaging, [38–40] lighting [41–43] and energy harvesting, [26,44,45] etc. A study focuses on the role of surface chemistry in CDs properties is first shown in **Chapter 3**.

The first report on CDs in photocatalytic application was reported in 2010. [46] In the beginning, the research about CDs for photocatalytic process mainly focused on using CDs to modify the semiconductor, especially making use of their special fluorescence emission. [46–48] CDs with size-dependent photoluminescence and excellent upconversion photoluminescent behavior were prepared using a facile ultrasonic method. [46] The TiO_2/CDs hybrid material was subsequently constructed via sol-gel method. Under visible light ($\lambda > 420$ nm) irradiation, the upconversion photoluminescent emission of CDs can excite TiO_2, which provided the materials with significant visible light activity.

The surface-functionalized CDs are also capable of playing the role as a catalyst to realize the photocatalytic CO_2 conversion under visible light irradiation. [49] Similar with conventional semiconductor-based photocatalytic process, when loading noble metal nanocrystal on the surface of carbon dots to concentrate the photogenerated electrons, the CO_2 photoreduction efficiency could be enhanced. In addition to CO_2 photoreduction, this material can also be applied in photocatalytic H_2 generation.

As introduced previously, nitrogen doping is an effective way to modulate the bandgap between the conduction band and the valence band of graphene derivatives. N-doped CDs are thus capable of being a semiconductor and absorbing visible light. Teng and co-workers realized the N-doped CDs for visible-light driven photocatalytic overall water splitting. [50] The photocatalyst with both n- and p-type conductivities has a bandgap of 2.2 eV, which meets the energy levels requirement for water reduction and oxidation. Under visible light irradiation ($420 \text{ nm} < \lambda < 800$ nm), hydrogen and oxygen evolved steadily and stoichiometrically over a period of 72 hours.

The group led by Prof. Erwin Reisner in University of Cambridge recently reported a facile method to prepare graphitic CDs, with (*g*-N-CD) and without (*g*-CD) core nitrogen doping for photogenerated charge accumulation and facilitating photocatalytic hydrogen evolution reaction. [51] A significant improvement of the photocatalytic performance has been realized using *g*-N-CD compared to undoped CDs due to the enhanced extraction of photogenerated charges. In addition, the graphitized CDs are capable of absorbing more light compared to amorphous CDs (*a*-CD). The physicochemical properties of three CDs were compared using different characterization methods and demonstrated that nitrogen doping in the graphitic carbon core ensures *g*-N-CD to translate the strong absorption of visible light into the enhanced charge separation for efficient photocatalysis. The investigation on their charge-transfer properties to water will be presented in **Chapter 4**.

The research of CDs-based materials is still very young, and offers great promise in various applications. However, further development of these materials requires giving attention to fundamental questions concerning the structure–performance relationship so that they can be designed and optimized for current and future applications. Therefore, CD is chosen as one object of intense research in this thesis.

1.1.4 Polymeric Carbon Nitride (PCN)

Since the pioneering work reported in 2009 on the metal-free photocatalyst, polymeric carbon nitride with visible-light activity by Wang and co-workers, [52–54] it has become a very popular research topic. At first, this yellow-orange powder was named "graphitic carbon nitride" or "*g*-C_3N_4" because a π–π stacking feature ($2\theta = 27.4°$) was observed in the X-ray diffraction pattern. However, with the development in this field, samples with morphological changes from 2D layered structure have been obtained, which shows no observed graphite features. The crystallinity and chemical composition are also not always fixed but variable due to the different syntheses. (**Figure 1.5**) Therefore, in this thesis, the term "PCN" (an abbreviation for polymeric carbon nitride) is used to describe the polymer photocatalysts containing carbon and nitrogen which are synthesized using cyanamide, dicyandiamide, melamine and urea as precursors. [55]

The appropriate bandgap (~2.7 eV) endows PCN with visible light absorption and promising photocatalytic performance, which has been demonstrated in various photocatalytic applications. In the beginning, Wang reported the hydrogen evolution from water in the presence of a sacrificial agent using bulk PCN. [52,53] Then, the PCN has been employed in the field of photocatalytic organic synthesis, for instance, the selective oxidation of alcohols [56] and the aerobic oxidative coupling of amines [57]. As mentioned earlier, the CO_2

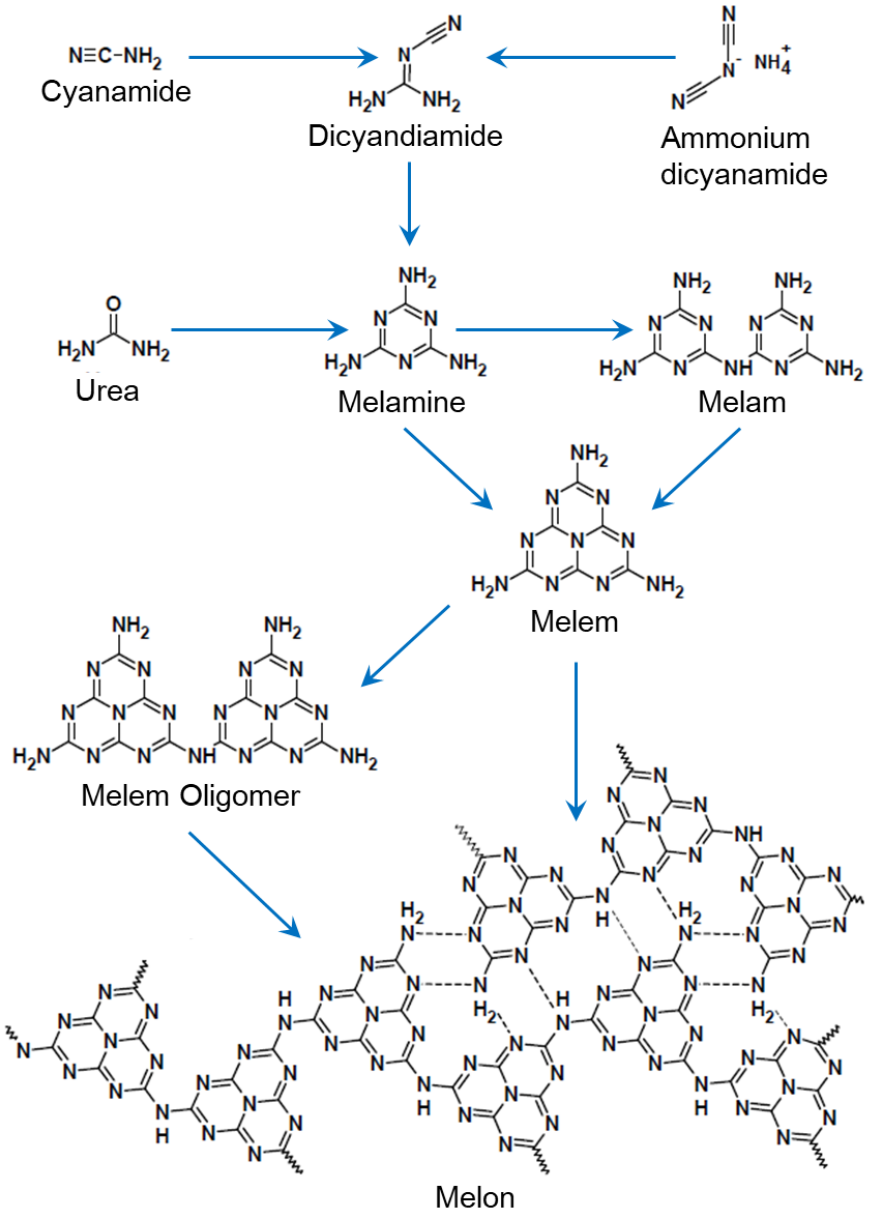

Figure 1.5 Scheme of structural motifs and conversion process for polymeric carbon nitride materials.

photoreduction has gained significant interest as it provides a promising pathway for solar fuel generation. It has also been demonstrated that PCN-based nanomaterials are promising for CO_2 photocatalytic reduction. [58–60] Besides, PCN has also been applied in photocatalytic overall water spitting. [61–63] The incorporation of CDs into the PCN matrix can lead to an increase in the ultraviolet-visible absorption, and thus composite catalyst exhibits impressive stability and performance for photocatalytic water splitting, with quantum efficiencies of over 16% under visible light irradiation, as well as an overall solar energy conversion efficiency of 2%. [44]

Optical, electronic and chemical properties of PCN materials can be influenced by its size, composition and morphology. [64] Thus, the development of various synthetic methods and modification techniques is highly desirable to obtain the optimized PCN photocatalysts.

Among them, modification of the texture and electronic structure by incorporating heteroatoms into the PCN molecules represents an effective approach considering the polymeric nature of PCN and a wide choice of monomers and dopants.

Various anions (e.g. B, F, O, P, S and I) and cations (e.g. K, Fe, Co, Ni, Cu and Zn) have been introduced into the frameworks of PCN via either interstitial or substitutional doping. [55,64] For instance, Fe–N bonds were formed when introducing iron atoms into the PCN molecules. An improvement of photooxidation activity was shown in the Fe doped PCN materials, due to the lowering of the bandgap and broadening of light absorption. [65]

Considering the polymeric nature, the π conjugation, as well as optical and photocatalytic properties of PCN can be modified by polymerizing with structure-matching organic co-monomers. This also provides another way to introduce heteroatoms into PCN matrix. For example, trithiocyanuric acid has a very similar structure with melamine that is a common precursor for PCN preparation and can be used to incorporate sulfur atoms into carbon nitrides. [66] The sulfur doped PCN synthesized through the co-polymerization strategy possesses an extended optical absorption edge and a promoted water oxidation activity. A study on the influence of heteroatoms on the electronic structure of PCN materials will be shown in **Chapter 5**.

As a layered material, the electronic structure and surface performance of exfoliated PCN nanosheets is different from the bulk. Encouraged by exfoliating graphite to graphene, it is expected to obtain PCN nanosheets from delaminating bulk layered PCN. It should be noted that not only the π–π interactions but hydrogen bonds are also disrupted during the exfoliation of PCN.

In 2012, Niu et al. reported a type of PCN nanosheets prepared by oxidation etching of bulk PCN under high temperature. [67] The obtained PCN nanosheets have an ultrathin structure with a thickness of about 2 nm, which is favorable for the electron transfer along the in-plane direction and thus prolongs the lifetime of the photogenerated charge carriers. As a result, the photocatalytic performance of PCN nanosheets is improved greatly. Except for exfoliating from bulk samples, PCN nanosheets can also be prepared by bottom-up approach. Inspired by the roles of phosphates and phospholipids played in the natural photosynthesis, Liu et al introduced K_2HPO_4 into the artificial photosynthesis system and achieved the apparent quantum efficiency of photocatalytic hydrogen evolution over PCN to be 26.1% at the wavelength of 420 nm. [68]

Recently, the group led by Prof. Bin Zhang in Tianjin University reported a new record of visible-light driven photocatalytic hydrogen evolution rate, 20.95 mmol h^{-1} g^{-1}, achieved by the modified atomically-thin porous PCN sheets. [69] The ultrathin PCN nanosheets were

synthesized by a facile one-pot two-step thermal treatment strategy. More details will be shown in **Chapter 6**.

Since PCN was first reported as a photocatalyst with visible-light-activity, it has been almost 10 years. The research of PCN-based materials is still accelerating, and holds a great potential for being robust materials for various photocatalytic reactions. Through the better understanding on the structure and composition, the applications of PCN-based photocatalysts for photochemical energy conversion will be significantly enriched in the near future. Therefore, PCN is taken as the other research object in this thesis.

1.2 Characterization of Carbon Nanomaterials

To further improve the performance of these carbon nanomaterials for the artificial photosynthesis, the understanding of their structural, morphological, and chemical information, the correlation between these characteristics and the activity are both needed. In order to achieve this goal, a wide variety of characterization techniques have been employed to investigate carbon nanomaterials under different conditions.

As introduced above, the carbon nanomaterial is a big family including nanodiamond, fullerenes, carbon nanotubes, graphene, and so forth. It is impossible to review the characterization methods and results that have been obtained to date of carbon nanomaterials in such one short section. In this section, I focus only on carbon dots and polymeric carbon nitride. A brief overview of the basic characterization techniques on these two materials will be first given. Then the drawbacks of these conventional in-house techniques and the demand for advanced techniques are highlighted.

1.2.1 Basic Characterizations of Carbon Nanomaterials

Morphology of carbon nanomaterials, such as the particle size of CDs, the number of exfoliated PCN layers, provides the rich information about the active sites and shows significant impact on the catalytic performance. The most straightforward and commonly employed methods to visualize the morphology of carbon nanomaterials are electron microscopies. Scanning electron microscopy (SEM) focuses on the information of sample's surface and topography. Transmission electron microscopy (TEM) provides more details not only the morphology but also the composition, crystallization with an atomic resolution. Atomic force microscopy (AFM) allows the investigation of materials at nanoscale. For carbon nanomaterials, it is a powerful method to assess their surface topography and estimate the number of graphene or other exfoliated structure due to the ultrahigh sensitivity to the vertical scale.

Ultraviolet–visible (UV–Vis) absorption spectroscopy can be used to measure the transitions in a molecule from its occupied bonding (σ and π) orbitals and non-bonding (n) orbitals to unoccupied (π* and σ*) orbitals. Especially, molecules with conjugated double bonds (like CDs) will have π→π* transitions that fall into the UV–Vis range. In addition, the optical bandgap and light absorption edge of semiconductor photocatalysts can also be measured by UV–Vis absorption spectroscopy, which is of vital importance for the photocatalytic process. Photoluminescence (PL) emission examines the decay from the excited state to the ground state, which is a complimentary technique to UV–Vis absorption spectroscopy. For the photocatalytic process, the electron transfer kinetics and the recombination of electrons with holes can be probed by the PL spectroscopy.

Infrared (IR) spectroscopy and Raman scattering are two types of vibrational spectroscopies and complement each other in identifying the chemical bonding information of carbon nanomaterials. Raman spectroscopy is sensitive to the materials consisting of highly symmetric covalent bonds, and thus is suitable for the characterization on the elemental carbon nanomaterials with uniformed structure, like diamond and graphene. On the other hand, for those carbon nanomaterials with large amount heteroatoms doped (e.g., PCN materials in this dissertation), IR spectroscopy becomes more sensitive. The assignment of some common chemical bonds in CDs and PCN materials are summarized in Table A1 in Appendix.

Another technique to characterize the chemical composition of carbon nanomaterials is X-ray photoelectron spectroscopy (XPS). The high sensitivity to the chemical environment allows it possible to qualitatively compare the atom in different binding sites and quantitatively measure its abundance from XPS measurement. For example, three kinds of C–N species bonds have different bonding energy (**Figure 1.3**) but are not easily distinguished in IR spectrum. Similarly, ultraviolet photoelectron spectroscopy (UPS) uses ultraviolet light to ionize valence electrons, and thus determines the valence band structure of materials. Combination of UV–Vis absorption spectroscopy and UPS results allows estimating the edge position of the electronic bands of photocatalytic materials.

1.2.2 Demand for Advanced Characterization Techniques

As introduced above, conventional in-house characterization tools are well positioned to study carbon nanomaterials for artificial photosynthesis. However, owing to the rich and complex chemical nature, some fundamental technique is not suitable for CDs and PCN materials. An example is the structural characterization of carbon nanomaterials. Powder X-ray diffraction (XRD) is widely available in the laboratory for phase identification, but become powerless for the nanosized structures and the polymeric materials with poor periodicity, like CDs and PCN

studied in this dissertation. It therefore requires other methods for the investigation of such materials. X-ray absorption and emission spectroscopies (XAS and XES) do not, unlike XRD, require long-range order of its objects but are highly sensitive to the local structure. In another word, XAS and XES are capable of providing element-specific probe of amorphous samples in addition to ordered phases. XAS and XES can measure both electronic structure and chemical environment of the absorbing atom.

Similarly, in addition to the above-mentioned XAS and XES, another synchrotron-based soft X-ray spectroscopies, Resonant Inelastic X-ray Scattering (RIXS), can also be used to investigate the electronic and crystal structure, nature of chemical bonds and dynamic transfer processes of charge carriers in photocatalytic materials, especially consisted of light elements such as carbon, nitrogen, oxygen, titanium and iron. [70] The major limitation of the soft X-ray spectroscopies is actually related to the access to the synchrotron sources required to conduct these experiments. The availability of a large range of photon energies (from IR to X-rays) at the synchrotron radiation BESSY II light source is ideal to characterize materials, determining their static and dynamical properties, and exploring their behavior upon light-induced electronic excitation, and the following chemical reactions involving transient reactive species.

Additionally, *in-situ* and *operando* characterizations have attracted increasing attentions. The term "*in-situ*" refers the sample is characterized in the same state as in its application but without exposure to an external condition, while "*operando*" can be considered as a special case of "*in-situ*", where all conditions including the sample state are consistent with the actual operating condition. [71–73] The *in-situ* and *operando* characterization techniques can enrich the understanding of carbon nanomaterials at different scale and time domains, leading to significant insights into the principles of development and functionalization. A typical example of *in-situ* and *operando* characterization of carbon nanomaterials is the employment of attenuated total reflection (ATR) environmental cell in IR measurement that leads to the various approaches for the determination of surface changes under various condition. [74–76] In addition, the recent developments in the flow-cell technique have also offered *in-situ* and *operando* applications to soft X-ray spectroscopy. (see details in Section 2.2.3 and Section 2.4.2) It should be emphasized that the *in-situ* and *operando* characterization is beneficial for investigating a real-world sample, but the data acquisition and interpretation of *in-situ* and *operando* experiments are far more complex, especially in soft X-ray spectroscopy under ultrahigh vacuum conditions. Therefore, *ex-situ* spectroscopic methods will still play a significant role in materials characterization and not be substituted by *in-situ* and *operando* detections.

1.3 Brief Introduction of the Dissertation Structure

As introduced above, carbon nanomaterials are ideal candidates in the field of semiconductor-based artificial photosynthesis, as either photosensitizers or photocatalysts. However, many challenges remain and need to be addressed by a multidisciplinary research force. A challenge of great interest for materials scientists is the design and preparation of optimal photocatalysts with high efficiency. One for chemists is the construction and improvement of a proper reactor for photocatalytic performance evaluation. Another challenge taken up by physicists is the task of providing the microscopic understanding of both materials and reaction process and elucidating the structure–performance relationship of carbon nano-photocatalysts.

In this thesis, we focus on two families of carbon nanomaterials which are of particular interest for semiconductor-based photocatalysis: CDs and PCN. The role of surface chemistry and heteroatoms in their electronic and chemical properties are focused. To this aim, different spectroscopic techniques have been used. And, for each type of sample, the study begins with a general investigation on this material and then shifts to the specific samples that have been used in a photocatalytic process. The general-to-specific pattern can provide more information of CD and PCN materials, not only for photocatalysis but also involving their other applications.

First, in **Chapter 2**, the fundamental principles behind the spectroscopy measurements and the kind of information that can be obtained from the different techniques are introduced at the beginning, followed by a brief description of the experimental methodologies.

Chapter 3 presents a comprehensive study on the surface influence on the chemical, electronic and optical of CDs. This work for the first time shows the experimental results on the electronic structure of CDs materials by utilizing X-ray spectroscopic methods. An *in-situ* study on the hydrogen bonding behavior of different functionalized CDs is also compared by infrared spectroscopy using the environmental cell.

Chapter 4 focuses on the electron transfer between CDs with their surrounding water molecules. Different carbon dots were provided by Prof. Erwin Reisner in University of Cambridge (UK) and their catalytic performance has also been evaluated. The charge-transfer between these samples with water and the structure of the interfacial water around CDs are measured via *in-situ* soft XAS applying a new detection scheme demonstrated here for the first time on nanoparticles.

In **Chapter 5** the effect of various dopants on the electronic structure of PCN materials are studied using XPS, UPS, XAS and RIXS. The bonds formed with dopant and the changes of electronic structure in vicinity of the band-gap are described. Two types of doped PCN

materials, with iron and sulfur, were synthesized by Xinchen Wang's group in Fuzhou University (China).

Chapter 6 presents a study of modified PCN photocatalysts synthesized from a continuous thermal treatment. Prof. Bin Zhang and his colleague in Tianjin University (China) evaluated the photocatalytic activity of these as-synthesized PCN materials and found that the sample with poor light absorption showed the best performance, which seemed counterintuitive and drove us to seek an explanation from spectroscopic study.

In **Chapter 7,** conclusions are summarized, and a brief outlook on possible future studies is given.

Chapter 2

Experimental Methods

Content

As introduced in the previous chapter, the advancement of carbon nanomaterials has been facilitated by novel characterization methods that are capable of investigating materials on various length and time scales. Characterization techniques based on synchrotron X-ray source have played an important role in providing new insights into the materials' electronic and chemical structures with element- and site-sensitivities. In addition, many conventional characterization techniques also exhibit powerful capabilities of studying carbon nanomaterials, such as photoemission spectroscopy and infrared spectroscopy. In this chapter, the theoretical background of these different spectroscopic methods is first briefly described, and then the details of experimental techniques employed in this thesis are highlighted.

2.1 Interaction of Radiation with Matter

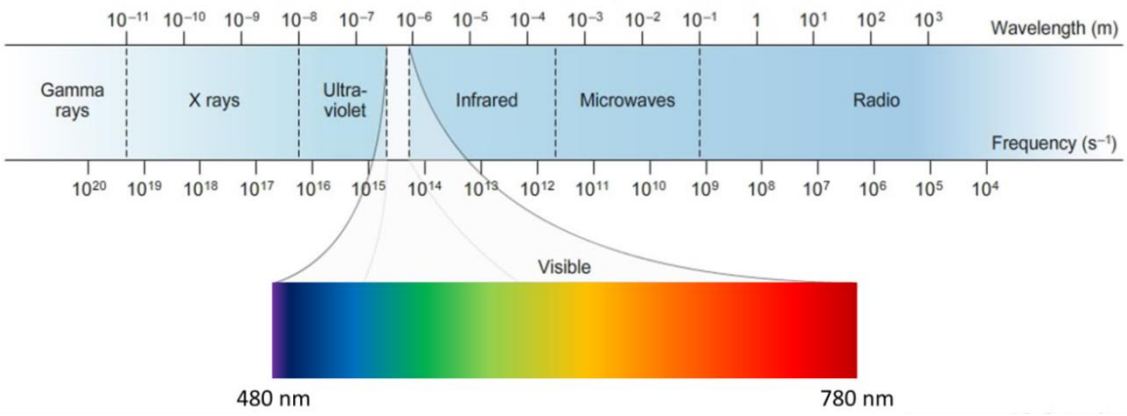

Figure 2.1 Electromagnetic spectrum. The top numbers are the approximate wavelength boundaries of the regions, and the approximate frequency boundaries are listed on the bottom. The visible portion of the spectrum, shown expanded. Adapted from [77], and the permission to use is acknowledged.

Isaac Newton (1643−1727) discovered in 1666 that sunlight could be split into seven colors by a prism and these colors were arranged in a spectrum with a constant order, which opened up the research of light. More than 100 years later, the light was demonstrated as a form of electromagnetic wave propagating at a constant speed by James Clerk Maxwell (1831−1879). The arrangement of different types of electromagnetic radiation in the spectrum was found to be determined by its wavelength λ or its frequency ν, which vary more than ten orders of magnitude from Gamma rays to radio waves as illustrated in **Figure 2.1**. Later, the particle-like properties of the light was also be uncovered. The light can also be regarded as photons. The photon energy E is also a characteristic of electromagnetic radiation, and related to its frequency ν:

$$E = h\nu$$

where h is Planck's constant (6.626×10^{-34} J·s). In addition, the wavenumber $\tilde{\nu}$ indicating the

number of light waves per centimeter, is defined as:

$$\frac{1}{\lambda} \equiv \tilde{\nu} = \frac{\nu}{(c/n)}$$

where c is the speed of light in a vacuum, and (c/n) is the speed of light in a medium with a refractive index n, in which the wave propagate. The wave number represents a unit of radiation energy, as does wavelength. **Table 2.1** shows the characteristics of X-ray, ultraviolet, visible and infrared regions of the electromagnetic spectrum.

Table 2.1 Some electromagnetic radiation mentioned in this dissertation.[a)]

Region	Wavelength [λ, nm]	Energy [E, eV]	Wavenumber [$\tilde{\nu}$, cm^{-1}]	Frequency [ν, THz]
X-ray	0.01−10	1.24×10^{5}−124	1×10^{9}−1×10^{6}	3×10^{7}−3×10^{4}
Vacuum Ultraviolet	10−200	124−6.20	1×10^{6}−50000	3×10^{4}−1500
Near Ultraviolet	200−380	6.20−3.26	50000−26315	1500−790
Visible	380−780	3.26−1.59	26315−12820	790−380
Near Infrared	780−2500	1.59−0.50	12820−4000	380−120
Middle Infrared	2500−50000	0.50−0.025	4000−200	120−6
Far Infrared	50000−1×10^{6}	0.025−0.001	200−10	6−0.3

[a)] Because the limits on the ranges are inexact, some of the boundaries may overlap.

These interactions of radiation with matter define spectroscopy and provide us various methods to study matter. The spectroscope, first invented by Robert Wilhelm Bunsen (1811−1899) and Gustav Robert Kirchhoff (1824−1887) in 1860, [78,79] inaugurated a new era in exploring the microcosm. Depending on the type of interaction with matter, various spectroscopic techniques have been developed. Next, the interaction of X-ray, ultraviolet and infrared radiation with matter will be briefly described.

2.1.1 X-ray Interaction with Matter

In 1895 Wilhelm Conrad Röntgen (1845–1923) reported the discovery of a new kind of radiation generated in a high voltage discharge tube, [80,81] and named it as "X-ray", because of its unknown nature. Today this radiation is well-studied as an electromagnetic radiation with a wavelength ranging from 0.01 to 10 nanometers, and has become an important and powerful basis for various techniques covering a wide application from medical to material science. For the applications in material science, X-ray techniques are widely used for disclosing the electronic and geometric structure of matters owing to the rich interaction between incident X-ray and electrons in matters. The most relevant interaction mechanisms are scattering and absorption.

Compton scattering is an inelastic scattering process resulting in the decrease in energy of the incident X-ray photons. [82] In the scattering process the energy difference of the incident photon and the emitted photon is transferred to the material for excitation of electrons. This effect was first observed by Arthur Holly Compton (1892–1962) in 1923 and further verified by Yui Hsun Woo (1897–1977). [82–84] Compton scattering confirms the particle-like property of light. When the energy of the incident photon decreases, Thomson scattering (also known as Rayleigh scattering) can be observed. Here, a free electron oscillates in response to the electric vector of X-ray and emits a radiation with the same frequency as the incident X-ray. Only the angle of deflection is changed in the process without changing the energy. This phenomenon was first explained by Joseph John Thomson (1856–1940) using classical electromagnetism. Quantum mechanics proves Thomson scattering is the low-energy limit of Compton scattering. This interaction has great significance in the area of X-ray crystallography. [84]

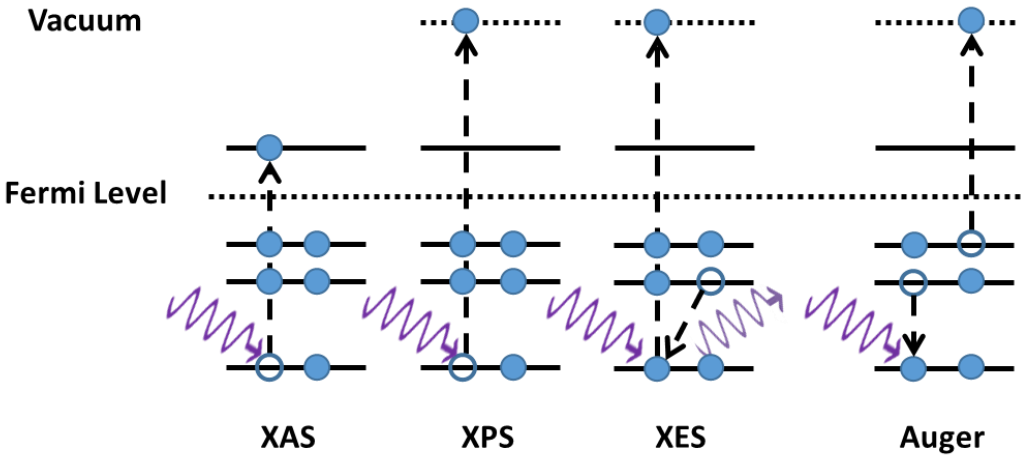

Figure 2.2 Schematic of X-ray absorption process (XAS), photoexcitation of an electron into the continuum (XPS), emission of an X-ray photon upon decay of a valence electron into the core hole (XES) and non-radiative relaxation of the core hole via Auger emission (Auger). Solid and hollow circles respectively present electrons and holes, and only final states are shown. Violet arrows represent X-rays, dashed arrows represent electron excitation and decay.

In addition to scattering, another type of radiation–matter interaction that occurs when the incident photon energy continues decreasing is photoelectric absorption. In this process, an X-ray photon is absorbed by an atom in which the photon may excite the electron from a core level to a valence level or above. If the electron is excited to an unoccupied state in the vicinity of the Fermi level by the incident X-ray, it represents the prototype for X-ray Absorption Spectroscopy (XAS). If the incident photon energy is higher than the ionization energy of the atom, an electron will be ejected with a defined kinetic energy, which is the underlying process

in X-ray photoelectron spectroscopy (XPS). Two competitive processes occur after the X-ray absorption: X-ray fluorescence and Auger electron emission. In the former radiative process, the excited electron releases its excess energy upon relaxation which is carried away by an X-ray photon that can be detected in a typical X-ray Emission Spectroscopy (XES) measurement. In the other non-radiative process, the excess energy is transferred to a secondary electron. The above-mentioned processes are described in **Figure 2.2**. The application of these processes for spectroscopy will be introduced later.

2.1.2 Ultraviolet Interaction with Matter

The early studies that indicated the interaction of ultraviolet (UV) light with matter were performed by Heinrich Rudolf Hertz (1857–1894) and Wilhelm Ludwig Franz Hallwachs (1859–1922) in 1887. [85,86] These experiments demonstrated that negative charge can be removed when a solid is irradiated with UV light. In the following years, these experiments were repeated and finally explained as the "photoelectric effect" by Albert Einstein (1879–1955) in 1905 by introducing the nature of light.

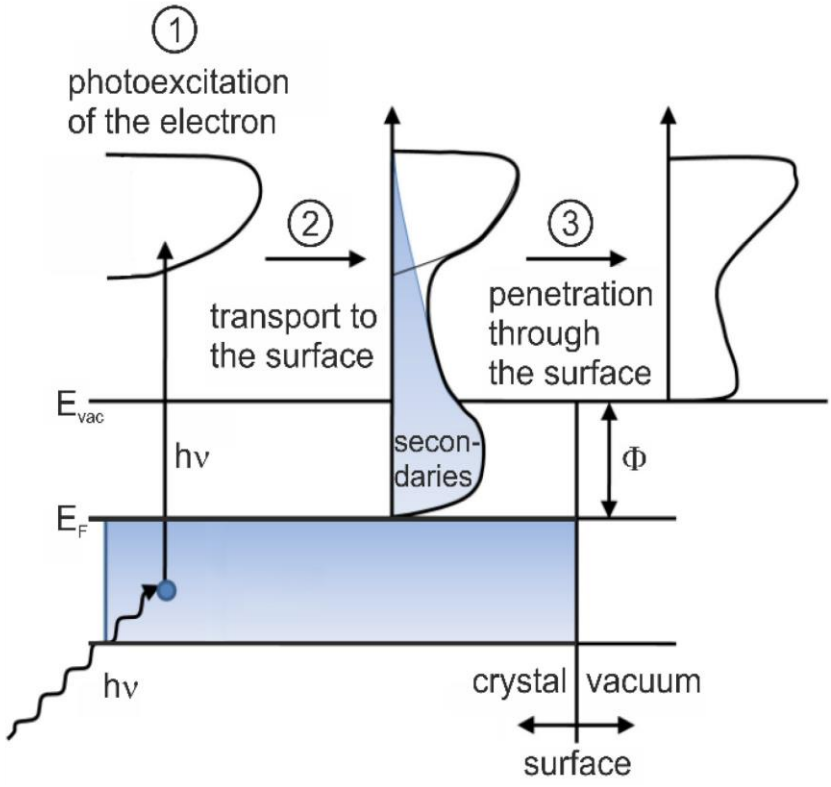

Figure 2.3 Scheme of the three step model descriptions of the photoemission process. Reproduced with permission from ref. [87], copyright 2003 Springer-Verlag Berlin Heidelberg.

When a UV photon is absorbed by matter, photoelectrons and secondary electrons are generated by ionization, similar to the interaction of X-rays with matter described above. When

the energy of the incident UV light $h\nu$ is higher than a certain energy, electrons can be emitted. The minimum certain energy was referred as the work function of the matter, Φ. Therefore, the maximum kinetic energy of the photoelectrons $E_{k,max}$ ideally equals to the energy difference between the photon energy of incident UV and the work function of the work function, [87] i.e.

$$E_{k,max} = h\nu - \Phi$$

The photoemission process can be broken down into the following three steps (**Figure 2.3**): the excitation of a photoelectron, its transportation to the surface and its penetration through the surface into the vacuum. [87]

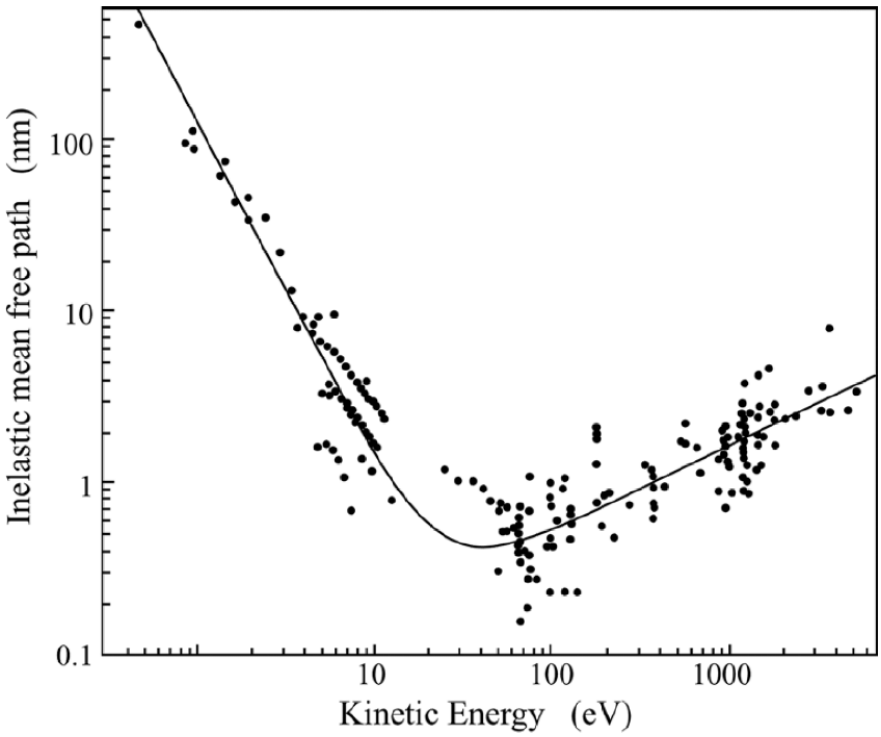

Figure 2.4 Energy dependence of the inelastic mean free path for electrons in a solid. Adapted with permission from [88], copyright 1979 John Wiley & Sons, Inc.

When they transport to the surface, the excited electrons can undergo inelastic scattering, which causes their kinetic energy to decrease. The intensity of primary electrons I_0 decays exponentially with distance and can be described by the Beer–Lambert law, $(d)=I_0e^{-d/\lambda(E)}$, where $\lambda(E)$ is the travelled distance after which the intensity of an electron beam is decayed to $1/e$, which is called inelastic mean free path (IMFP). [87] It only changes with the kinetic energy, regardless of material. For most kinetic energies, the value of the IMFP is in the range of several nanometers (**Figure 2.4**). [88]

When the kinetic energy of the electron is large enough to overcome the work function of the sample, then it can successfully escape the solid. If the photon energy of radiation is not

enough to excite the electron out of the matter, it will excite the electron to higher energy level, which normally occurs with the UV and visible light irradiation. The relevant experimental techniques include ultraviolet photoelectron spectroscopy (UPS), UV-visible absorption spectroscopy and fluorescence spectroscopy, which will be introduced below.

2.1.3 Infrared Interaction with Matter

Infrared (IR) light was discovered by Friedrich Wilhelm Herschel (1738–1822) in 1800 as the first type of invisible light, which has been already well studied and utilized in various fields. The photon energy of infrared is less than 1.6 eV (see **Table 2.1**), which coincides with the transitions between the molecular vibrational levels.

Similar with the previous discussion on the atomic interaction with photons, when a molecule is exposed to an electromagnetic radiation, whose energy exactly matches the difference between two energy levels of the molecule, the molecule can absorb the photons, causing the transition to a higher energy level. However, the coincidence of energy is not sufficient to decide whether the molecular can interact with the absorbed photon but it is also governed by "selection rules" that are based on quantum mechanics and group theory. [89] Therefore, when a molecule interacts with infrared photons, transitions in the molecule can be either allowed or forbidden due to the selection rules, and only allowed transitions give rise to the infrared absorption.

The distribution of charge across the molecule can be changed due to the oscillating electric field generated by the infrared radiation. That the charge differential is multiplied by the distance between the charges defines the dipole moment of a molecule. The molecular vibration must be accompanied by a change in the instantaneous dipole moment. This is because when the dipole moment of the molecular vibration changes, an electric field from the oscillating dipoles is generated and can couple with the external oscillating electromagnetic field at the matching frequency, leading to the energy transfer from the infrared radiation to the molecule. In addition, the greater the dipole moment changes during a vibration, the more easily the photon energy transfer to molecules. The selection rule for the interaction of infrared with molecule is based on the change in the dipole moment of the molecule during the molecular vibration. [89]

According to the selection rule, homonuclear diatomic molecules do not interact with infrared radiation because there is neither permanent dipole moment nor varying dipole moment as the two atoms vibrate. But this does not imply that only asymmetry molecules with permanent dipole moment can interact with infrared radiation. CH_4, a type of tetrahedral molecule, has no permanent dipole moment. But its instantaneous dipole moments are present

when its bonds undergo an asymmetric stretch. Similarly, the dipole moment of CO_2 molecule changes during the asymmetrical stretching vibration and deformation vibration. Therefore, CH_4 and CO_2 are capable of absorbing the infrared radiation due to the molecular vibrations, which makes them significant greenhouse gases.

As discussed above, the interaction of infrared radiation with molecules results in the transition between certain vibrational levels, reflecting the characteristic information of the molecule, which can be utilized as a spectroscopic method for studying molecules. More details can be found in Section 2.4.

2.1.4 Synchrotron Radiation

To control the interaction of radiation with matter and further explore the world invisible to a naked eye, technological developments in advanced light source are required. The synchrotron radiation facility, in particular, is capable of providing electromagnetic waves comprising infrared light, visible light, ultraviolet light, and X-rays. Synchrotron radiation was first predicted theoretically in 1945 by Julian Seymour Schwinger (1818–1994) and then accidentally discovered at a magnetic-induction electron accelerator of General Electric Research Laboratory in the U.S. in 1947. [90] This was the prototype of the first generation of synchrotron radiation sources, which is parasitic on the high-energy collider. The advantages of synchrotron radiation, like great brilliance, high collimation and wide tunability in photon energy, enable it a powerful technique for cutting-edge research in diverse fields. [90] In the field of materials science, synchrotron radiation has been used heavily in the precise characterization of electronic, chemical and geometric properties since the second-generation source became available in the late 1970s. [90] In the past several decades, many novel synchrotron-based characterization techniques have been developed due to the advancement in light source.

When the charged particles move at almost the speed of light in a magnetic field, the charged particles will travel in a curved path and emit synchrotron radiation in the tangential direction of the motion. [90] Synchrotron radiation can be generated at different types of magnetic structures in electron storage rings (**Figure 2.5**). [91] As shown in **Figure 2.5**a, synchrotron radiation covering a broad energy range is emitted at a bending magnet. As novel synchrotron-based techniques emerge, the requirements for the quality of synchrotron radiation are increasing. Various insertion devices have been installed in modern synchrotron facilities, which are comprised of rows of magnets with alternating polarity. The undulator and the wiggler are two commonly used insertion devices. [90] As shown in **Figure 2.5**b, the electron beam wiggles with a small angular divergence through the undulator. As a result, quasi-

monochromatic light with enhanced brilliance can be obtained by the interference effect. [90,91]

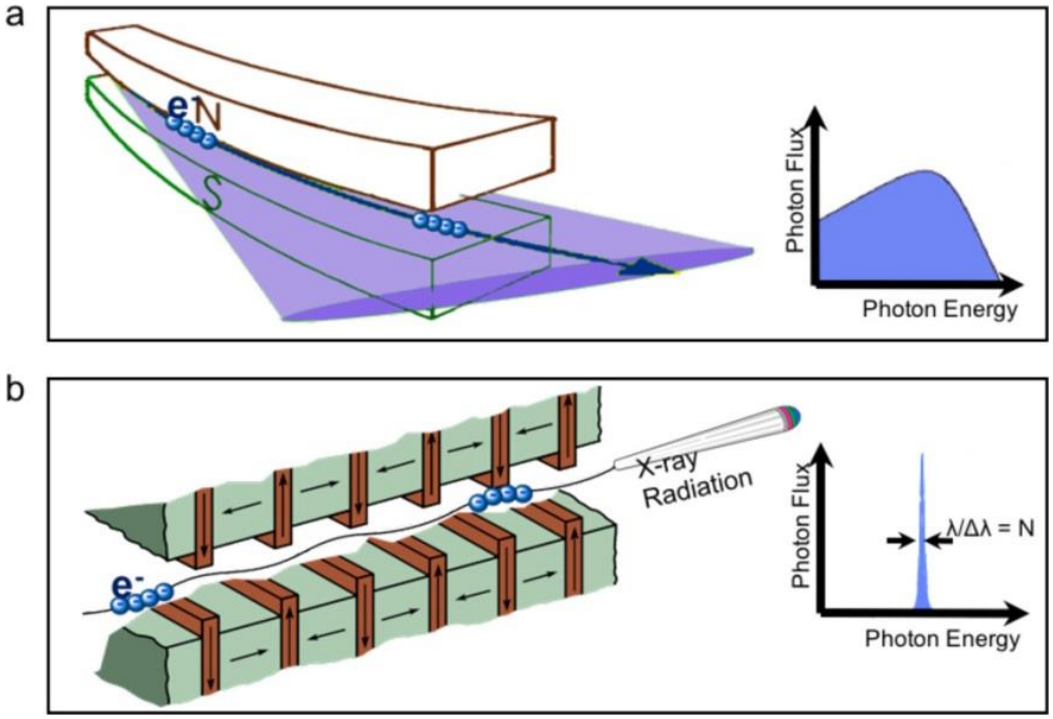

Figure 2.5 Schematic diagrams of the generation of synchrotron radiation by injecting electron bunches into (a) one group of bending magnets or (b) an undulator with a parodic magnetic structure. The corresponding photon energy distribution is shown on the right side of each figure. Reproduced with permission from ref. [91], copyright 2017 American Chemical Society.

Taking the accelerator of the BESSY II, a third-generation synchrotron radiation source, as an example, electrons produced by an electron source are accelerated in a linear accelerator to possess the energy of 50 MeV. Electrons are then injected into a booster ring and are accelerated further to the final energy of 1.7 GeV, reaching near speed of light in vacuum. Electrons enter the storage ring of circumference 240 meters and travel through different insertion devices. As a result, a variety of synchrotron lights with different photon energies are generated and released into different beamlines for experiment using different experimental end station. Currently, 46 beamlines and various experimental stations are available to user operation at BESSY II. The measurements presented in this dissertation were carried out at different beamlines with different end stations, which will be introduced in the following sections.

2.2 X-ray Absorption and Emission Spectroscopy

As introduced in the previous chapter, X-ray absorption and emission spectroscopies investigate both the electronic and atomic structure in the vicinity of a specific atom by

measuring the unoccupied state and occupied states, respectively. These measurements are usually performed at a synchrotron facility due to the requirement of an intense and tunable source of monochromatic X-ray to excite the core electron of the atom. In this section, after an overview of the basic principle of X-ray absorption and emission processes, the major experimental aspects for the understanding of solid materials and liquid samples will be illustrated.

2.2.1 General Principles

As shown in the previous section, the absorption of an X-ray photon of a matter leads to various phenomena depending on the incident energy. In the soft X-ray portion, electrons in the core level can absorb the energy from X-ray photon and be excited to unoccupied states.

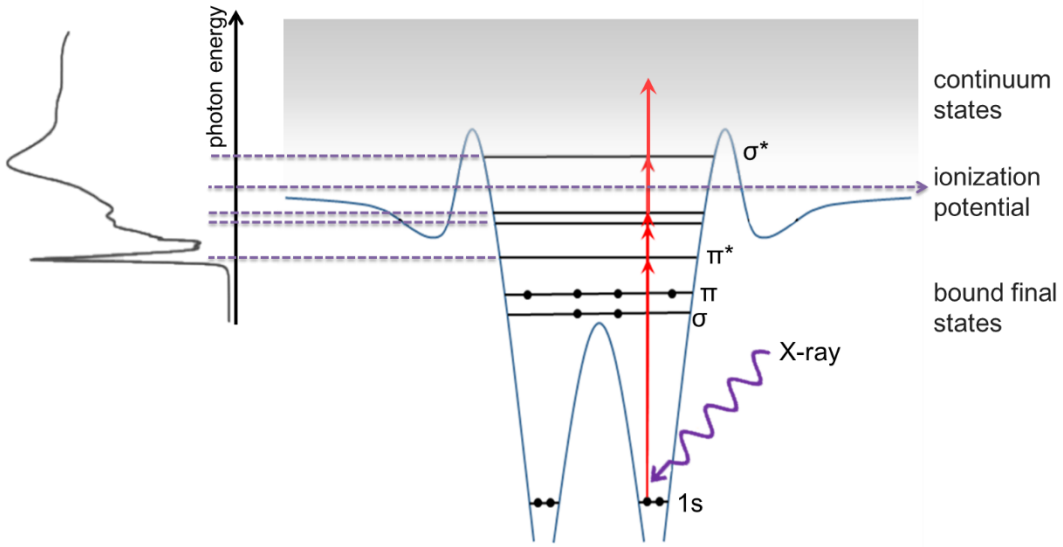

Figure 2.6 Illustration of the principle of X-ray absorption spectroscopy for a diatomic molecule. Upon the X-ray irradiation, a 1s electron is excited to an unoccupied molecular orbital. By measuring this absorption process, the X-ray absorption spectrum (shown on the left) can be thus obtained.

When the X-ray energy scans equal to the ionization energy of a core electron, resonance absorption occurs, leading to a sharp increase of the absorption coefficient. This jump is called an absorption edge, which can be utilized for the element-specific analysis on the materials. **Figure 2.6** depicts the basic principle of XAS with a diatomic molecule as the example. A soft X-ray photon gets absorbed and excites an electron from core level to an unoccupied state. The photon energy of the incident X-ray matches the energy difference between the final and the initial state.

Experimentally, the above process can be visualized by measuring the X-ray absorption coefficient as a function of incident photon energy. The absorption coefficient μ describes the extent to which the intensity of an incident X-ray beam is reduced as it passes through a

material. As indicated by Beer–Lambert law, the X-ray intensity I_t after the beam go through a thickness of sample t is:

$$I_t = I_0 e^{-\mu t}$$

where I_0 is the incident intensity.

This represents the most direct method of measuring the XA spectrum. However, considering the limited penetration depth, transmission measurements are extremely challenging in the soft X-ray regime. In case of carbon nanomaterials studied in this thesis, the attenuation length of soft X-ray is indeed in the submicron range, as shown in **Figure 2.7**, which restricts its application for very thin samples. This requires other methods that directly measure the probability of the generation of a core hole upon X-ray absorption.

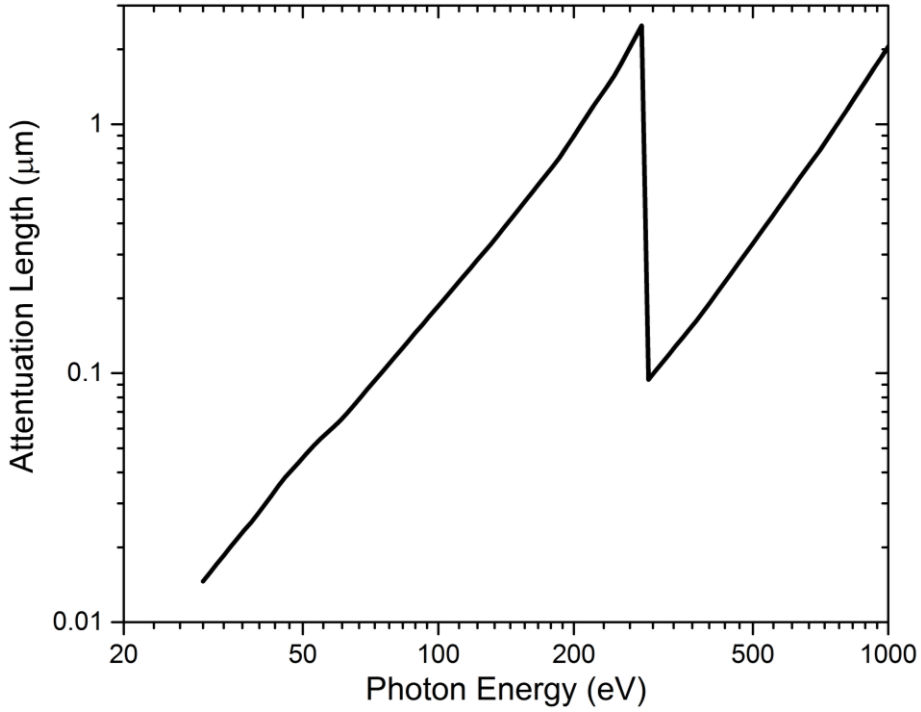

Figure 2.7 X-ray attenuation length for carbon (density is 2.2 g·cm^{-3}) as a function of photon energy at fixed angle, 90°. Plotted using the date from [92].

The final state in the X-ray absorption process is an excited state and will relax by emitting either a photon (radiative decay) or an electron (non-radiative decay). [93] The generated core hole is subsequently filled by an outer shell electron, thus producing X-ray fluorescence. The energy of this outgoing photon equals to the energy difference between the outer shell and the core shell. The fluorescence intensity is directly related to the number of created core hole and is therefore proportional to the absorption coefficient. This detection mode based on the radiative decay is known as the Fluorescence Yield (FY) detection of XAS. Non-radiative (Auger) decay represents as the other major decay channel that an electron from

a higher energy level fills the core hole followed by the emission of a second electron releasing the energy. Electrons emitted from Auger decay can be detected as a function of excitation energy, which is referred as Electron Yield (EY) XAS. The typical depth sensitivity in case of electron yield measurement is given by the escape depth of electrons lying within the range of 2–20 nm, which makes the method strongly surface sensitive. On the other hand FY mode is more sensitive to the bulk structure since the typical depth can be about 100 nm in the soft X-ray region. [93] These two decay processes compete with each other. The relative yields depend on the atomic number *Z*. The Auger decay dominants for light elements over X-ray fluorescence, as shown in **Figure 2.8**.

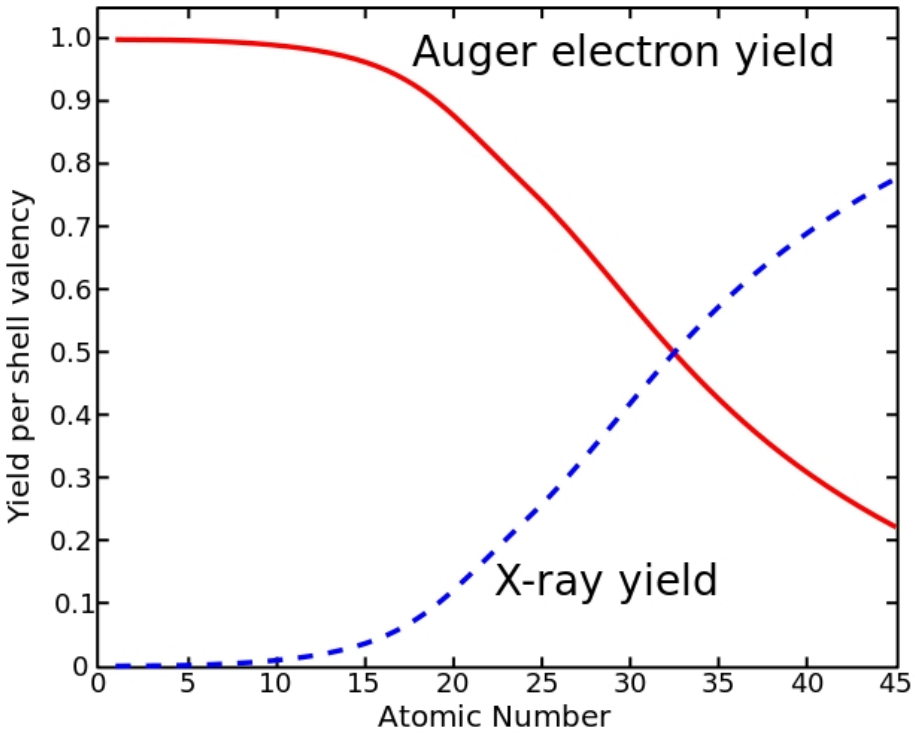

Figure 2.8 Auger electron and X-ray fluorescence yields as a function of atomic number *Z*. In general, the Auger yield is higher for elements with lower atomic numbers while the fluorescence yield increases for elements with higher atomic numbers. Downloaded from [94], and the permission to use is acknowledged.

In both modes, when the emitted photons or electrons of all energies are detected and added up to obtain the X-ray absorption measurement, they are known as Total Fluorescence Yield (TFY) or Total Electron Yield (TEY). When electrons and photons of specific energies are discriminated, the detection mode is called "partial yield". When recording the photons generated upon decaying from occupied states at a fixed excitation, X-ray emission spectroscopy (XES) can be measured and information on occupied electron orbitals of a material is provided.

When there is only one intermediate state in the X-ray emission process, it can be succinctly described by a two-step model, where absorption and emission are considered as two separated processes. It is a good approximation when the electron is excited to a state with sufficiently long lifetime. Practically this can be the case for states significantly above the threshold, leading to the ionization of the molecule, which is shown in the non-resonant X-ray emission process. If several intermediate states exist, the various possible channels would interfere, and then the two-step model is no longer applicable. The emission process cannot be decoupled from the absorption, but has to be treated as a one-step process, which always occurs in resonant X-ray emission process. The intermediate state of non-resonant X-ray emission is the same as the final state of X-ray photoemission, whereas that of resonant X-ray emission is the same as the final state of X-ray absorption. Both non-resonant and resonant X-ray emission processes are second-order optical processes. [70] When the emitted-photon

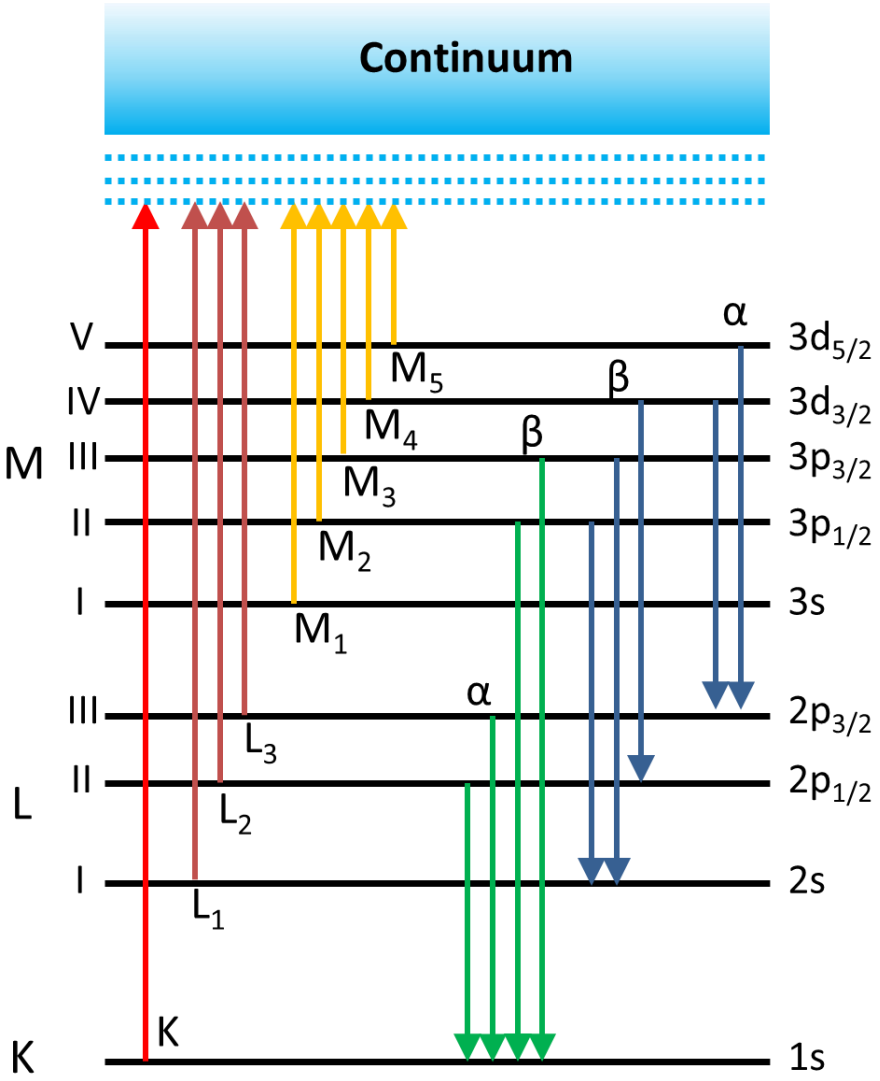

Figure 2.9 Schematic of the electronic energy levels and corresponding notations for X-ray absorption and emission processes. For clarity only three electronic shells (K, L and M) are shown.

energy differs from the incident-photon energy, the resonant X-ray emission spectroscopy is called "resonant inelastic X-ray scattering (RIXS)". [95]

To name the X-ray absorption edges and emission lines used in X-ray spectroscopy, different notations have been proposed. X-ray absorption and emission spectroscopies are core-level spectroscopies; therefore, they can be described using the core electrons involved in the process. In quantum mechanics, the core electrons exist in discrete orbitals, which are classified using the principal quantum number (symbolized **n**). The sets of orbitals with the same principal quantum number are defined as energy levels, which are labelled alphabetically as K (**n** = 1), L (**n** = 2), M (**n** = 3), … according to their distances from the nucleus. X-ray absorption edges are named based on the energy state of the excited electron, for example, the K edge absorption arises from the 1s electrons. This notation, named as X-ray notation, was proposed by International Union of Pure and Applied Chemistry in 1991 to replace the Siegbahn notation. [96] However, the Siegbahn notation is still widely used in X-ray emission process. A scheme of the atomic energy levels and the notions for the X-ray absorption edges and emission lines are shown in **Figure 2.9**.

The more detailed explanations of these soft X-ray spectroscopies are offered by J. Stöhr [93], F. de Groot and A. Kotani [70].

2.2.2 Experimental Solid-state XAS Measurement

Total electron yield (TEY) mode XAS is widely used for solid sample measurement in the soft X-ray range. As discussed previously, after the X-ray absorption, the excited electrons may decay by transferring its energy to nearby electrons. The electrons near the surface can be ejected from the material by gaining energy; consequently net positive charges become available on the sample. The drain current of the sample to ground is measured as the TEY detection.

To obtain a correct spectrum, energy calibration and intensity normalization become very important. For TEY measurements performed at BESSY II, the photocurrent of the last refocusing mirror of the beamline is recorded during each experiment, and is denoted as I_0. Therefore, the presented XA spectra are calculated by: $\mathrm{I} = I_s/I_0$, where the pure sample drain current is assigned to I_s. In addition, the carbon K-edge spectra of the beamline (carbon contamination) was measured using a GaAs photodiode, installed downstream of the monochromator, which can be used for the calibration of the sample carbon K-edge spectra (see Appendix II).

The solid samples measured in this dissertation were always dispersed to form aqueous solution and then drop-casted on a conductive silicon wafer. Then the samples would be introduced onto a copper plate with electrical connections to the Keithley electrometers (Model

6514) that would enable recording the photocurrent for the electron yield measurement. All TEY mode XAS measurements presented in this work were performed using LiXEdrom end station at the beamline U49-2_PGM-1 or UE56-2_PGM-2 at BESSY II. The detailed description of beamlines can be found in references [97,98] and Appendix.

As indicated in the name of this setup, "LiXEdrom", was initially developed for liquid samples, which will be detailed in the following sections.

2.2.3 Experimental Liquid-state XAS Measurement

XAS has been successfully applied *ex situ* on solid materials and can provide detailed information on the local chemical and electronic structures of the excited atom. On the other hand, the electronic structure of materials can be influenced and modified by surrounding solvent environment. Studying the electronic structure of liquid environment and, especially aqueous dispersion of nanomaterials under *in-situ* condition, by soft X-rays has attracted substantial attention in recent years, and is still a great challenge, due to the contradiction between the typically high vapor pressure of the liquid and the strict vacuum requirement for signal detection. [99–101] The liquid flow cell, using membranes to isolate the liquid phase from the vacuum, provides the possibility to investigate liquid samples and nanoparticle dispersions in vacuum with soft X-ray.

In this thesis, two different types of flow cell were employed. One is the flow cell connected with two electrodes connecting to an ammeter enables the ionic yield detection which is applicable in the LiXEdrom station. The cell is made of polyether ether ketone (PEEK) and could be attached to a sample holder with screws and O-ring for vacuum sealing. The membrane that is made of silicon wafer with silicon nitride (Si_3N_4, Silson Ltd., United Kingdom) window was screwed and pressed mechanically against the cell body during operation. Liquid samples flow through the tubes behind the membrane. The membrane (typically 75–100 nm) is coated with Au (10 nm) and Cr (5 nm) was served as the front electrode. The counter electrode is a platinum rod of 1.6 mm diameter. A syringe pump was used to push the liquid during the experiments. The volume of liquid sample are decided by the loop, normally a minimum of 3 mL sample is enough for the measurements. **Figure 2.10** presents the schematic drawing of the liquid flow cell.

Originally, this flow cell was designed for the TFY- and PFY-mode XAS measurements. However, for carbon materials, the fluorescence yield is extremely low (as shown in **Figure 2.8**), moreover most soft X-rays are absorbed by the membrane (or adsorbed carbon contamination) therefore no signal from the samples can be detected. Recently, the new detection scheme by detecting ionic yield for XAS measurement was proposed by Dr. Jie Xiao

et al in HZB, termed as "total ion yield" (TIY), and demonstrated to be bulk-sensitive. [102,103] This provides an opportunity to characterize carbon nanomaterials in liquid state. Further details will be given in Chapter 4.

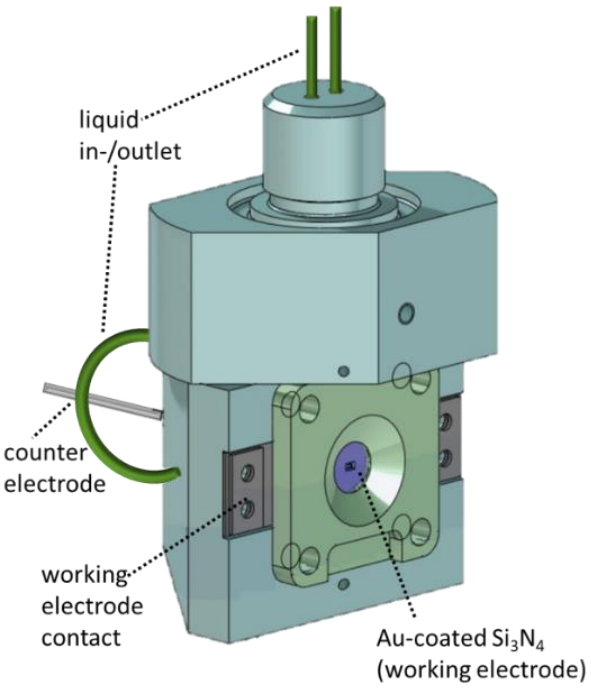

Figure 2.10 Schematic of the flow cell for ionic-current detection for XAS measurement. Adapted with permission from ref. [104], copyright 2019 Wiley-VCH.

The other type flow cell for the liquid measurement applied in this thesis is the transmission cell by detecting the incoming and transmitted X-ray through the liquid sample. At the UVSOR-III synchrotron facility, Dr. Masanari Nagasaka et al. developed such a detection scheme. [105] UVSOR-III, the ultraviolet synchrotron orbital radiation facility, is located in Okazaki, Japan, which is a third-generation light source with a storage ring of 53 meters long and 15 consequent beamlines. [106] The transmission mode XAS were measured at BL3U beamline. More details about the beamline BL3U can be found in the literatures [107] and Appendix.

The transmission-type liquid flow cell is schemed in **Figure 2.11**. The liquid sample is pumped in the tube and flows behind two 100 nm thick Si_3N_4 membranes, which ensures X-ray penetration. The thickness of liquid sample layer can be adjusted from 2000 to 20 nm by changing the helium pressure outside two membranes to optimize the sampling signal. [108] A photodiode detector is applied to measure the transmitted X-ray after the absorption. The calibration of the photon energies at the C and O K-edges made use of gas molecules. [109] The photon energy of the polymer film at the C K-edge is calibrated by the first peak (287.96 eV) of methanol vapors, and that at the O K-edge is calibrated by the O 1s π^* peak (530.80 eV)

for free oxygen molecules, respectively. [108] For the result at C K-edge, the background signal of the membrane recorded with pure water was subtracted from the sample spectra. Under the optimized condition, the energy resolutions at the C and O K-edge are 0.14 and 0.4 eV, respectively.

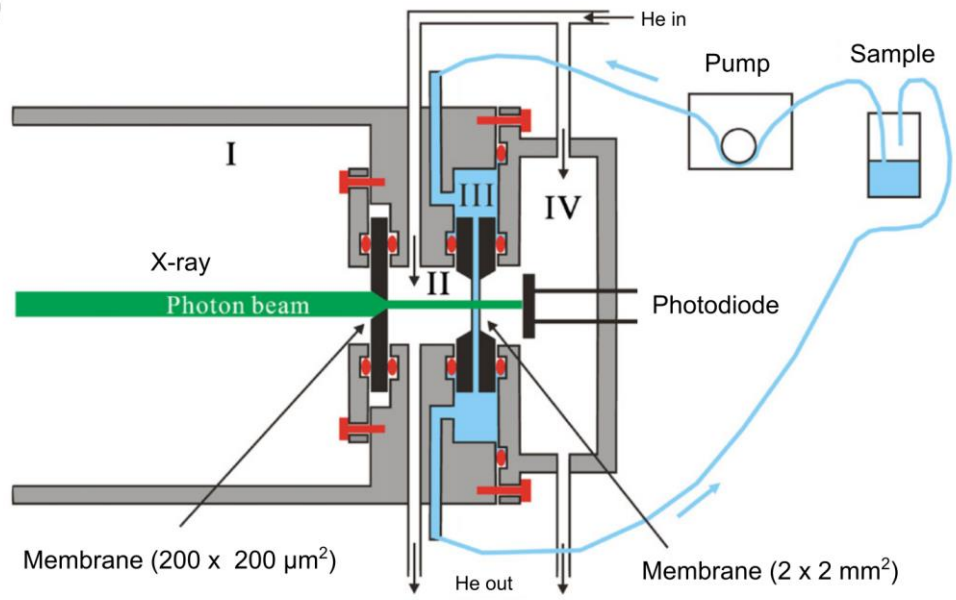

Figure 2.11 Schematic of the transmission cell setup. The transmission-type flow cell is separated into four regions. Incident X-ray is introduced from region I under vacuum and reaches the sample cell after passing through a membrane. By changing the pressure of Helium in region II can adjust the thickness of liquid sample in region III. To measure the transmitted X-ray after the absorption by the sample, a photodiode detector is installed in the region IV filled by helium. Reproduced with permission from ref. [105], copyright 2010 Elsevier.

2.2.4 X-ray Emission Spectroscopy

As stated in the previous section, the X-ray emission was presented as one decay channel after the X-ray absorption process. Since the energy of the emitted photons equals to the energy difference between the occupied states and core holes, the X-ray emission process carries the information about the occupied states. X-ray Emission Spectroscopy (XES) measuring the energy-dependence of the emitted X-ray photons is a technique complementary to XAS and provides information about the local electronic and chemical properties of the occupied states. [70] It is also possible to combine XAS and XES in one spectroscopic technique that is RIXS containing the information of both the incident and emitted photons. In addition, the high-resolution RIXS can also be successfully applied to probe molecular bond vibrations in the ground states. [110–112] In general, the spectral resolution of RIXS is not as high as that of the IR spectroscopy, but is drastically improving due to the advances in instrumentation. [113]

Meanwhile, RIXS is capable of selectively probing a specific subensemble of molecules when measuring at the resonant excitation, which is an advantage over IR spectroscopy. [110] Therefore, RIXS can act as an effective complementary spectroscopic method to IR spectroscopy on investigating the molecular vibrations.

In this thesis, all non-resonant XES experiments were performed using the LiXEdrom end station. The setup consists of a main experimental chamber, a grating chamber and a detector chamber. Different sample holders placed in the main experimental chamber ensure both XAS and XES measurements on liquid or solid samples. The sample manipulator can be moved in three dimensions with micrometer precision to align with the X-ray beam and the detector. In the grating chamber, four different gratings together covering the energy range from 20 eV up to 1000 eV are mounted on a revolver shaped grating holder. [114,115] The detector equipped in the LiXEdrom station consists of a deflection plate, two dimensional multichannel plates (MCP), a phosphorous screen and a charge-coupled device (CCD) camera. [115] For the XES measurements, the sample, the grating holder and the detector lie on the Rowland circle. [115]

The RIXS results presented in this thesis were measured using the PEAXIS end station at the BESSY II which enables Photoemission Spectroscopic (PES), XAS and RIXS studies on materials within the same experimental setup. The PEAXIS experimental station has a sample chamber which is connected to the interaction chamber with a load lock which is used to transport the samples. The sample chamber, the load lock as well as the interaction chamber are kept under ultrahigh vacuum of 10^{-9}–10^{-8} mbar. [116] A commercial hemispherical electron analyzer from SPECS Surface Nano Analysis GmbH is used for electron detection during the PES measurements. The RIXS spectrometer comprises of a grating chamber, a five-meter-long moveable rotating arm for angle dependent RIXS and a CCD detector. [117]

Further details on LiXEdrom and PEAXIS experimental end stations are published elsewhere [114–117] and summarized in Appendix.

2.3 Photoelectron Spectroscopy

Photoelectron spectroscopy (PES) measures the kinetic energies of electrons ejected from materials based on the photoelectric effect. Therefore, the average sampling depth of PES roughly coincides with the IMFP of the electrons in the material. In other words, PES is a surface-sensitive technique. Depending on the different types of excitation sources, PES experiments can be divided into X-ray photoelectron spectroscopy (XPS) and ultraviolet photoelectron spectroscopy (UPS).

2.3.1 X-ray Photoelectron Spectroscopy

In XPS, the absorption of an X-ray photon drives the emission of a photoelectron. The X-ray photons are generated by high-energy electron bombardment of a metallic anode. Aluminum (Al Kα: 1486.6 eV) and magnesium (Mg Kα: 1253.6 eV) are the two most commonly used anode materials.

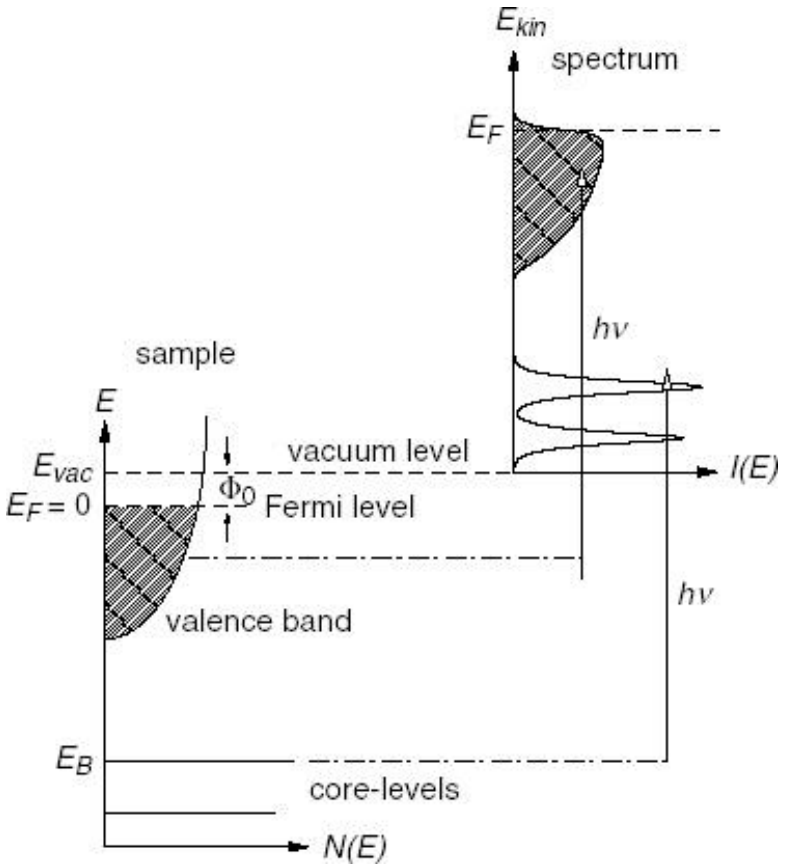

Figure 2.12 Schematic illustration of the photoemission process. Electrons with binding energy E_B can be excited above the vacuum level by photons with energy $h\nu$. Reproduced with permission from ref. [118], copyright 2005 IOP Publishing.

The photoemission process in a sample upon X-ray irradiation is illustrated in **Figure 2.12**. The photon energy of the incident X-ray ($h\nu$) is decided by the source employed in the spectrometer. The kinetic energies of emitted electrons (E_k) can be measured by the analyzer. In addition, the work function Φ of the sample remains consistent with the Fermi level (E_F) of the analyzer if the sample has an electrically conductive contact with the analyzer. Consequently, the binding energies of the emitted electrons (E_B) are determined by using the equation mentioned in Section 2.1.2:

$$E_B = h\nu - E_k - \Phi$$

The above discussion also confirms that a sufficient electrical conductivity of the

sample is necessary for PES measurements. Otherwise, a charge-up of the sample will occur, which can induce artifacts in the observed spectra when studying semiconductors and insulators with poor conductivity.

For a XPS spectrum, the position and the intensity of a peak contain the main information. Because the position of a peak, i.e., the exact binding energy of a core level is very sensitive to the chemical environment and the oxidation state of the emitting atom, the identification of an XPS peak and the quantification of its intensity can be used to determine the species with their relative abundances in the material. [118] For this purpose usually a survey scan is recorded first, then high resolution scans are performed at the different core levels.

In addition to the laboratory-based light source, the use of synchrotron radiation for XPS makes it possible for depth profiling and resonance photoemission with tuning the X-ray excitation energy.

2.3.2 Ultraviolet Photoelectron Spectroscopy

As described above, XPS is a type of core-level spectroscopy, detecting the core electrons due to the high photon energy of incident X-ray. To obtain the complete electron configuration, the description of valence electrons in the outermost energy level is also indispensable. The binding energies of valence electrons are generally between 0 and 15 eV, which can be excited by ultraviolet photons. UPS is a simple tool for investigating the electronic structure of the valence electrons of a material.

A helium gas-discharge lamp is the most commonly available laboratory-based source for UPS measurement, where emitted photons possess energies of 21.2 eV (He I) and 40.8 eV (He II) with a good energy resolution and a high flux. [119] Therefore very fine features in the valence band (or the highest occupied molecular orbital, the HOMO) can be resolved. The primary electrons contain the information about their initial state and thus produce distinct spectral features, where the binding energies of electronic states can be extracted. The binding energy of the valence band maximum (or the HOMO onset) is of interest for semiconductor photocatalysts, which can be used to determine the bandgap structure and decide their photooxidation ability. [119] It should be noted that, UPS probes the total density of occupied states of the molecule, whereas the above-mentioned XES probes the partial density of occupied states of different atoms in the molecule.

Moreover, the onset of the signal stemming from the secondary electrons gives direct information about the work function of the material. If the work function of the detector has been corrected by measuring the kinetic energy of electrons originating from the Fermi-level of a metal, the energy of the secondary electron cut-off (SECO) onset represents the work

function of the sample.

Similar to that in XPS, the synchrotron light (less than 100 eV) can also be employed in the UPS measurement.

2.3.3 CISSY Experimental Station

XPS and UPS experiments in this work were performed using the CISSY setup using the lab-based source. The CISSY consists of three main chambers: load-lock, preparation and analysis chambers, which are kept under ultrahigh vacuum in the order of 10^{-9} mbar or below (**Figure 2.13**). [120] The samples are first placed on a load-lock manipulator, then introduced to the preparation chamber and the analytic chamber. In addition, a sputter chamber and N_2-filled glove box are attached to the setup, allowing the deposition and ambient pressure preparation of chalcopyrite $Cu(In_{1-x}Ga_x)(S_ySe)_2$ (CIS) thin film solar cells. This unique design makes CISSY to be a combination of spectroscopic studies with in-system preparation. The setup can also be used as a mobile end station for the experiments at BESSY II synchrotron. The name of this setup, CISSY, was derived from "CIS" and "synchrotron". [120]

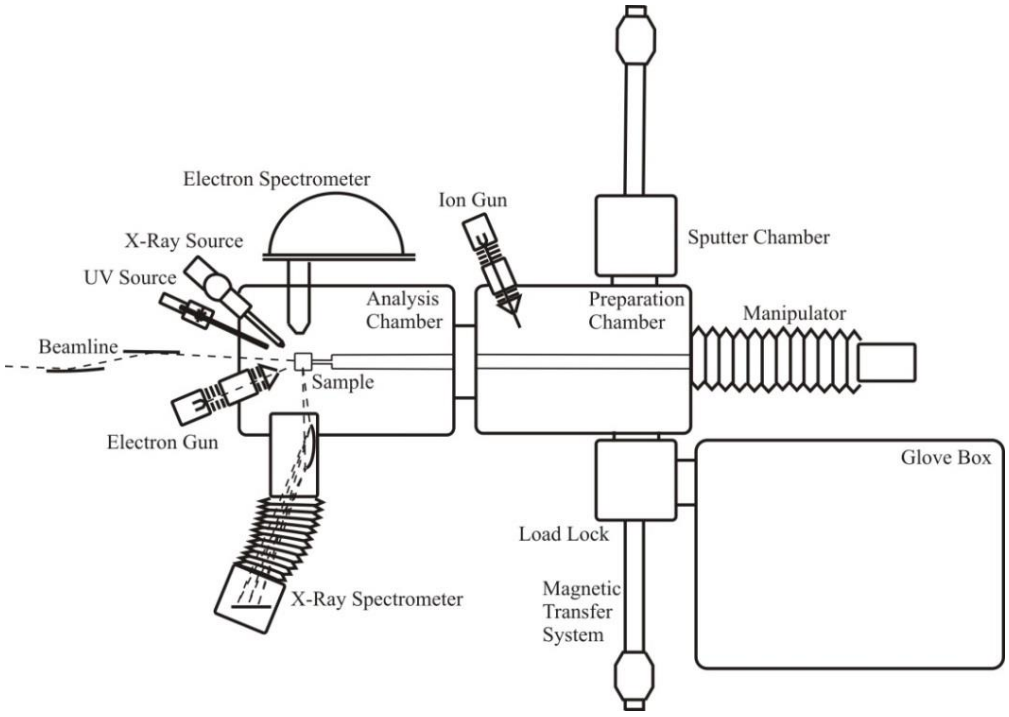

Figure 2.13 Schematic drawing of the CISSY setup. Downloaded from [121], and the permission to use is acknowledged.

To realize the spectroscopic characterization of materials, two radiation sources, an XR 50 X-ray source and a UVS 10/35 UV source from SPECS Surface Nano Analysis GmbH and a CLAM 4 photoelectron analyzer from VG Scienta GmbH are equipped with the CISSY. [120] The XR 50 X-ray source is equipped with two different anodes (Mg Kα at 1253.6 eV and Al

Kα 1486.6 eV) for XPS experiments. For UPS measurement, photons with two different energies can be emitted from the UVS 10/35 UV source: He I 21.2 eV and He II 40.8 eV depending on the gas pressure inside the lamp.

All XPS and UPS shown in this thesis were respectively measured using Mg Kα radiation and He I as excitation source. The analyzer of the spectrometer was calibrated using pure gold. All samples were thin film on Si wafer drop-casted from aqueous dispersion. The pass energies of XPS and UPS measurement were set to be 20 eV and 5 eV, respectively. C, N and O 1s XPS spectra were fit to a Gaussian–Lorentzian peak (30% Gaussian) after a Shirley-type background subtraction to determine their exact binding energies.

2.4 Infrared Spectroscopy

As discussed in Section 2.1.3, the vibrations corresponding to a variation in the dipole moment in the molecule will lead to an absorption band in the Infrared (IR) region. Observed IR absorption bands in samples can allow access to information on the nature of present vibrational modes, chemical composition, bonding lengths and strengths, as well as the angles of chemical groups, existing hydrogen bonding networks, and the conformation of the molecule. IR spectroscopy is therefore useful for the studies of molecule. The *in-situ* IR measurements can be applied in the qualification and quantification of different species due to the chemical environment changes.

2.4.1 Vibration Transition and Infrared Absorption

Atoms in a molecule above the temperature of absolute zero are in motion around their equilibrium positions, which lead to the molecular vibration. The vibration in a diatomic molecule represents the simplest type of molecular vibration. Such vibration occurs when the bond between two nuclei stretches or compresses, which can be simplified using the harmonic oscillator model. The potential energy E of an ideal harmonic oscillator is described in classical mechanics as:

$$E = \frac{1}{2}k(r - r_e)^2$$

where k is the force constant measuring the strength of the bond between two nuclei, and r is the distance between two nuclei after deviating from the equilibrium bond distance r_e.

However, real molecular vibrations are more complicated. To accurately understand the molecular vibration of real molecules, quantum mechanics are required. When applying the quantum mechanics to the ideal harmonic vibration, the vibrational potential energy E can also be expressed with the vibrational quantum number v:

$$E = h\nu_0(v + \frac{1}{2}),\ v = 0, 1, 2, \ldots$$

where h is the Planck's constant, and ν_0 is the fundamental frequency of the particular mode. Therefore, the vibrational energy of ground state (v=0) is $\frac{1}{2}h\nu_0$, that of first excited level (v=1) is $\frac{3}{2}h\nu_0$, and so on. The vibrational energy levels in this case are distributed evenly. [122]

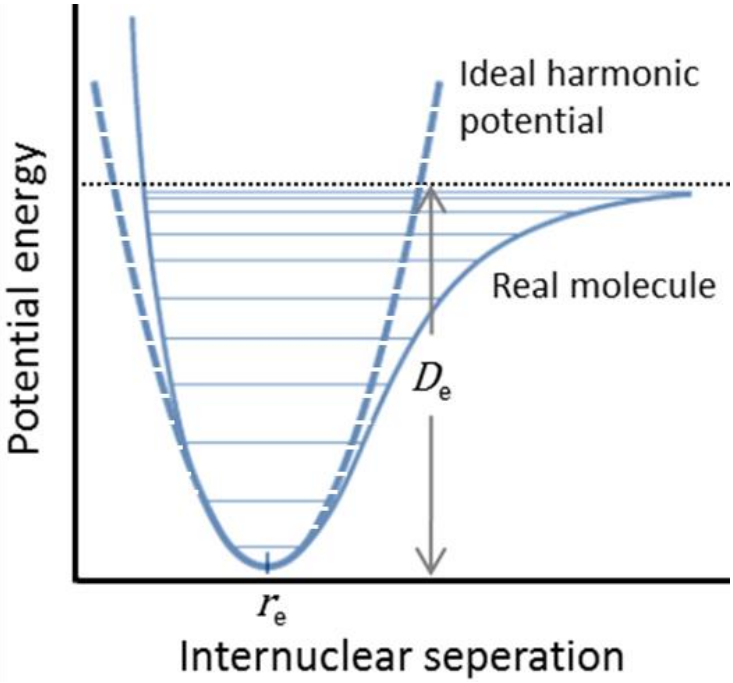

Figure 2.14 Vibrational potential energy curves of an ideal harmonic oscillator model (dashed line) and a real molecule (solid line). Adapted from ref. [122] with permission from Elsevier.

Figure 2.14 shows the potential energy curves for the ideal harmonic vibration and real molecular vibration. At low vibrational energies two curves are very similar, but at higher vibrational energies the curve for the real molecule becomes much wider. Additionally, the space of two adjacent vibrational energy levels for a real molecular vibration become smaller and smaller as the vibrational quantum number increases. In such a case, the motion becomes anharmonic. A more accurate description of vibrational modes in real molecules is given by the anharmonic approximation of the vibrational potential. The empirical description of the potential energy in a diatomic molecule is given by the Morse function [122]:

$$V(r) = D_e(1e^{-a(r-r_e)})^2$$

where D_e is the molecular dissociation energy measured to the bottom of the potential energy curve in **Figure 2.14**, and a is a constant equal to $(\frac{k}{2D_e})^{1/2}$. The energy between the vibrational modes is then no longer equidistant, and with raising vibrational quantum number it becomes smaller. The vibrational energy levels E are given by

$$E = h\nu_e[(v+\frac{1}{2}) - x_e(v+\frac{1}{2})^2]$$

where ν_e is the harmonic vibrational frequency and x_e is anharmonicity constant, $x_e = \frac{\nu_e}{4D_e}$. [122] The selection rules obtained for allowed vibrational transitions, previously mentioned in the Section 2.1.3, now can be described as $\Delta v = \pm 1, \pm 2, \pm 3, \ldots$

Molecules containing more than two atoms have more than one bond, and various vibrational modes can be coupled. For such complex molecules, all vibrational modes can be simplified as several independent motions, which are called normal modes. In addition, some of the vibration modes of large molecules can be classified when considering the symmetry of the molecule. The number of normal modes therefore depends on the total number of atoms and the molecule symmetry.

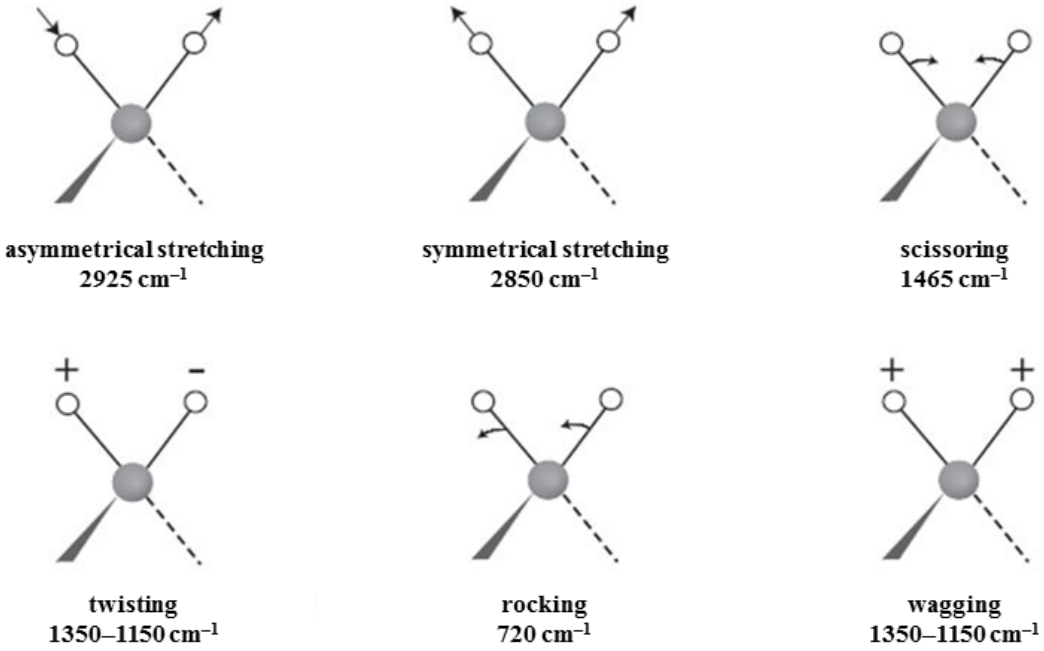

Figure 2.15 Vibrational modes of a methylene group (–CH_2–). Adapted from ref. [122] with permission from Elsevier.

As introduced in Section 2.1.3, there is a "selection rule" that decides whether molecular vibrations can be interacted with infrared photons. The normal modes of vibration that fulfill the above-mentioned selection rules are infrared-active, and be measured using infrared spectroscopy. For example, atoms in the methylene group that are ubiquitous in organic compounds have six different vibrational modes: asymmetrical and symmetrical stretching, scissoring, rocking, twisting and wagging, as shown in **Figure 2.15**. [122] All of these vibrations are capable of absorbing infrared light at characteristic frequencies.

In theory, a normal vibration involves vibrational motions of all atoms in a molecule.

However, a normal vibration is generally dominated by the contribution of a vibration localized within a particular group of atoms in a molecule. If an absorption due to such a group vibration has a high intensity, it is called a characteristic absorption band. [122] Some representative group vibrations studied in this thesis and the approximate wavenumbers of the infrared absorption bands arising from them are listed in Table A1 in the Appendix. The characteristic absorption bands provide clues for identifying compounds or their substructures by infrared spectroscopy.

2.4.2 Attenuated Total Reflection Environmental Cell

It took a long time from the discovery of IR light in 1800 to the emergence of the commercial IR spectrometers in laboratories. Although methodologies and techniques advanced rapidly during 1940s, IR spectroscopy became the most widely used vibrational spectroscopic technique after Fourier transform instruments were introduced in the 1970s. [89] Today, an infrared spectrum in the entire wavenumber range can be simultaneously recorded by using the Fourier transform method, however, it was obtained from the dispersive method by measuring at each wavenumber separately before the development of Fourier transform infrared spectroscopy (FTIR). [123]

The Fourier transform technique enables IR spectrum to be acquired in few milliseconds or even faster, which is essential for the *in-situ* measurements. Various intermolecular interactions and bond variation are widely present in different physical and chemical processes, such as the breaking and formation of hydrogen bonds, van der Waals forces and chemical bonds. These variations of chemical environment give rise to the changes in molecular vibration, which can be studied with infrared spectroscopy. Many new experimental techniques, like diffuse reflectance, reflection-absorption and attenuated total reflection infrared spectroscopy, have been developed. [75] Aqueous environment necessitates particular attention since its influence on nanomaterial properties is poorly understood while most of their applications take in such media. Therefore, in this thesis, understanding the interaction of carbon nanomaterials with aqueous environment is taken as an important part. Due to the high sensitivity and the facile operation, attenuated total reflection (ATR) infrared spectroscopy were employed in this study to investigate the molecular vibrations at the solid-liquid interface. [74]

Now ATR-FTIR measurements can be realized by mounting the commercial ATR accessory (**Figure 2.16**) in an infrared spectrometer. The core component of ATR accessory is an optically dense crystal made of IR transparent material. When the incident infrared beam is introduced onto the ATR crystal at a certain angle, a total internal reflection will occur, which is

the precondition for ATR measurements. However, the incident light is not entirely reflected back due to its wave-like properties. An evanescent wave that can penetrate a few micrometers (0.5−5 μm) into the sample is generated. The evanescent wave attenuates exponentially with increasing the penetration depth. [75, 122] Consequently, the energy of IR radiation is transferred to the sample, and the difference between the incident beam and the reflected beam shows the characteristic information of sample. When scanning over the wavenumber of the incident IR beam, the sample selectively absorbs incident light at specific wavenumbers, resulting in a decrease in reflectance. Accordingly, the attenuated reflected beam is recorded by the detector and a spectrum containing the information of the sample can be thus obtained.

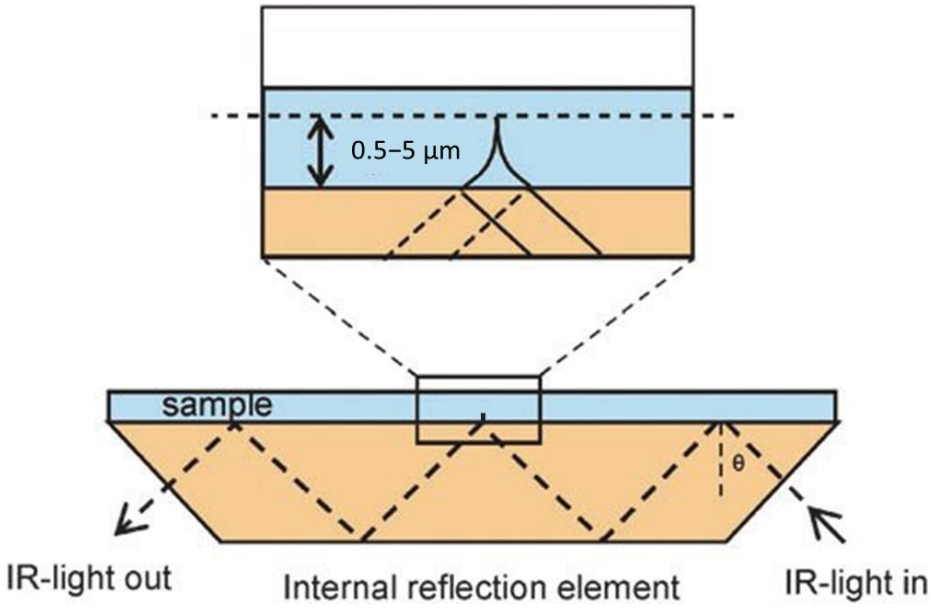

Figure 2.16 Schematic illustration of the multiple reflection in an ATR crystal. Adopted from ref. [75] with permission from the Royal Society of Chemistry.

In order to ensure multiple reflections of incident IR light in the ATR crystal, the refractive index of the ATR crystal must be greater than that of the sample. [75] Since the refractive indices of most solid and liquid materials are lower than 1.8, crystals with a refractive index between 2.4 to 4.0, such as diamond, Ge, Si, ZnSe, AgCl etc., are usually employed in the commercial ATR accessory. [123]

The FTIR spectra shown in this thesis were measured in the ATR mode using a Bruker Vertex 70v spectrometer equipped with a KBr beamsplitter and a MCT (mercury cadmium telluride) detector. Spectra were recorded in the mid-infrared region between 800 and 4000 cm^{-1} with a spectral resolution of 4 cm^{-1}. A ZnSe ATR crystal was used using a custom-made single path ATR accessory designed by Dr. Ulrich Schade in HZB. The *in-situ* surface chemistry investigations were realized using an environmental cell that is capable of introducing dry air,

humid air and liquid water to the sample surface. During the measurements the sample chamber and optical paths were maintained in vacuum. The humid air was prepared by bubbling dry air through deionized water, and the liquid water was directly injected through the inlet using a syringe. For all samples, a reference spectrum was measured on the clean ATR crystal following which the spectra were first collected for the dry sample and then subsequently for the sample exposed to humid air and liquid water. A spectral resolution of 4 cm^{-1} was set. 1024 scans for reference spectrum, 128 scans on dry CDs samples and 32 scans for *in-situ* measurements were collected.

2.5 Summary

In this chapter, a particular attention has been paid to X-ray, UV and IR spectroscopies, which are used in this dissertation for determining the electronic structure and chemical composition. The theoretical background and the development of these spectroscopic techniques are described. Each technique described here provides specific information on materials. Thus, the coupling of several techniques to investigate the same sample is of crucial importance for the better understanding of carbon nanomaterials.

XAS and XES can characterize the local structure of unoccupied and occupied states, which offers information on both the electron configuration and chemical composition. XPS is widely used for determining the chemical state of the element. For the UPS, it is always used to study the valence band structure of the sample at the molecular scale and it is sensitive to the heteroatoms doping. IR spectroscopy probes the chemical bonds in the materials. X-ray spectroscopies are core-level techniques, and characterize the sample in an element-specific manner, whereas the UPS and IR spectroscopy are molecular spectroscopy techniques. For the two samples studied in this dissertation, CDs and PCN, the carbon atoms are of most interest. The nitrogen atoms are also widely existed not only in polymeric carbon nitride, but the CDs with amino groups functionalized and core nitrogen doping. Additionally, oxygen are also appears in the surface functional groups of modified CDs and PCN. Therefore, the local structure at carbon, nitrogen and oxygen K-edges have been identified by XAS and XES. And their core levels are also probed using XPS. The samples of interest are characterized using UPS and IR if necessary. Thus this combination of various techniques is favorable to reveal the relationship of the performance of carbon nanomaterials and their electronic and chemical structures.

Apart from the *ex-situ* characterizations, particularly important also is the *in-situ* analysis of the carbon nanomaterials in aqueous environment. Environmental cell equipped with ATR-

FTIR allows the measurement of the hydrogen bonding network around the sample surface. XAS applied to liquid using flow-cell strategy offers the opportunity to study the charge transfer between CDs and water. In the following chapters, examples on the investigation of CDs and PCN materials will be illustrated using these spectroscopic techniques.

Chapter 3

Luminescent Surface Modified Carbon Dots

Content

Large part of this chapter is taken from the published work Ren et al. [137], edits have been made to match the flow of the dissertation. Scientists from different institutes were involved in the published paper. Ren and Petit designed the experiments. Ren performed all experiments, analyzed the data, and wrote the initial draft of the manuscript. Weber and Bande conducted the theoretical simulations. Weigert and Resch-Genger helped with the PL measurement. Wang and Lauermann helped with the XPS measurement and data analysis. Choudhury and Petit helped with the XAS and XES experiments in BESSY II. Petit supervised the project.

3 Luminescent Surface Modified Carbon Dots

The unique physicochemical properties of carbon dots (CDs) can be effectively adjusted through modifying their chemical composition. However, a major challenge remains in understanding the core and surface contributions to optical and electronic transitions. In this chapter, three blue luminescent carbon dots with carboxyl, amino and hydroxyl groups were characterized by UV−vis absorption and emission spectroscopies, synchrotron-based X-ray spectroscopies, and infrared spectroscopy. The influence of the surface functionality on their fluorescence was probed by pH-dependent photoluminescence measurement. Moreover, the hydrogen bonding interactions between water and the carbon dots' surface groups were characterized by infrared spectroscopy. This comprehensive spectroscopic study demonstrates that the surface chemistry has a profound influence on the electronic configuration and surface-water interaction of carbon dots, and thus affecting their photoluminescence properties.

3.1 Motivation

As discussed in Chapter 1, the surface functionalization of CDs is of vital importance for many applications. Depending on the surface moieties, the surface-related electronic acceptor levels, [124–126] as well as hydrogen bond interaction with solvent molecules can be modulated, [127–129] affecting the photoluminescence (PL) properties of CDs. Extensive studies of surface-related optical transitions based on UV−vis absorption and emission spectroscopies have been conducted to elucidate fluorescence mechanisms. PL with pH dependence can be monitored to assess the effect of surface groups on optical properties, which is a widely reported phenomenon for CDs. [130–132] On the other hand, no direct measurement of electronic transitions on surface-modified CDs has been conducted so far to our knowledge. No spectroscopic evidence of hydrogen bonding between CDs and solvent molecules beyond indirect PL measurements are either available.

Extending the characterization of CDs with complementary spectroscopy techniques is strongly needed for a deeper understanding of the structure–performance relationship of CDs. As introduced in previous chapters, synchrotron-based soft X-ray spectroscopies are powerful tools for exploring element-specific electronic states and chemical structures of carbon nanomaterials. XAS and XES can respectively provide information about the partial unoccupied and occupied electronic states. [133] In combination with XPS, which has been frequently used to probe the core levels of carbon, oxygen and nitrogen in CDs, [131,134,135] these methods can present a complete picture of electronic states in CDs. No reports of XAS/XES on carbon dots are though available at the moment to our knowledge. In addition, FTIR using an attenuated total reflectance (ATR) environmental cell enable the direct detection

of the hydrogen bonding environment around carbon nanomaterials. [136] Only surface groups are expected to interact with water molecules therefore exposure to humid air could also be used to identify surface-related chemical groups and the hydrogen bonds acceptor/donor nature.

In this chapter, three commercial blue luminescent CDs functionalized with carboxyl (CDs-COOH), amino (CDs-NH_2) and hydroxyl (CDs-OH) groups are studied. The three types of carbon dots were purchased from ACS Materials (USA), and used without further purification or treatment except when mentioned specifically. The technical data of three samples are listed in **Table 3.1**. After the preliminary characterizations on these CDs samples, the electronic structures of three CDs were investigated by XAS and XES on solid samples at the U49-2_PGM-1 beamline of the BESSY II synchrotron radiation source using the LiXEdrom end station. The interpretation of XA spectra is discussed based on density functional theory calculations. Moreover, XPS was applied to align the XA and XE spectra at C, N and O K-edges to the Fermi level to estimate the contribution of each atom to the valence and conduction bands. In addition, the hydrogen bonding interaction of the CDs with water molecules were characterized by ATR-FTIR spectroscopy. Finally, we attempt to correlate these results with the PL properties of differently functionalized CDs which were measured at Bundesanstalt für Materialforschung und -prüfung (BAM), Berlin, Germany in collaboration with Resch-Genger and Weigert.

Table 3.1 Technical data of three carbon dots. Reproduced from ref. [137] with permission from the Royal Society of Chemistry.

Sample	Product	Synthesis	Concentration [mg/mL]	Size [nm]
CD s-COOH	GNQD0301 Carboxylated GQDs	Precursor pyrolysis	5	＜ 10
CDs-NH_2	GNQD0201 Aminated GQDs	Hydrothermal method	5	＜ 5
CDs-OH	GNQD0101 Blue Luminescent GQDs	Polymerization of organic small molecule	5	＜ 15

3.2 Optical Properties and Chemical Compositions of Carbon Dots

The optical properties are the most straightforward way to recognize these carbon dots samples by measuring UV−vis absorption and PL spectroscopy. The broad absorption spectra and the much more structured emission spectra of the three CDs are shown in **Figure 3.1**. The closely

resembling absorption spectra of the three CDs samples reveal a well-resolved peak at around 340 nm, which originates from the C=O bonds of the carbonyl and/or carboxyl groups in carbogenic core or from COOH groups. The higher energy absorption features in the region 220−250 nm (**Figure 3.1**a) is associated with the optical transition in the carbon core. [42] The PL spectra in **Figure 3.1**b obtained upon UV excitation exhibit three distinct emission peaks at around 385 (I), 420−433 (II), and 463 nm (III). According to previous studies, these emissions I, II and III can be attributed to n–σ* (such as C–O–C, C–OH or C–N), n–π* (in C=O), and π–π* transitions in the graphitic core, respectively. [125,132] A more profound assignment of the origin of CDs' optical properties is hampered by the different synthetic routes used to prepare the commercial CDs, which also complicates the evaluation of the exact role played by the different surface groups. These challenges are addressed in the following by the detailed characterization of the samples using different analytical techniques, particularly X-ray spectroscopies.

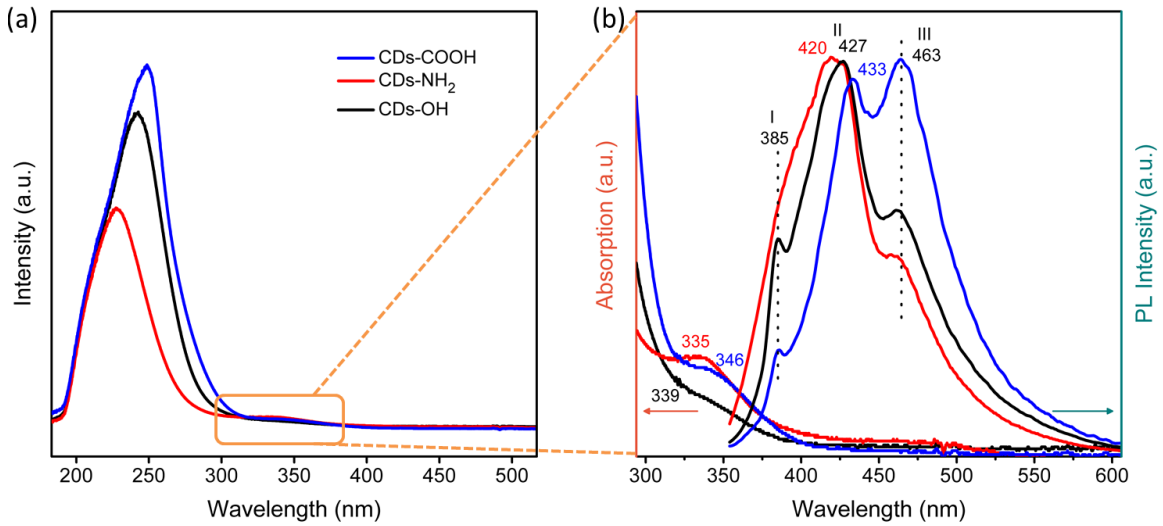

Figure 3.1 UV-Vis absorption and emission spectra of blue luminescence carbon dots. Excitation was at 338 nm. Reproduced from ref. [137] with permission from the Royal Society of Chemistry.

The chemical composition of the three CDs can be characterized by ATR-FTIR spectroscopy. As shown in **Figure 3.2**, ATR-FTIR spectra of the CDs with different surface termination, characterized under dry air flow, have different vibrational signatures, coming presumably from both surface groups and carbogenic core. Peaks at 1122 cm^{-1} and 1174 cm^{-1} in CDs-COOH sample and at 1260 cm^{-1} in CDs-OH are recognized as C–O stretching vibrations in different bonding environment. [135] The peak at 1226 cm^{-1} in CDs-NH_2 is most likely related to C–N stretching. [138] The features around 1390 cm^{-1} are attributed to the bending modes of O–H and/or C–H in CDs-COOH and CDs-OH. [139] The feature at 1400–1450 cm^{-1} in CDs-NH_2 is assigned to CH_2 bending. [45,140]

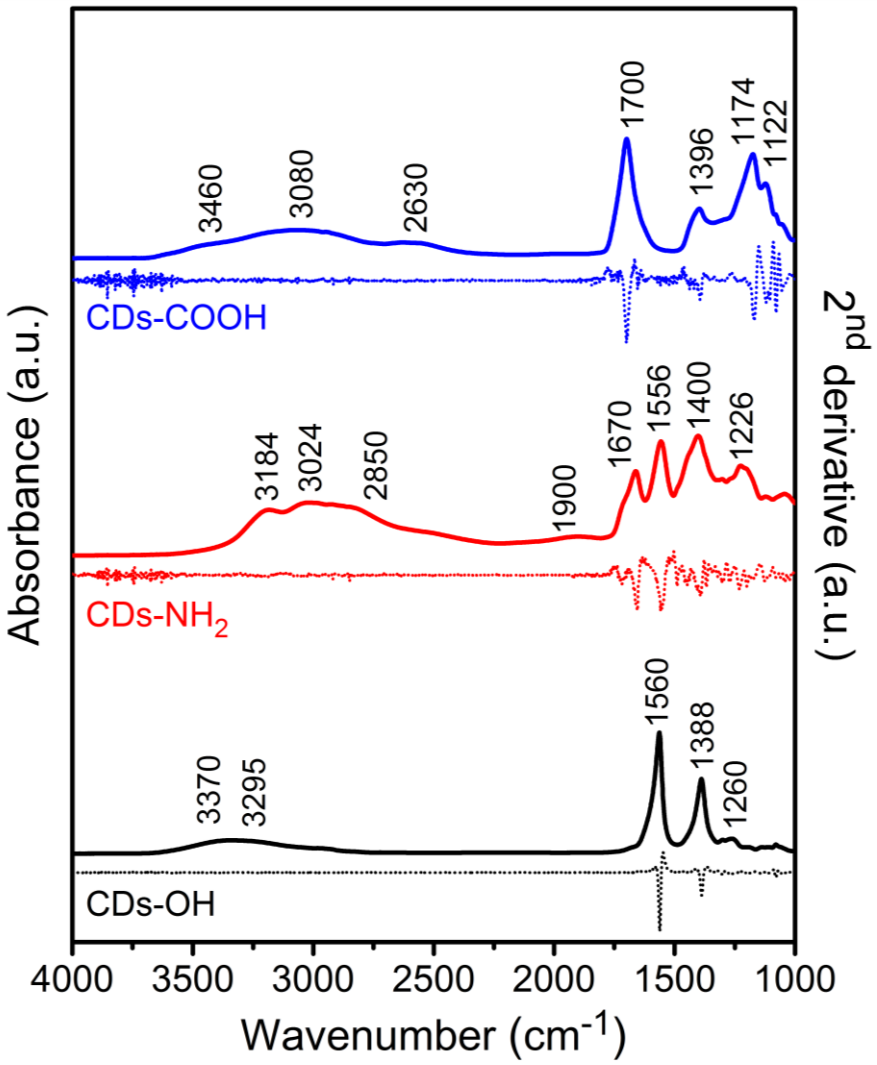

Figure 3.2 ATR-FTIR spectra of CDs with different surface chemistries measured under dry air flow. The second derivative of FTIR spectra are shown in short dots. Note that the contribution from strongly adsorbed water molecules at 1650 cm^{-1} is observed on CDs-COOH. Reproduced from ref. [137] with permission from the Royal Society of Chemistry.

All CDs contain a significant amount of C=O bonds based on X-ray spectroscopy results; however FTIR shows that they are in different chemical environment. A strong band for C=O vibrations is observed at 1556 and 1560 cm^{-1} in CDs-NH_2 and CDs-OH, respectively, associated to carbonyl groups in their carbogenic core. [141] In this region, the IR spectrum of CDs-NH_2 has two clear features at 1556 and 1670 cm^{-1}, where the former arise primarily from the C=O stretching vibration in the carbon core and the latter is attributed to the bending vibration mode of NH_2 group. [140] A sharp feature at 1700 cm^{-1} for CDs-COOH was associated with C=O stretching vibrations from surface carboxyl groups. [45] For CDs-NH_2, the overtone bands of amino group at 1900 cm^{-1} can be detected.

Broad bands observed in the region of 2800–3000 cm^{-1} for all CDs samples, are most likely associated with C–H stretching vibrations. In the higher frequency region around 3000–

3600 cm^{-1}, stretching modes of hydroxyl or amino groups and residual adsorbed water are expected. It should be noted that, unlike the band observed in hydroxyl group of CDs-OH, the O–H stretch in carboxyl groups of CDs-COOH appears as a very broad absorbance in the region 2400–3200 cm^{-1}, which is attributed to the formation of intramolecular hydrogen bonds among carboxylic groups. [139] The band at 3460 cm^{-1} could result from O–H stretching of strongly adsorbed water on CDs-COOH. In addition, the low C=O stretching frequency (1700 cm^{-1}) of COOH groups also corroborates the strong water adsorption on CDs-COOH since C=O stretching frequency is known to decrease by hydrogen bonding with carboxyl groups. [142] The asymmetrical broadening of the C=O band peak toward lower frequency is due to O–H bending mode to these strongly adsorbed water molecules, which is observed at 1650 cm^{-1} on the second derivative of the IR spectrum (**Figure 3.2**). These results clearly indicate that water could be adsorbed on the CDs-COOH surface even under dry air flow at room temperature.

3.3 Electronic Structure of Carbon Dots

X-ray spectroscopies are employed to determine the local electronic configuration and chemical structure of different blue luminescent CDs. Note that X-ray spectroscopies are sensitive to both core and surface contributions of the CDs due to their small size. The XA spectra of the three CDs samples at C K-edge are compared in **Figure 3.3**. Four main features at 285.2 (A), 287.5 (B), 288.9 (C) and 294-297 (D) eV are observed. In addition, DFT calculations using an individual-atom decomposition method were performed by Mr. F. Weber in HZB, [143] to enable the assignment of the different features of the C K-edge XA spectra (see **Table 3.2**).

According to the calculation and previous experimental studies on carbon nanomaterials, feature A at 285.2 eV can be assigned univocally to the excitation of core electrons into $\pi^*_{C=C}$ orbitals. [144] Depending on the chemical environment of the core orbitals, i.e., the functionalization of the carbon atom, one finds shifts with respect to the exact position of the expected signal. The feature B is typical of the transition to $\pi*$ orbital of C–O–C in an epoxide structure [144,145] but contribution from $\pi*$ of C–COH bonds in hydroxyl group is also possible. [146,147] The sharp peak at 288.9 eV (C) is mainly attributed to both $\pi^*_{C=O}$ excitations in carboxyl and/or carbonyl groups and σ^*_{O-H} transitions in OH group. [147,148] Signal C1 at 288.4 eV can be attributed to additional $\pi^*_{C=C}$ transitions in sp^2 bridge and edge positioned carbon atoms [149] as well as $\pi^*_{C=O}$ transitions. [144] At 290.6 eV, one can find the feature C2 in the CDs-COOH sample, which is best assigned to σ^*_{C-O} transitions in carboxylated carbon atoms, based on the theoretical calculations. In different

publications [145,146,149] this signal is described as $\pi^*_{O-C=O}$ transition, which can be supported by the calculations. It shall be mentioned that both features C and C2 lie also in the typical range for various σ^*_{C-H} transitions, which leads to the increase in the background intensity. Finally, feature D in the range of 294-297 eV is related to all kinds of σ^*_{C-C} and σ^*_{C-O} transition.

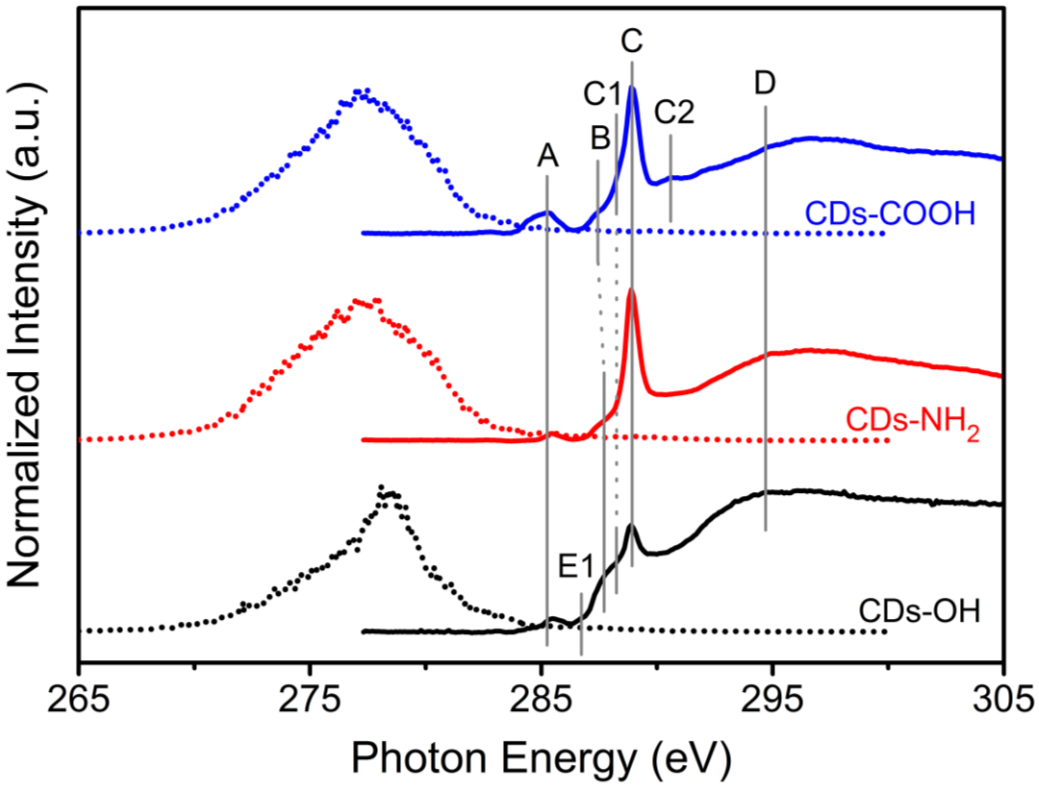

Figure 3.3 XA/XE spectra at the C K-edge of carbon dots with different surface chemistries. Reproduced from ref. [137] with permission from the Royal Society of Chemistry.

XES is complementary to XAS as the observed spectral shape reflects the partial density of occupied states. **Figure 3.3** presents the non-resonant C Kα XE spectra of CDs samples. The general profiles in the C Kα XE spectra are similar for the CDs-COOH and CDs-NH_2. All spectra exhibit a broad feature, which is associated with the σ state and centered at approximately 277.2 eV, as well as a high-energy shoulder, which is associated with the π state and centered close to 280.8 eV. For CDs-OH, the σ and π features locate respectively around 278.4 eV and 280.3 eV. [144,147]

The O K-edge XA/XE spectra of the three CDs samples (**Figure 3.4**) and N K-edge XA/XE spectra of CDs-NH_2 (**Figure 3.5**) provide supplementary information regarding the chemical bonding of oxygen and nitrogen atoms. In the O K-edge XA spectra, the sharp peaks at 533.8 eV (CDs-NH_2 and CDs-OH) or 534 eV (CDs-COOH), together with the feature shown at the left shoulder (532.9 eV), are π* resonances from C=O bonds. [150,151] Besides, a shoulder at 535.1 eV for the O 1s → π^*_{C-OH} of the carboxyl groups is clearly observed for CDs-

COOH. The feature at 537 eV can be ascribed to transitions from O 1s core levels to π* states in epoxy configurations. The σ* feature, which appears at the higher energy region (539–550 eV) consists of C–O, O–H, C=O and epoxide groups. [152,153] The distinguishable feature at 545.3 eV for 1s → $\sigma^*_{C=O}$ in carboxyl groups is only shown in CDs-COOH (**Figure 3.4**). [150] In the N K-edge XA spectrum of CDs-NH_2, the contribution of nitrogen to the electronic configuration and local structure in CDs-NH_2 is evidenced by two sharp features at 399.7 eV and 402.2 eV, which arise from transitions of N 1s to unoccupied π* states of pyridinic (or pyrrodic) nitrogen and quaternary nitrogen. The broad feature above 406 eV is attributed to the transitions to σ* states of different nitrogen bonds. [153,154]

Table 3.2 Interpretation of C K edge XA spectra of carbon dots based on local time-dependent DFT calculations. Reproduced from ref. [137,143] with permission from the Royal Society of Chemistry.

Feature	Energy (exp.) (eV)	Energy (theo.) (eV)	Group*	Assignment
A	285.2	285.5	C=C (all sp^2)	π*(C=C)
		285.3	**C**–COOH (edge)	π*(C=C)
		284.7 / 286.3	Epoxy (basal sp^2/ edge sp^2)	π*(C–C)
B	287.5	287.6 / 287.1 / 287.7	Epoxy (basal / bridge / edge)	π*(C–O–C)
		286.9 / 286.8 / 288.6	C–OH (basal / bridge / edge)	π*(C–COH)
C1	288.4	288.6	C=C (bridge), C–OH (edge)	π*(C=C)
		288.6	COOH	π*(C=O)
C	288.9	288.5	**C**–C=O (basal / edge)	π*(C=O) and π*(C–C)
		289.2 / 289.1 / 290.1	C–OH (basal / bridge / edge)	π*(C–COH) and σ*(O–H)
		289.7	**C**–COOH (edge)	π*(C=O) and π*(C=C)
		289.1 / 289.4 / 289.1	C–H (basal / edge)	σ*(C–H)
C2	290.6	290.7	COOH	σ*(O–H)
		289.7 / 291.3	**C**–COOH (edge)	π*(C=O) / σ*(C–O)
		291.2	Epoxy(edge)	σ*(C–C)
		291.5 / 291.2 / 291.1	C–OH (basal / bridge / edge)	σ*(C–O) / σ*(O–H) and σ*(C–C)
D	294-297	295.0 / 294.7	C–H (basal sp^3/ edge sp^3)	σ*(C–C)
		294.5 / 295.9	C–C (edge / bridge)	σ*(C–C)
		295.6 / 295.8 / 294.7	Epoxy (basal / bridge / edge)	σ*(C–C)
		293.0 / 294.0–296.0	C–OH (bridge / edge)	σ*(C–O) and σ*(C–C)
		292.8 / 293.5	**C**–COOH (edge)	σ*(C–C) / σ*(O–H)
		296.4	COOH	σ*(C–O)

*Group refers to the type of carbon atom that is excited in a localized, single-electron excitation calculation. When there are more than one carbon atoms in a group label, the one highlighted with bold font was excited

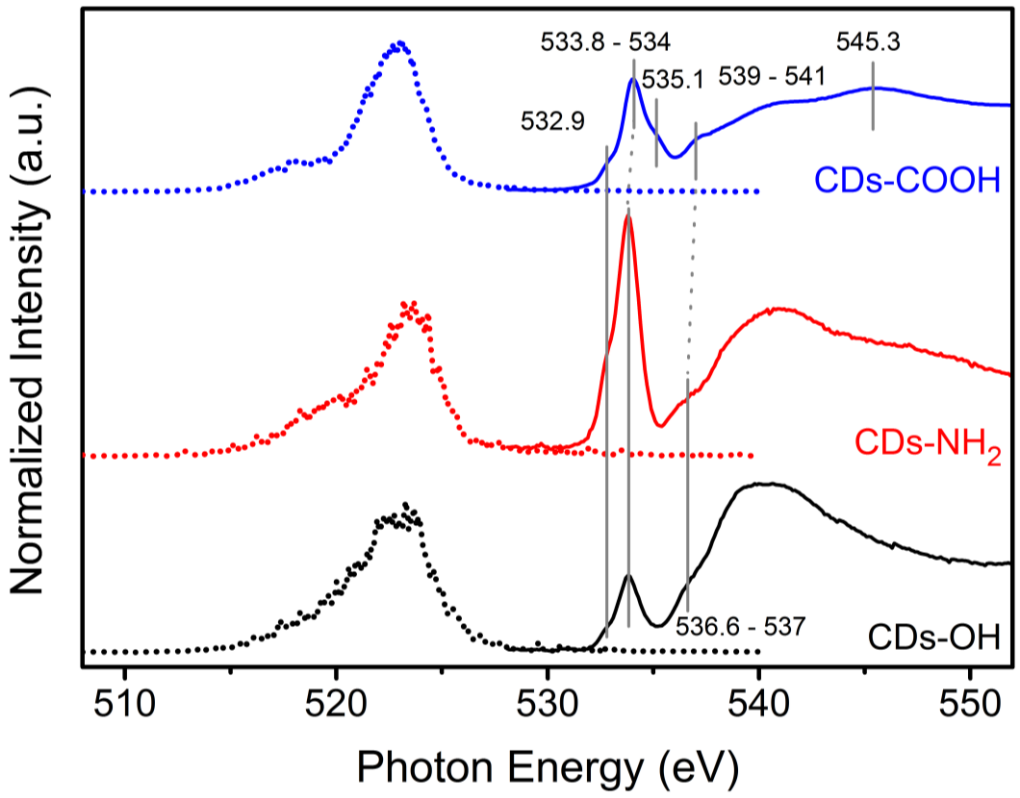

Figure 3.4 XA/XE spectra at the O K-edge of carbon dots with different surface chemistries. Reproduced from ref. [137] with permission from the Royal Society of Chemistry.

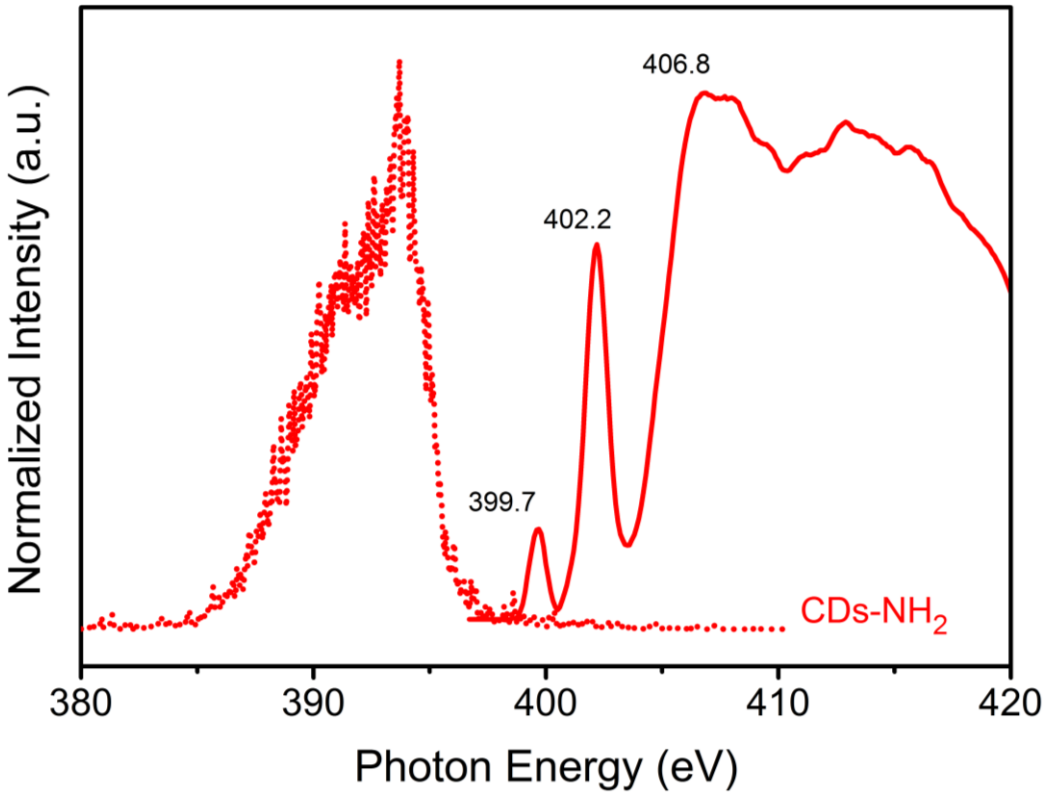

Figure 3.5 XA/XE spectra at the N K-edge of CDs-NH_2. Reproduced from ref. [137] with permission from the Royal Society of Chemistry.

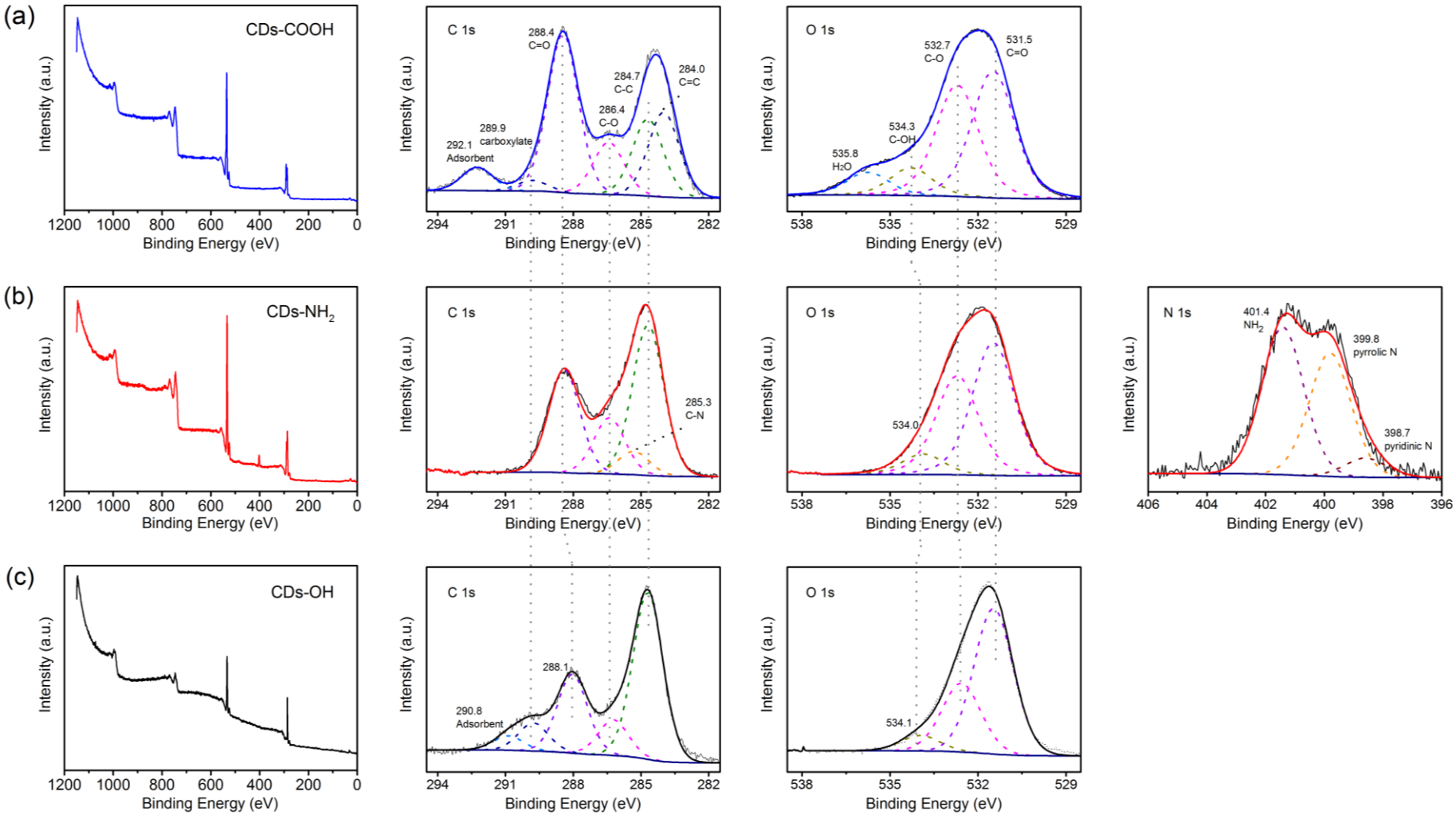

Figure 3.6 XPS results of the three carbon dots samples: (a) CDs-COOH, (b) CDs-NH_2 and (c) CDs-OH. Reproduced from [137] with permission from the Royal Society of Chemistry.

Figure 3.6 shows the XPS results measured for three CDs samples. In C 1s XPS, three peaks at 284.7, 286.4, and 288.4 eV can be assigned to C–C, C–O and C=O respectively. [155] C=C component can be remarkably distinguished at 284 eV in CDs-COOH sample, suggesting that CDs-COOH consist of large π-conjugated domains in the carbogenic cores. [156] There is a pronounced feature for the adsorbed residual water at 535.8 eV in the O 1s spectra, which was also observed on FTIR (**Figure 3.2**). The peak at 289.9 eV shown in CDs-OH corresponds to carboxylate-like structure [157] formed with the C=O in the core. The presence of C–N bonds was also confirmed in the C 1 s spectra of CDs-NH_2 with the peak at 285.3 eV. O 1s spectra can be deconvoluted into three peaks of C–O at 531.5 eV, C=O at 532.7 eV, and C–OH around 534.2 eV. [155] There is one more constituent peak at higher binding energy (535.8 eV) in CDs-COOH sample, which can be attributed to adsorbed H_2O molecules. [158,159] The N 1s XPS spectrum of CDs-NH_2 contains three peaks at 398.6, 399.8, and 401.4 eV, for pyridinic C–N–C, pyrrolic C_2–N–H, and NH_2, respectively. [160]

Table 3.3 Atomic percentage of each element in three samples, calculated from XPS. Reproduced from ref. [137] with permission from the Royal Society of Chemistry.

Sample	Element	Atomic percentage (%)
CDs-COOH	carbon	49.3
	oxygen	50.7
CDs-NH_2	carbon	50.9
	oxygen	41.5
	nitrogen	7.6
CDs-OH	carbon	58.7
	oxygen	41.3

XPS measurements of the C 1s, N 1s and O 1s core levels of the three differently functionalized CDs (**Figure 3.6**) confirm the differences in the chemical and electronic states. The atomic percentage of each element was estimated by comparing the relative area of each core levels (**Table 3.3**) and all three CDs materials have a high oxygen content, which is most likely widely distributed between the carbogenic core (carbonyl and epoxide groups) and surface (hydroxyl and carboxyl groups). [33,161] Using XPS results, C, N and O XA/XE spectra could be aligned to a common energy axis by offsetting XA/XE spectra using their corresponding XPS core-hole binding energies referenced to the Fermi level (**Figure 3.7**). [162–164] The Fermi level is estimated for each edge by measuring the lowest binding energy peak of the respective core levels (**Figure 3.6**). In the vicinity of the band gap, electronic states contributing to valence and conduction bands can be identified. For all CDs, the C K-edge XES onset occurs at higher energy than that of O K-edge, which means that the

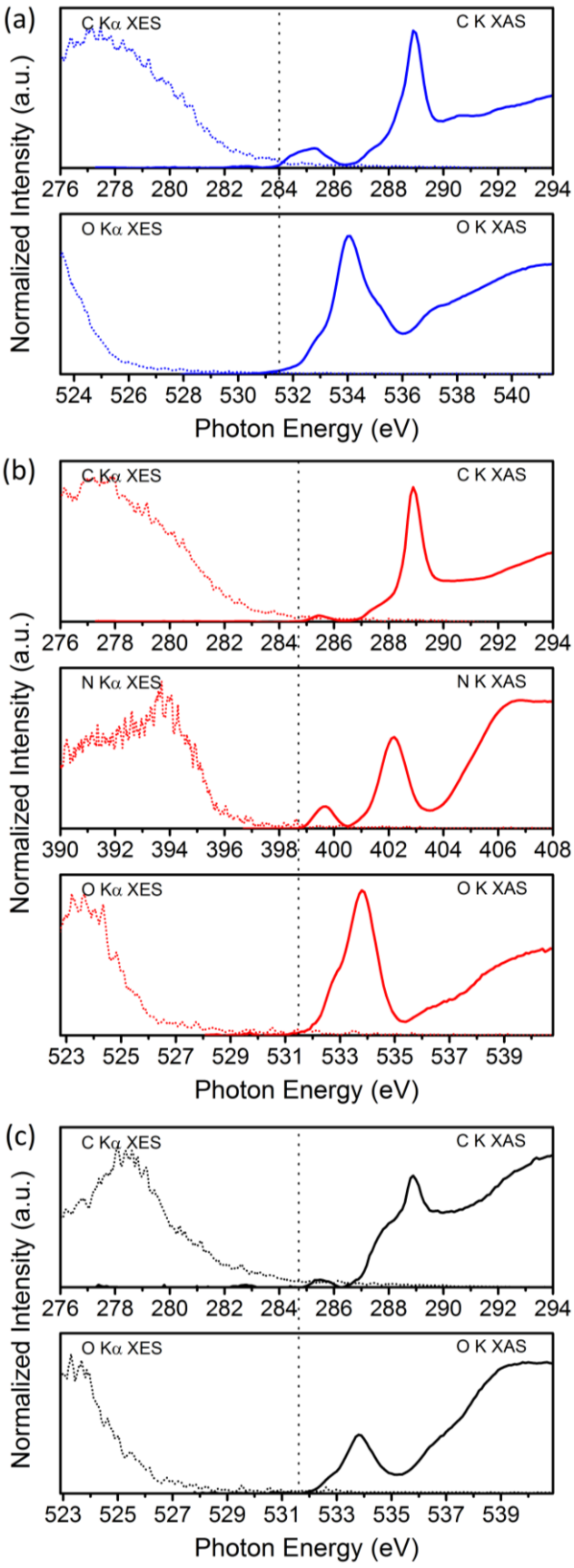

Figure 3.7 C, N and O K-edges XA/XE spectra in the vicinity of the band gap of (a) CDs-COOH, (b) CDs-NH_2, and (c) CDs-OH. The dotted line shows the estimated Fermi level based on XPS measurements. Reproduced from ref. [137] with permission from the Royal Society of Chemistry.

carbon atoms contribute more to the density of states (DOS) in the valence band. For CDs-NH_2, the N K-edge XES onset is sharper with more spectral weight 4 eV below the Fermi level, therefore N atoms may also contribute significantly to occupied states. Previous studies have already confirmed that introducing nitrogen atoms, as an electron-donating element, into CDs, [165] graphene [166] and other carbon nanomaterials [147] could modulate the valence band edge or create midgap states, leading to a narrower band gap.

The π* transition from sp^2 carbon at the C K-edge XAS is located at lower energy than first unoccupied states of the O K-edge XAS, indicating that carbon atoms in the graphitic core dominate the DOS in conduction bands, in particular for CDs-COOH, for which the π* feature is more visible. The unoccupied states from nitrogen atoms are located closer to the edge than those from carbon and oxygen atoms in CDs-NH_2. For CDs-OH, both carbon and oxygen atoms may contribute to the conduction band minimum since the first unoccupied states have similar relative energy with respect to the Fermi level.

3.4 Hydrogen Bonding Network and Its Influence on Fluorescence

In order to estimate the ability of surface groups to form hydrogen bonds with water molecules, the CDs were characterized by *in-situ* infrared spectroscopy by recording FTIR spectra during exposure to humid air. **Figure 3.8**a-c present the ATR-FTIR spectra of CDs-COOH, CDs-NH_2 and CDs-OH plotted with respected to increasing the relative humidity (RH). To compensate the overall signal decrease, the IR spectra recorded under dry air (RH = 0%) and humid air (RH = 80%) on each sample are normalized using the peak around 1390 cm^{-1} as a reference (**Figure 3.8**d-f). The lower panel shows the difference spectra between these extreme RH values to illustrate the modifications induced by water exposure only. Note that the comparison between the samples based on difference spectra should be treated with caution since their respective references had different amount of initial adsorbed water.

Upon water vapor exposure, increase on O–H bending (1620-1650 cm^{-1}) and stretching (3000−3600 cm^{-1}) modes of water molecules are clearly observed. The O–H bending modes maximum on difference spectra is at 1624, 1630 and 1650 cm^{-1}, for CDs-COOH, CDs-NH_2 and CDs-OH, respectively. The O–H bending band of water molecules is known to shift toward higher frequency in the case of stronger hydrogen bonding. [167] Associated with the increase in O–H bending are the generations of water overtone feature in the region 2000−2200 cm^{-1} for CDs-COOH and CDs-OH. For CDs-NH_2, this water overtone band is located nearly to that of amino group (around 1900 cm^{-1}), and thus leads to a band broadening.

The O–H stretching region is also sensitive to the hydrogen bonding environment of

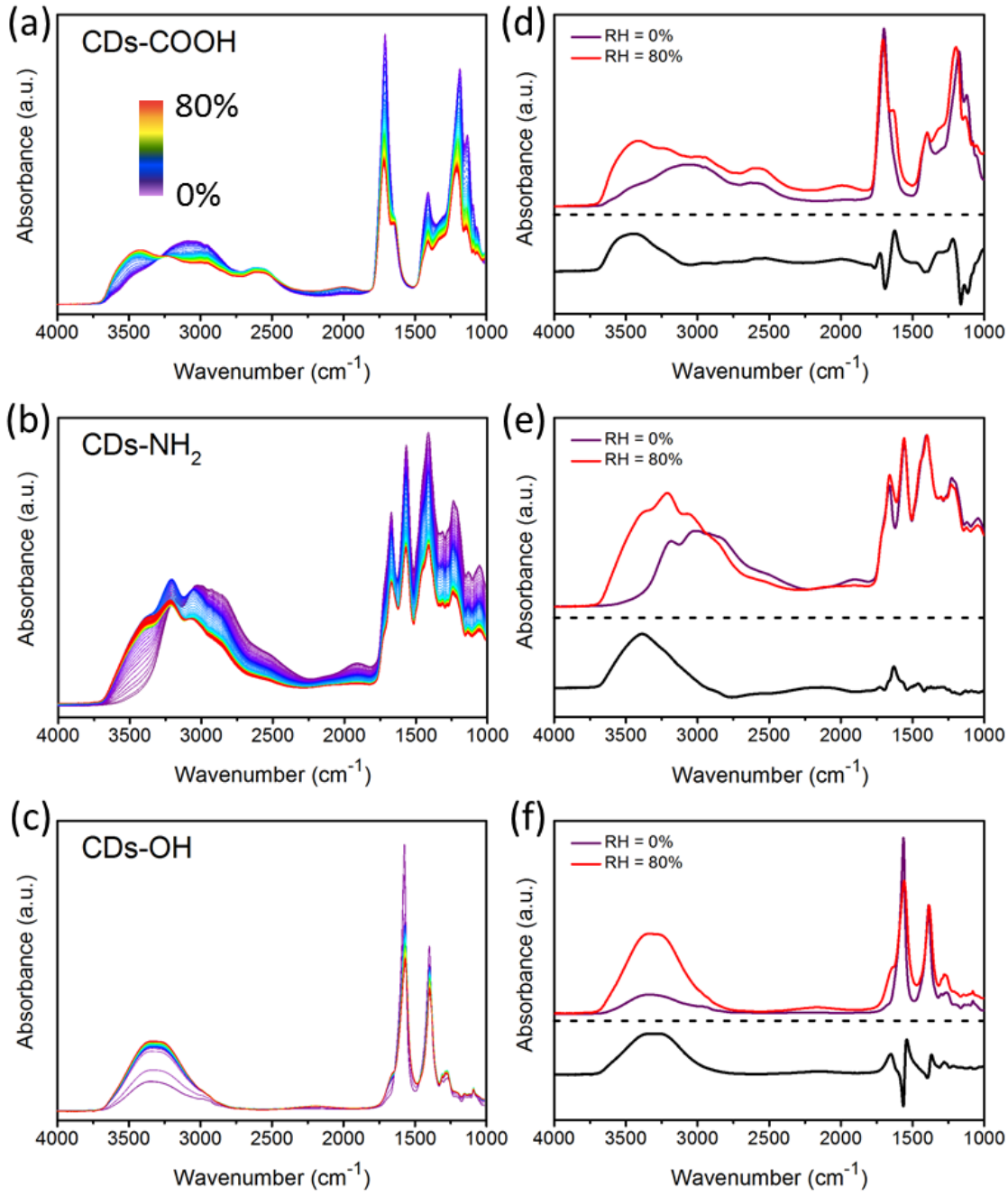

Figure 3.8 (a)-(c) FTIR spectra of carbon dots samples recorded at different relative humidity; (d)-(f) Normalized FTIR spectrum obtained from dry state and that from humid atmosphere, the lower panel shows the difference spectrum. Reproduced from ref. [137] with permission from the Royal Society of Chemistry.

adsorbed water molecules. [136,168] It consists of three components peaking at 3250, 3420 and 3540 cm^{-1}. The lowest component at 3250 cm^{-1} is assigned to the water molecules having a similar hydrogen bonding environment with ice. The component at the highest frequency (3540 cm^{-1}) is conversely ascribed to hydrogen bonding environment in poorly connected water molecules such as in small water clusters. In between the two extreme frequencies lies a third component (3420 cm^{-1}) which is associated with the hydrogen bonds stronger than that

of water clusters but weaker than network water. [169–171] For CDs-COOH and CDs-NH_2, the weakly-bonded components (3420 and 3540 cm^{-1}) are enhanced significantly after humid air exposure. For CDs-OH, the middle feature shows a red-shift of −36 cm^{-1} down to 3380 cm^{-1}, together with a strong increase of the component at 3250 cm^{-1}, indicating the appearance of strongly hydrogen bonded water molecules as compared to CDs-COOH and CDs-NH_2. However, it should be noted that for CDs-COOH sample, the different spectra most probably related to intermolecular bonding between H_2O molecules since the reference spectrum already contained a strong contribution from adsorbed water molecules.

In addition to the increase of water OH vibrational modes, surface-related modes are influenced by hydrogen bonds formation with water. After exposure to water, the C=O peak maximum of the CDs-COOH and CDs-OH is found to shift of +8 and −6 cm^{-1}, respectively, while the band for CDs-NH_2 is not shifting. In particular, C=O bonds are known to shift to lower frequency when accepting hydrogen bonds, [142] which could be used to explain the red-shift of C=O stretching in CDs-OH. While they are related to carbonyl groups in CDs-OH, most C=O bonds in CDs-COOH are part of carboxyl groups connecting with OH groups, which supply more sites for hydrogen bonds formation upon water vapor exposure. While the hydroxyl oxygen and hydrogen can each forms one hydrogen bond, it may change the angle and/or the length of the hydrogen bonds with C=O bond. These deformed hydrogen bonds induce a higher frequency for the C=O stretching than those of corresponding hydrogen bonds interaction with few water molecules (RH = 0%). [142,172] In addition, the C–O stretching band (1174 cm^{-1}) of carboxyl group in CDs-COOH is also enhanced with the exposure to water vapor due to hydrogen bonding, and shows a blue-shift of 22 cm^{-1}. [173]

Based on the previous discussion, CDs-COOH forms the strongest hydrogen bonds with water molecules, which cannot be fully removed from the CDs surface even under dry air flow or vacuum at room temperature. After exposure to humid air, a stronger hydrogen bonding network is observed on CDs-OH, therefore the following ordering, from the strongest to weakest hydrogen bonds with water, is proposed:

$$\text{CDs-COOH} > \text{CDs-OH} > \text{CDs-NH}_2$$

In order to further clarify the correlation between the PL behavior and the surface groups of blue luminescent CDs, the influence of pH on the fluorescence spectra of three CDs was also investigated (**Figure 3.9**). This reveals distinct differences among the three CDs samples. While the PL of CDs-COOH is quenched at increasing pH value, the PL of CDs-OH and CDs-NH_2 diminishes both in acidic and alkaline conditions. This pH effect correlates well with the protonation and deprotonation of the different functional groups. The carboxyl groups of CDs-COOH are deprotonated at pH 14, leading to a reduction in fluorescence. The

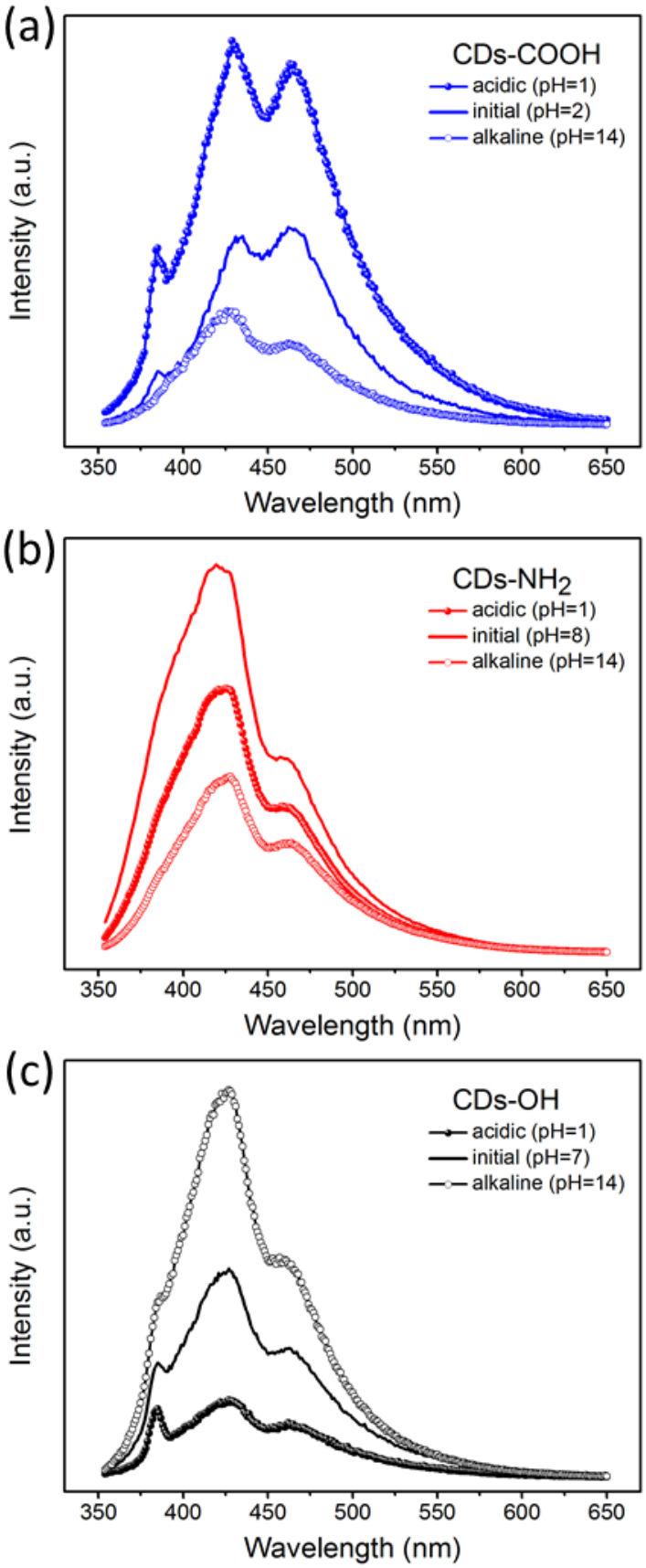

Figure 3.9 pH-dependent PL spectra of carbon dots at acidic (pH = 1) and alkaline (pH = 14) conditions; excitation was at 338 nm. Reproduced from ref. [137] with permission from the Royal Society of Chemistry.

PL intensity of CDs-NH_2 is stronger in the initial pH 8. Under both acidic and alkaline conditions, the PL is quenched uniformly throughout the whole emission range reflecting the amphoteric nature of amino groups. Since the electrostatic attraction between negatively charged hydroxyl groups and positive charged protons under acidic conditions leads to the formation of non-radiative complexes, the peak II (427 nm) in CDs-OH was significantly reduced under acidic conditions in contrast to the alkaline condition. It can be concluded that charged surface groups, either positively or negatively, tend to quench the luminescence compared to neutral groups. Note that the emission peak II at 420 nm also slightly shifts with varying the pH, which could be related to different hydrogen bonds strength with C=O groups.

Comparing X-ray and *in-situ* IR spectroscopic results with the fluorescence emission spectra helps to interpret the differences in PL behaviors among the three CDs samples. All CDs have three clear emission peaks shown in **Figure 3.1**b. CDs-COOH has the largest percentage of conjugated system, identified from XAS. Consequently, the major emission component in CDs-COOH is the peak III at 463 nm, assigned to the contribution from the conjugated carbon core. The n−π* emission peak (II) centered at lower wavelength (433 nm) is also strong on CDs-COOH sample, which is mainly associated to carboxyl groups. These results confirm that the blue fluorescence of the CDs-COOH mainly originates from the graphitic core and the C=O bonds, which is in good agreement with previous reports. [134,138,174] The surface-related emission (II) plays the predominant role in CDs-NH_2 (420 nm) and CDs-OH (427 nm) but appears shifted compared to CDs-COOH because C=O groups have a different bonding configuration. Note that the amino groups and hydroxyl groups grafted onto the carbogenic core can also enhance the integrity of the conjugated system as the electron donators, and thus induce a clear emission at 463 nm in CDs-NH_2 and CDs-OH as well. [125,175] The feature I at around 385 nm originates from an n−σ* transition. This peak is more intense in CDs-NH_2 and CDs-OH which agrees with the XPS and XAS results. In O K-edge XAS σ* intensity of CDs-OH is much stronger than other two samples; C−O also dominates O 1s XPS in CDs-OH. Similar results are shown in CDs-NH_2.

The spectral shift of the PL emission II in three CDs may be related to the C=O in different hydrogen bonding environments modified with the neighboring surface groups. [135,170] Sciortino et al showed that excited states are sensitive to solvent environment, leading to an emission shift. [176] Different local hydrogen bonding networks formed by surrounding water molecules with the surface groups may also influence the fluorescence behavior. The stronger hydrogen bond formed between CDs samples and water, the narrower emission energy level is generated, resulting in larger red shifts. Thus, the spectral shifts of the peak II, of which emission maximum is located at 433 nm in CDs-COOH, 427 nm in CDs-OH

and 420 nm in CDs-NH_2, could be related to hydrogen bonding with water molecules as it follow the same order as the hydrogen bond strength.

3.5 Summary

In summary, this chapter investigates three types of CDs samples modified with carboxyl, amino and hydroxyl groups, and suggesting that the surface chemistry plays an essential role on CDs' optical, chemical and electronic properties. A detailed study on electronic structure of CDs is presented based on X-ray spectroscopies, and contributions from core and surface groups were described. The PL of three CDs was discussed based on the nature of electronic states in the bandgap region. Hydrogen bonds between CDs and water and pH-dependent PL spectra illustrate surface-dependent properties of CDs. While all exhibiting a blue luminescence, which could be related to the clear C=O signature in the core of all CDs, the results presented herein also demonstrate that surface chemistry could be used to finely tune CDs' acceptor/donor electronic states and hydrogen bonds behavior.

Chapter 4

Charge Transfer between Carbon Dots and Water

Content

The work presented in this chapter is taken from the published work Ren et al. [180], edits have been made to match the flow of the dissertation. Scientists from different institutes were involved in the submitted paper. Ren and Petit designed the experiments. Ren performed all spectroscopic measurements, analyzed the data, and wrote the initial draft of the manuscript. Achilleos synthesized all samples. Golnak, Xiao and Petit helped with the experiments in BESSY II and the data analysis. Yuzawa and Nagasaka helped with the experiments in UVSOR-III. Reisner helped with the sample preparation and discussed the results. Petit supervised the project.

4 Charge Transfer between Carbon Dots and Water

In the last chapter the electronic structure of carbon dots (CDs) has been characterized *ex situ* by synchrotron X-ray spectroscopies. However, most promising applications of CDs take place in aqueous environment. Therefore, the understanding of the modification on electronic structure of CDs by surrounding water molecules is of vital importance. In this chapter, three types of carbon dots with different core structures (amorphous vs. graphitic) and compositions (with vs. without nitrogen doping) were investigated by *in-situ* X-ray absorption spectroscopy (XAS) in water. The charge transfer between CDs and water molecules are uncovered. In addition, the hydrogen bonding interactions between water and the CDs' surface groups has been characterized previously by infrared spectroscopy. The structure of interfacial water around CDs dispersion also shows a significant impact on the charge transfer, which can be studied by probing water molecules using *in-situ* XAS. These investigations reveal the nature of the solid-liquid interface between CDs and water, and may provide guidance for developing efficient CDs for light harvesting and fluorescence imaging.

4.1 Motivation

As introduced in previous chapters, carbon dots (CDs) that are cheap, stable and efficient, have recently shown a great potential for artificial photosynthesis. Significant progress has been made in the development of CDs-based photocatalytic materials and heterogeneous systems in the last several years. [26,27,33] Reisner et al reported a facile method to prepare graphitic CDs, with (*g*-N-CD) and without (*g*-CD) core nitrogen doping as light harvester for photocatalytic hydrogen evolution reaction. [51] A significant improvement of the photocatalytic performance has been realized using *g*-N-CD thanks to the enhanced light absorption compared to amorphous CDs (*a*-CD) and higher extraction of photogenerated charges compared to undoped *g*-CDs. [51] Similar to conventional semiconductor photocatalytic materials, an essential feature influencing the activity of CDs-based photocatalysts is the nature of its surface/interface chemistry phenomena, especially the solid-liquid interface where transfer of electrons driving the target chemical reactions occurs. The electronic and chemical properties of this interface also govern the selectivity, rate, and overpotential of redox reactions on the material surface. [177] Identifying active sites that enable efficient charge transfer at the CDs surface is fundamental to benefit at most from their electron accumulation properties in the photocatalytic reaction. However, a direct spectroscopic characterization of the CDs-water interface under *in-situ* condition is still missing.

Although X-ray absorption spectroscopy (XAS) has been successfully applied *ex situ* on CDs and can provide detailed information on the local chemical and electronic structures of

the excited atoms, [137] the *in-situ* XAS measurement of CDs aqueous dispersion is still a great challenge in the soft X-ray range. This, as mentioned in Section 2.2.3, is restricted by the contradiction between the high vapor pressure of the liquid and the strict vacuum requirement for signal detection. [99–101] To surmount this technical obstacle, various innovative flow cell technologies, [102,105,178,179] using membranes to isolate the liquid phase from the vacuum, have been devised to realize the XAS measurement on liquid samples and nanoparticle dispersions.

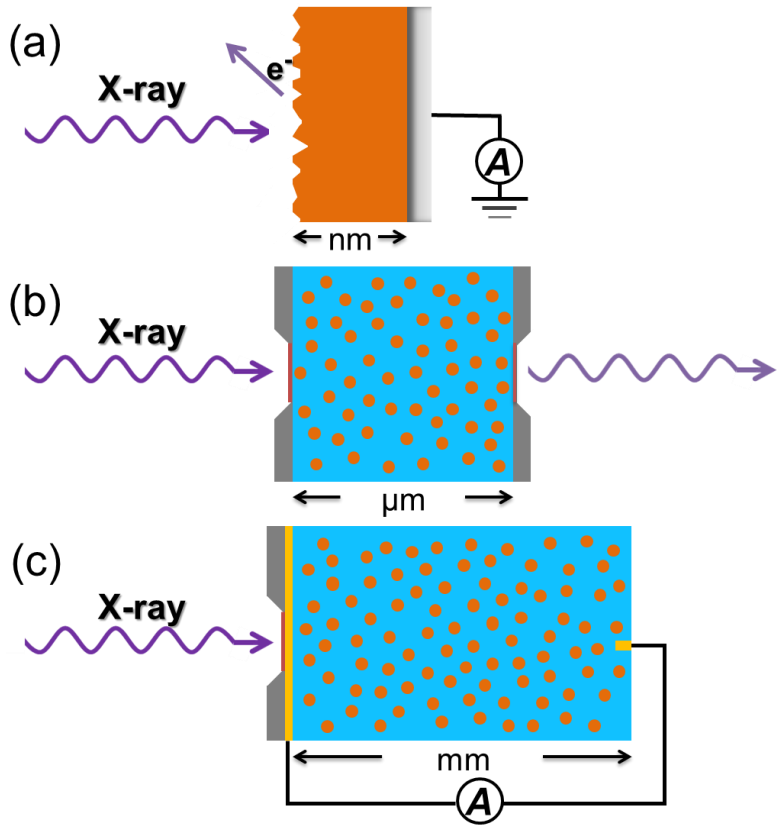

Figure 4.1 Schematic illustration of different XAS detection schemes: (a) TEY detection on solid materials in vacuum; (b) pure transmission and (c) TIY detection in CDs aqueous dispersion. Reproduced with permission from ref. [180], copyright 2019 American Chemical Society.

Experimentally, the true absorption cross-section of liquid samples can be measured in the transmission mode by detecting the incoming and transmitted light through the liquid sample. [105] On the other hand, the decays of core holes created in the X-ray absorption process enable the detection of fluorescence yield (FY) and electron yield (EY) to record XA spectra. As introduced in Chapter 2, the FY mode XAS measurement always suffers from very low emission probabilities (< 1%) compared to the EY detection for light elements such as carbon, nitrogen and oxygen. However, the short inelastic mean-free path of emitted photoelectrons (several nanometers) makes them impossible penetrate the conventional Si_3N_4

(or SiC) membranes of liquid cells and restricts the EY detection mainly on solid sample measurement. Recently, Xiao et al in HZB proposed another detection scheme for XAS measurement, total ion yield (TIY), in which the current induced by ionic species generated upon X-ray irradiation was detected. [102,103] The TIY measurement has been demonstrated to be bulk-sensitive and is currently in development to characterize pure solvent and ions. [102,103,181,182]

In this chapter, the first study of TIY-XAS application on dispersed nanomaterials is realized. The electronic structure of three CDs samples (*a*-CD, *g*-CD and *g*-N-CD) was characterized by XAS measured in total electron yield (TEY) on dry CDs in vacuum as well as transmission and TIY on dispersed CDs in water at the carbon K-edge. (**Figure 4.1**). The comparison between TEY, transmission and TIY measurements demonstrates that TIY measurement can be used for uncovering the charge transfer at the CDs-water interface and further provides new insights on the role that CDs played in the photocatalytic process. Furthermore, the hydrogen bonding environment of water molecules can be probed by transmission-XAS at the oxygen K-edge and has already been extensively applied on pure water, [183,184] aqueous solution [108,185] and colloidal dispersion [136,186]. The O K-edge XA spectra of the CDs dispersions at various concentrations were compared to characterize the hydrogen bonding network around CDs. By correlating these spectroscopic results to the photocatalytic performance of these CDs, we propose that *in-situ* XAS could be used to investigate charge transfer properties of photocatalytic materials directly in solution.

4.2 Electronic Structure of Solid Carbon Dots

First, the three CDs samples were drop-casted on a conductive silicon substrate and characterized by TEY mode XAS. The data were collected at the U49-2_PGM-1 beamline of the BESSY II synchrotron radiation source using the LiXEdrom end station. As shown in **Figure 4.2**, there are two sharp peaks (around 285 eV and 288.5 eV) with small features in between. The C K-edge TEY mode XA spectra were deconvoluted with Gaussian peaks to better estimate the energy of the various features observed. An inverse tangent background was used to take into account the photoionization potential at the carbon K-edge. The fitting details can be found in **Table 4.1**.

The feature A around 285 eV can be assigned univocally to the excitation of core electrons into $\pi^*_{C=C}$ orbitals. [137] The intensity of this feature is used to estimate the percentage of the C=C contribution in *a*-CD, which is lower than that of the other two graphitic CDs samples (**Table 4.1**). Since the C=C feature at 285 eV is often considered as the

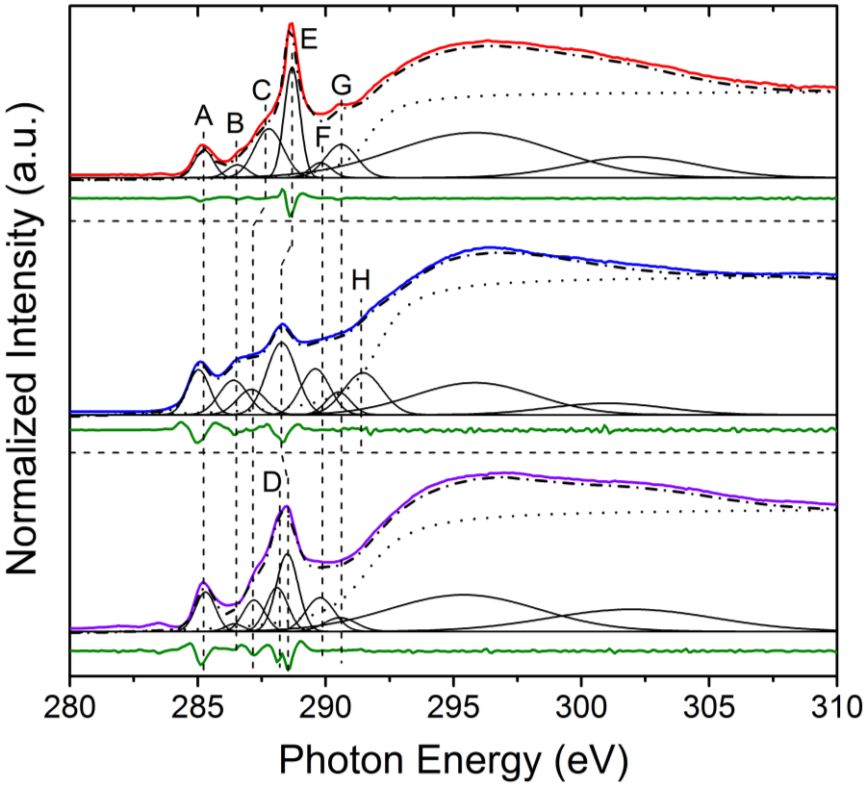

Figure 4.2 Deconvolution of the C K edge TEY-XA spectra of *a*-CD (red), *g*-CD (blue) and *g*-N-CD (violet). The second derivatives (oliver), different Gaussian peaks (solid), the resulting fit (dash dot) and the background (dot) are shown below the experimental spectra. The spectra are offset for clarity. Reproduced with permission from ref. [180], copyright 2019 American Chemical Society.

Table 4.1 Fitting details of the C K edge TEY-XA spectra of CDs samples. Reproduced with permission from ref. [180], copyright 2019 American Chemical Society.

Peak	*a*-CD		*g*-CD		*g*-N-CD	
	Energy [eV]	**FWHM [eV]**[a)]	**Energy [eV]**	**FWHM [eV]**	**Energy [eV]**	**FWHM [eV]**
A	285.24	0.87	285.14	1.02	285.28	0.98
B	286.55	0.96	286.48	1.33	286.43	0.79
C	287.78	1.33	287.20	1.33	287.25	1.00
D	/	/	/	/	288.10	1.00
E	288.69	0.72	288.38	1.37	288.50	1.00
F	289.80	1.00	289.70	1.33	289.78	1.32
G	290.61	1.46	290.60	1.14	290.57	1.45
H	/	/	291.57	1.77	/	/

[a)] Full Width at Half Maximum (FWHM) of Gaussian peaks.

graphitization degree of carbon nanomaterials, [187] this is in line with the previous observation from Raman spectroscopy. [51] The features B and C in the range of 286-288 eV can be assigned to the π^*_{C-C-O} transitions in oxygen-containing groups. [137,143] The sharp peak E at 288.5 eV is mainly assigned to the C 1s to $\pi^*_{C=O}$ transitions of the carboxyl groups, [137,187] which is confirmed by the previous infrared measurement. [51] A shoulder, feature F, observed at the right side of the main peak, originates from the C(O)=O moieties in carboxyl groups. [137] The features G and H are attributed to the electron transition from C 1s to σ* states in C–O and C–C bonds, respectively. [143] The broad features above the ionization potentials represents a large number of molecular orbital states. Strictly speaking, the two broad Gaussian components hold little physical significance but mainly for the mathematical visualization.

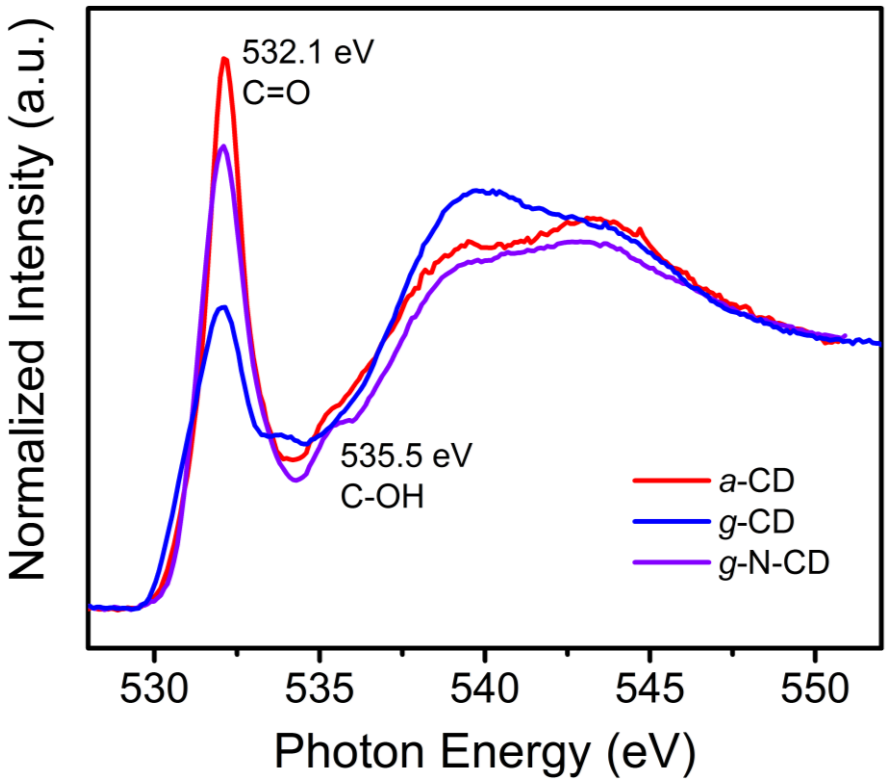

Figure 4.3 O K-edge TEY-XA spectra of of *a*-CD (red), *g*-CD (blue) and *g*-N-CD (violet). Reproduced with permission from ref. [180], copyright 2019 American Chemical Society.

The features shown in C K-edge TEY XA spectra can be supported by the XA spectra measured at O and N K-edges. In **Figure 4.3**, a sharp peak is shown at 532.1 eV, and can be attributed to the C=O bonds. It should be noted that this C=O feature appears at a lower energy position compared to that shown in Chapter 3, which indicates that these C=O feature have two different chemical environment. The CDs samples introduced in previous chapter possess an oxygen-rich carbogenic core, whereas the core of three CDs samples shown herein

are predominantly composed of carbon, and the C=O bonds mainly appear on the surface. In other words, the peak at 532.1 eV and the shoulder at 535.5 eV for the O 1s → π^*_{C-OH} confirm the rich existence of surface carboxyl groups of three CDs.

The shift and broadening of the peak at 288.5 eV observed in *g*-N-CD (**Figure 4.2**) was attributed to the additional contribution of C–N bonds (288.1 eV, Feature D) close to the C=O feature (288.5 eV, Feature E). In agreement, a predominant pyridinic contribution was detected at 399.7 eV in the nitrogen K-edge XAS spectrum (**Figure 4.4**). [137] Another contribution in the N K-edge spectra centered at 401.7 eV may correspond to the quaternary N incorporated in six-fold aromatic cycles, including pyrimidine. These results confirmed the success of nitrogen incorporation occurs in the core of *g*-N-CD. As introduced in Chapter 1, nitrogen doping has a great influence on the electronic structure of carbon nanomaterials. Numerous studies have confirmed that a localized density of states appears in the occupied region near the Fermi level of the carbon atoms adjacent to pyridinic nitrogen atoms, and thus suggests that carbon nanostructures containing pyridinic N possess Lewis basicity, [188–190] which is beneficial for the photoreduction of water to hydrogen. [69]

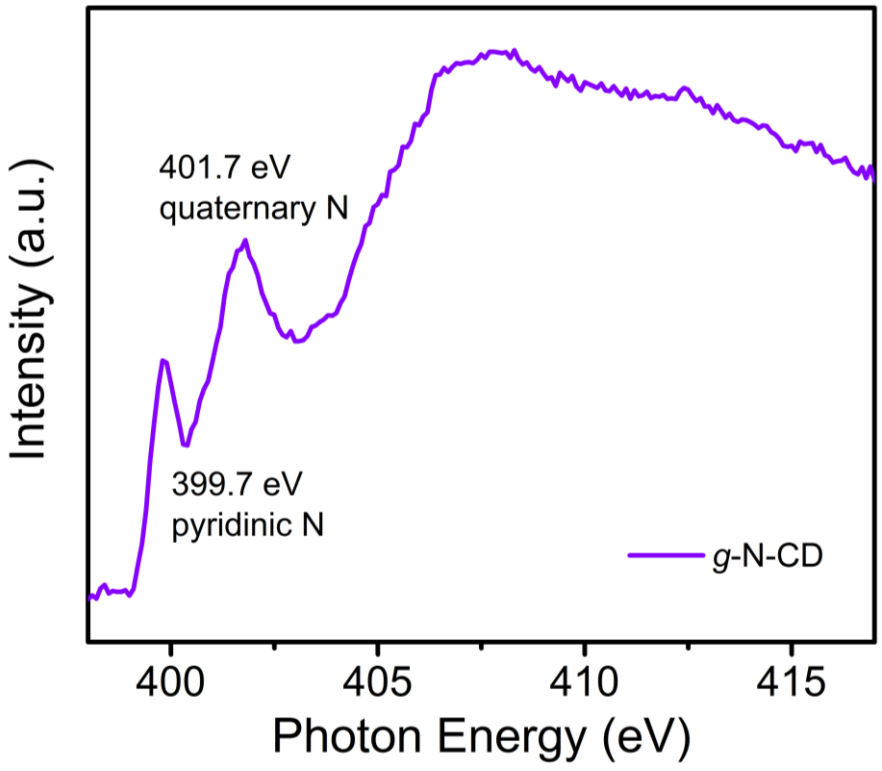

Figure 4.4 N K-edge TEY-XA spectrum of *g*-N-CD. Reproduced with permission from ref. [180], copyright 2019 American Chemical Society.

Now, by comparing all TEY-XA spectra showed above and in Chapter 3, the general characteristics shown in the absorption spectra of CDs can be briefly summarized. First, rich

features can be observed from carbon K-edge, which generally contains the transition related to $\pi^*_{C=C}$ at 285 eV, $\pi^*_{C=O}$ at 288.5 eV and oxygen-containing groups in the range of 286–288 eV. Secondly, the same group may appear at different peak positions due to the presence of different chemical environments, just like the above-mentioned C=O feature. Thirdly, the features appear at a similar position should be carefully analyzed, such as the π^*_{C-N} and $\pi^*_{C=O}$ present around 288.5 eV in the C K-edge XA spectra.

4.3 Charge Transfer at Solid–Liquid Interface

After analyzing the TEY-XA spectra on solid CDs samples, the *in-situ* XA spectra at C K-edge will be discussed. The transmission- and TIY-XA spectra were respectively measured at UVSOR-III Synchrotron and BESSY II Synchrotron with different liquid cells as previously described in Section 2.2.3.

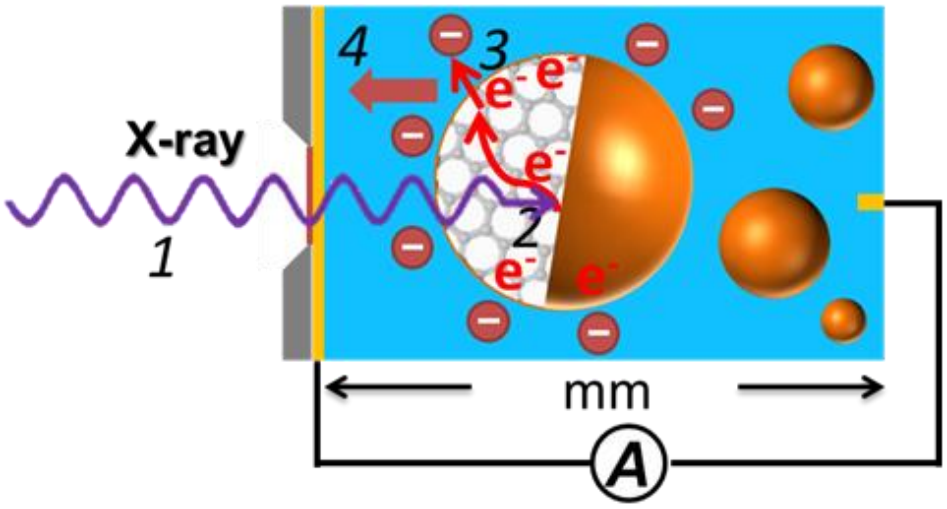

Figure 4.5 Schematic illustrations of the proposed mechanisms. 1: X-ray excitation, 2: electron transfer to the surface, 3: charge transfer to water, 4: diffusion of ions to the electrode. Scales are not reproduced for clarity.

For the transmission-XAS measurement, the detection mechanism, which measures the true absorption cross-section of liquid samples, is simple and clear. However, the measurement on the nanomaterials in liquid phase using the TIY mode XAS is reported for the first time, and thus it is necessary to introduce the new detection scheme before going into the experimental results. **Figure 4.5** shows the proposed mechanism of TIY-XAS. Upon scanning the absorption edges of the targeted element, the core electrons will be excited into the unoccupied states, then excited electrons and secondary electrons from the core-hole relaxation transfer to the sample surface, and some of them leave the surface. Charge carriers are thus formed in the liquid, and then diffuse to the electrode. The TIY-XA spectra can thus be

obtained by directly measuring the drain current between the two electrodes (gold-coated Si_3N_4 membrane and platinum rod). Therefore, the detected TIY signal carries rich information on both unoccupied states of specific absorber atom species and the charge transfer between the solid sample and water.

In the TIY detection, there is no external potential applied to the liquid cell. However, with incident X-ray irradiation, the incoming photons lead to an ejection of photoelectrons from the Si_3N_4 membrane to the vacuum. [182] A background signal can be observed due to the potential difference between the charged Si_3N_4 membrane and the counter electrode, which also offers the driving force for the detected ionic current.

Considering their isotropic and spherical feature, the origin of the detected ionic current is straightforward for the previous TIY-XAS measurement on ions. When the sample varies from ions to dispersed nanoparticles, the surface-sensitivity of the TIY detection due to the short mean free path of electrons will play a role in the photoelectron-transfer process. For CDs samples, their sizes (3–8 nm) are equal to or even larger than the mean free path of electrons (about 3 nm). As a result, some electrons generated in the carbon core upon X-ray irradiation would be difficult to emit out. Additionally, there are more than one species existing in CDs samples as shown in the TEY-XA spectra. Take the carbon atoms as an example, some chemical bonding are mostly present in the core, while others are probably found on the surface. This means that the spectral features of the TIY-XAS are not only influenced by the local environment but also by the electron-transfer process. As a consequence, one can expect that the higher intensity a feature appears, the more electrons escape through it. This can help to identify the charge transfer channel from the TIY-XA spectra. When the electrons emit out from the sample, it may be hydrated by a few water clusters and transport through the bulk liquid, and the ionic current is thus generated. Note that, the identification of the possible charge carriers remains currently an open question and calls for further investigations to determine the ionic species.

It should be pointed out that, the TIY detection is very sensitive to small disturbances. Unsteady current fluctuation can be observed when the liquid is flowing inside the cell, which indicates that the detected current is originated from the ion transport through the bulk liquid. Therefore, the flow of liquid sample is stopped for at least 30 minutes before the experiment, and the sample is kept static during the experiment.

The comparison of different detection schemes on three CDs samples are shown in **Figure 4.6**. Since it detects photons, the transmission-XA spectra of liquid samples present the information of CDs samples with both carbon core and surface groups. TEY and TIY are electron yield measurement and surface-sensitive, where the core features would not be as

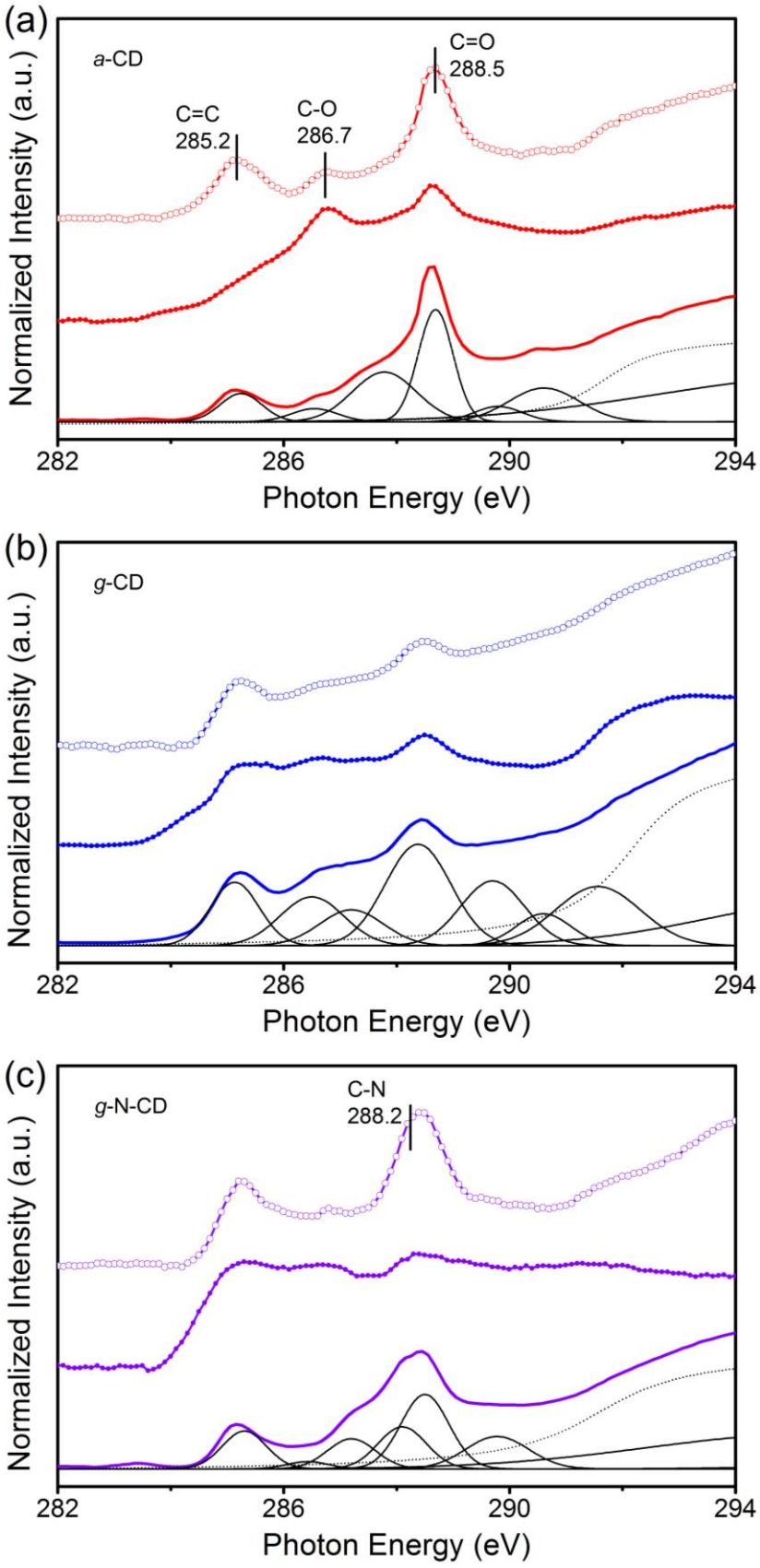

Figure 4.6 TEY-XA spectra (line) on dry CDs in vacuum, TIY- (line+solid circle) and transmission-XA spectra (line+hollow circle) in aqueous CDs dispersions at the C K-edge of (a) *a*-CD, (b) *g*-CD and (c) *g*-N-CD. The deconvoluted peaks of the TEY-XA spectra are also plotted. Reproduced with permission from ref. [180], copyright 2019 American Chemical Society.

pronounced as those in transmission-XAS. However, it should also be note that the detected ionic current in TIY-XAS stems from the bulk solution in the liquid cell and thus carries the information of the bulk solution, especially the interaction between CDs and surrounding water molecules.

A clear distortion of the C=C peak is observed in the TIY-XA spectra compared to TEY- and transmission-XA spectra. In *a*-CD, the C=C signal is very weak and might be obscured by the tail of the C–O feature. Unlike *a*-CD, however, the C=C feature is clearly distinguishable on TIY-XA spectra of graphitized samples. We interpret the different signature of *a*-CD as a result of the nature of the detected signal in TIY-XAS. In the amorphous core of *a*-CD, sp^2-hybridized carbon atoms are mainly found in small islands isolated into an amorphous carbon matrix. The sensitivity of transmission mode XAS to short-range ordering in the material (a few atoms), [93] makes the C=C signature of *a*-CD clearly visible as of graphitic samples. For TEY-XAS, the detected signal also depends on the photoelectron emission yield of the material, and is in most cases close to the real transmission-XAS, [93] as observed here. On the other hand, for TIY-XAS, the formation of stable ionized specied is needed to induce an ionic current between the two electrodes of the flow cell (**Figure 4.1**).

Since the energy needed to excite carbon atoms (>284 eV) is below the energy required to excite oxygen in water molecules (>534 eV), the selective X-ray excitation of CDs is possible and the solvent is not directly ionized. When the CDs in the aqueous dispersion are excited by the incident X-ray at the carbon edge, an efficient charge separation in the CDs and a charge transfer to water molecules is required to induce an ionic current that can be detected. TIY-XAS therefore acts as an energy-dependent probe of charge transfer from CDs to solvent which enables site-selectivity across the carbon K edge.

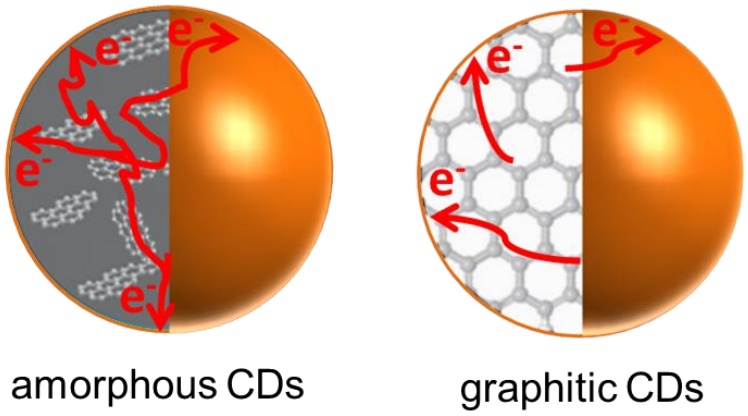

Figure 4.7 Schematic illustration of the transport of photoelectrons in amorphous and graphitic CDs.

From our results, it seems that photoelectrons emitted from C=C bonds in *a*-CD are not able to be efficiently transferred to surrounding water molecules. This is different from

C=C bonds in *g*-CD and *g*-N-CD, which are mostly found in ordered graphitic planes, as previously demonstrated by XRD and HRTEM. [51] As illustrated in **Figure 4.7**, electrons move faster in graphitic planes than in amorphous matrix due to the high degree of π–π stacking in graphitic carbon core. In contrast, the random orientation in amorphous carbon cores hinders connectivity between conjugated backbones; and thus hinders the electron transfer. The charge transfer process occurring in TIY-XAS is of a similar nature with that in the photocatalytic process. As introduced in Chapter 1, in the photocatalytic process electrons (in valence states) are excited upon UV or visible light irradiation, and then transfer to the surface (or surrounding catalyst) and participate in the reaction. The rapid electron-transfer of graphitized CDs underlies the high photocatalytic performance previously reported in combination with a molecular catalyst. [51,141]

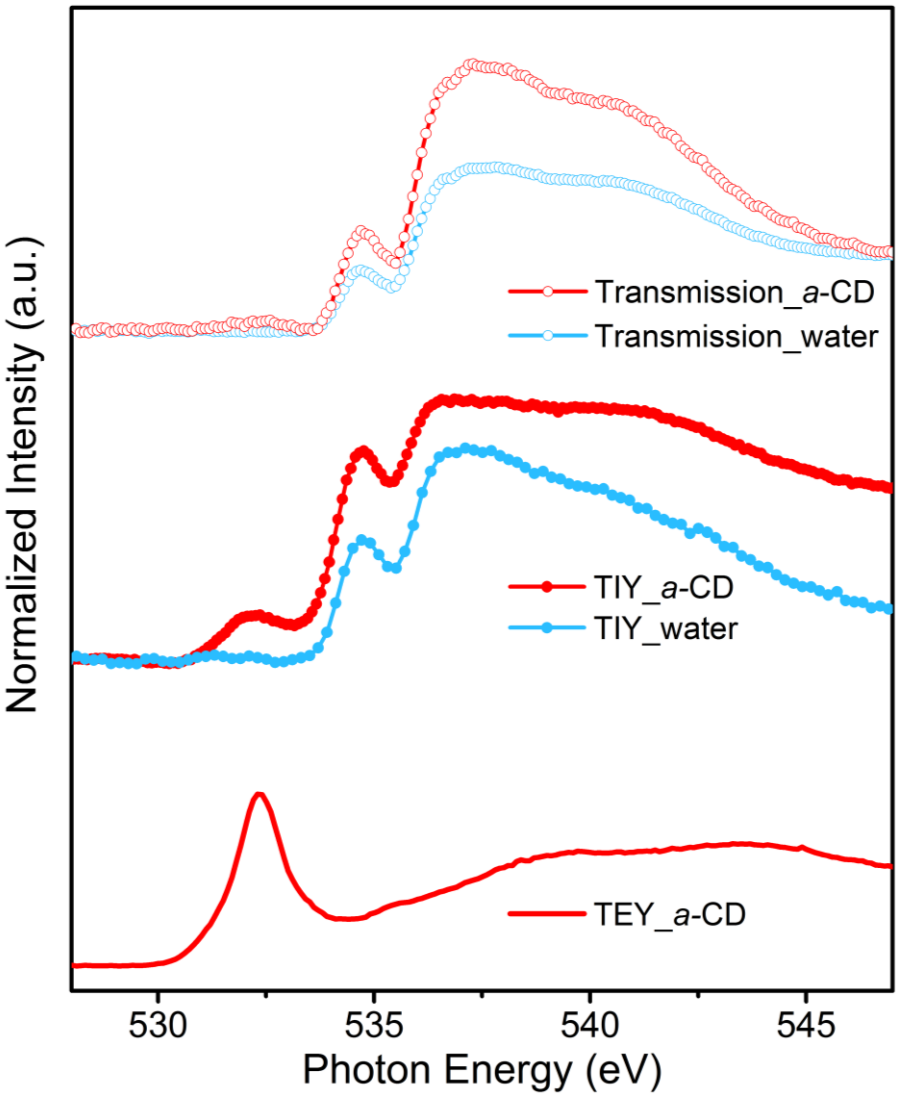

Figure 4.8 O K-edge TEY-XA spectra of three CDs samples (below) and O K-edge TIY-XA spectra of *a*-CD, *g*-N-CD and water. Reproduced with permission from ref. [180], copyright 2019 American Chemical Society.

The peak intensity in the range of 286-288 eV increases in the *in-situ* measurements compared with the TEY-XA spectra, especially in the TIY-XA spectra. Meanwhile, the sharp feature of C=O group exhibits a decrease in C K-edge TIY-XA spectra. These results confirm the deprotonation of carboxyl groups in water. Together with its emergence below the water edge in the TIY-XA spectra at the O K-edge (**Figure 4.8**), it indicates that the surface carboxyl groups act as the channel for electrons transfer between CDs and water molecules.

The features shown at O K-edge also vary among three XAS detection schemes. Different from the TIY-XA spectra, the contribution from C=O bonds in CDs appears to be negligible on transmission-XA spectra of *a*-CD below the water edge (**Figure 4.8**), which suggests that the transmission-XAS is not a suitable method to analyze the charge transfer between colloidal with surrounding solvent molecules.

The probing depth of the X-ray is about 10 μm below the water edge, and shows a dramatic decrease (less than 1 μm) at the resonant excitations. In TIY-XAS, the probing depth is much smaller than the cell size in both cases. But in transmission cell, to ensure the detection of water, the sample thickness is only a few hundred nanometers. Thus, the amount of CDs detected in transmission cell is much smaller than that in TIY cell. When scanning the incoming photon energy across the water O K-edge, the water molecules detected in both cells are almost the same. As a result, the intensity of the pre-edge in TIY-XA spectrum is so high relative to the water, compared to transmission-XAS.

However, the transmission-XAS is sensitive to the change in the sample concentration and moreover, the measurement at O K-edge can be used to identify the structure of interfacial water around CDs.

4.4 Interfacial Water Structure around Carbon Dots

The oxygen K-edge of three different CDs dispersions were then compared to pure water using transmission mode XAS, as shown in **Figure 4.9**. Typical water XA spectra consist of a pre-edge at 534.7 eV, a main edge around 537 eV and a post-edge at 540 eV. [183] The overall X-ray absorption is higher for CDs dispersions than pure water but also differs with the samples. The intensity of the pre-edge feature of *a*-CD is as strong as that of *g*-N-CD, whereas the intensities of the main- and post-edges of *a*-CD are stronger. For *g*-CD, these three features are weaker than those of the other two CDs samples.

The differences shown in the O K-edge XA spectra between CDs dispersions with water can be interpreted in terms of modification of the hydrogen bonding network of water molecules surrounding CDs. As investigated in previous XAS studies of bulk water, [191,192]

the pre-edge feature originates from unsaturated or dangling hydrogen bonds observed in liquid phase, the main edge is also related to the population of molecules with unsaturated hydrogen bonds, while the post-edge region is associated with the fully saturated hydrogen bonding network. In bulk ice, the pre- and main-edges are weaker compared to liquid water since all hydrogen atoms in ice participate in hydrogen bonds, while the post-edge is stronger than that of water. The interfacial water layers around nanoparticles dispersed in an aqueous environment forms a partially saturated hydrogen bonding network, which can be considered as the mixture of liquid water and ice.

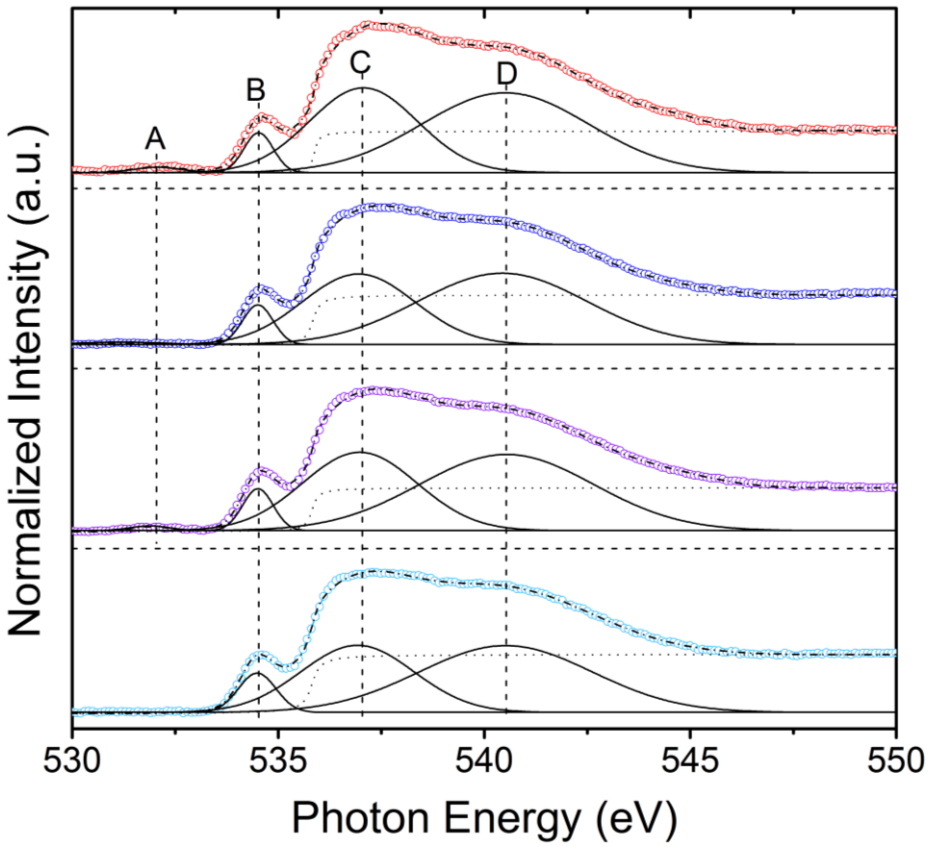

Figure 4.9 Deconvolution of the O-K edge transmission mode XA spectra of *a*-CD (red), *g*-CD (blue), *g*-N-CD (red) aqueous dispersions at 8 wt% and pure water (turquoise). The different Gaussian peaks (solid), the resulting fit (dash dot) and the background (dot) are shown below the experimental spectra. The experimental spectra are offset for clarity. Reproduced with permission from ref. [180], copyright 2019 American Chemical Society.

To compare the influence on the hydrogen bonding network of water molecules from the CDs samples, the pre/main-edge ratios were calculated from the fitted oxygen XA spectra (**Figure 4.9**). The pre/main-edge ratio of pure water spectra remains constant as 19.5%. The pre/main-edge ratios at 8 wt% concentration of *a*-CD, *g*-N-CD and *g*-CD represent 37%, 28% and 22% decreases compared to the same ratio calculated for pure water (**Table 4.2**) which

confirms the contributions of both bulk water and the interfacial water around CDs in the oxygen K-edge spectra. The distinctive results of the pre/main-edge ratio represent the different hydrogen bonding networks around CDs, which can be influenced by the concentration, the nanoparticles size, and the surface termination of the CDs.

Table 4.2 Fitting details of the O K edge transmission mode XA spectra of CDs samples at 8 wt%.

Peak	Energy [eV]	FWHM [eV]	Area			
			a-CD	*g*-CD	*g*-N-CD	water
A	532.16	1.14	0.0160	/	0.0318	/
B	534.51	0.87	0.0982	0.1524	0.2156	0.1366
C	536.98	3.28	0.7982	1.0030	1.5294	0.7007
D	540.49	4.95	1.1271	1.5256	2.2405	1.0723
Pre/Main edge [%][a)]			12.3	15.2	14.1	19.5

[a)] This is calculated from the area ratio of Peak B and Peak C.

To confirm the strong impact of three CDs on the water structure, the evolution of oxygen K-edge XA spectra at various concentrations was probed. The deconvolutions of experimental spectra are presented in Appendix, the pre-/main-edge ratio of each spectrum were calculated from the deconvolution and displayed in **Figure 4.10**, and the normalized spectra are shown in **Figure 4.11**.

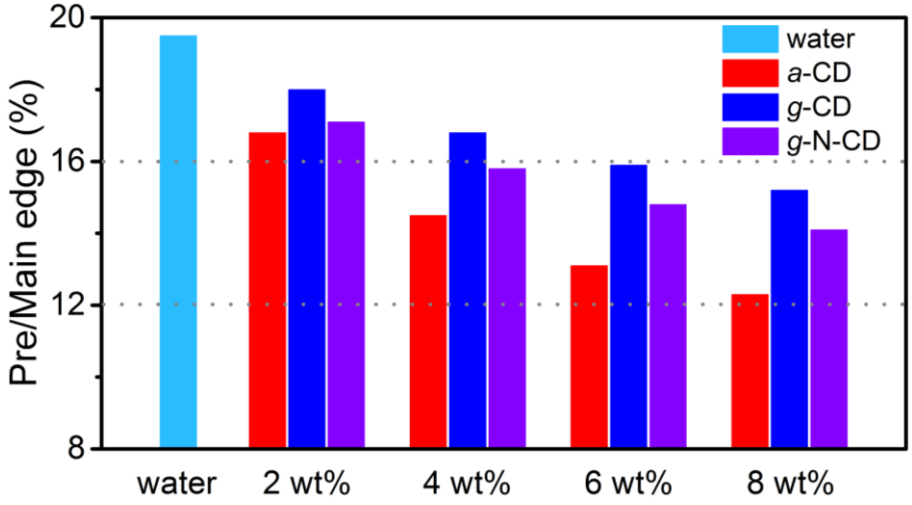

Figure 4.10 The Pre/Main-edge ratios for each spectrum.

The absorptions in the pre-, main- and post-edge regions increase with *a*-CD concentrations from 2 wt% to 8 wt% (**Figure 4.11**a). The larger spectral change shown in the

a-CD dispersion can be partially attributed to its larger sizes (6.8±2.3 nm) compared to the other

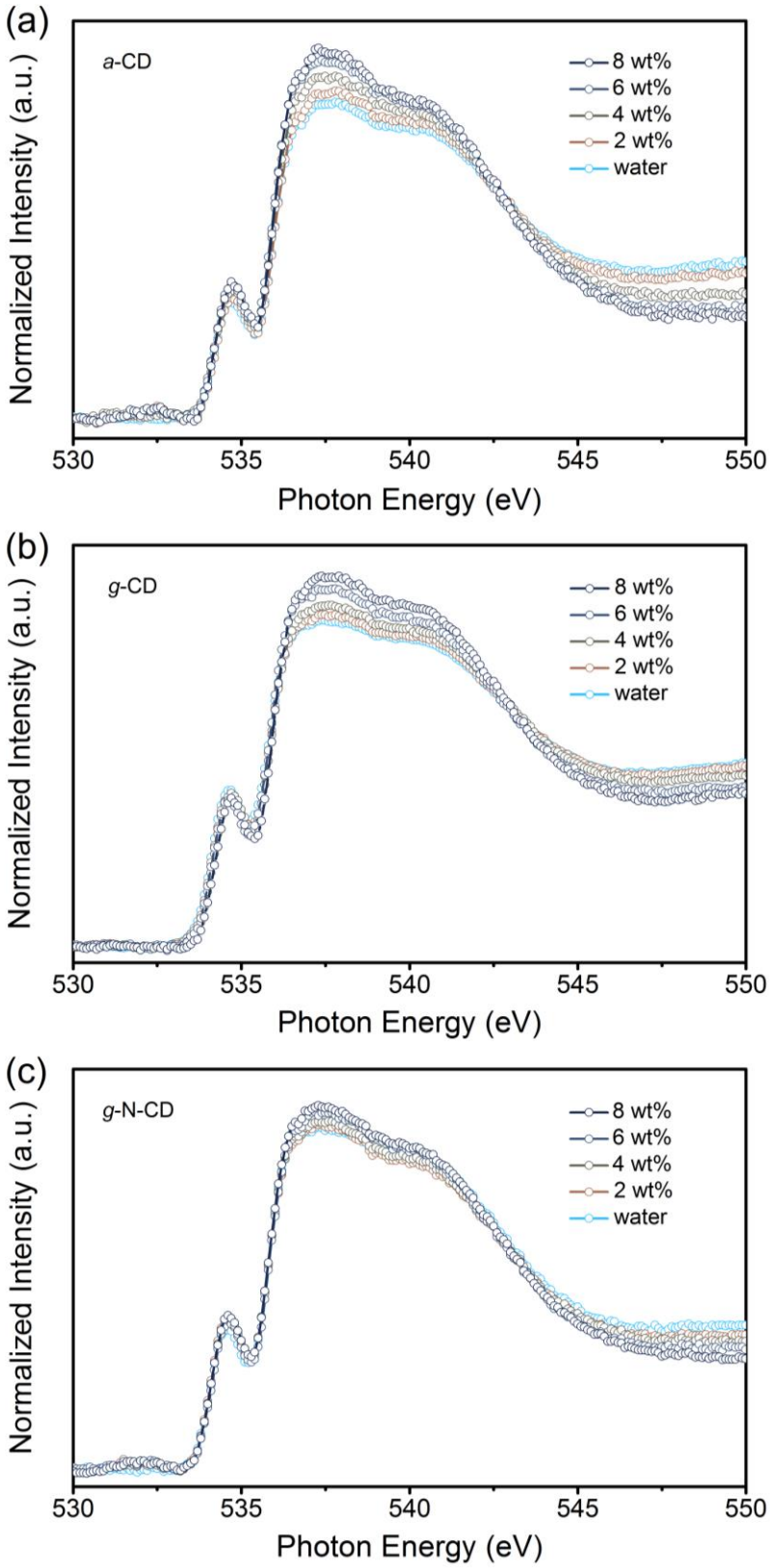

Figure 4.11 Transmission mode XA spectra at oxygen K-edge from (a) *a*-CD, (b) *g*-CD and (c) *g*-N-CD at different concentrations. The spectra are normalized to their integrated area. Reproduced with permission from ref. [180], copyright 2019 American Chemical Society.

CDs samples (3.1–3.6 nm). [51] The hydrogen bonding networks induced by nanodiamonds of similar size as *a*-CD have been previously determined to extended over several solvation shells. [186] Similarly, *a*-CD molecules are large enough to distort the hydrogen bonds beyond the first solvation shell. In the same time, the original donor, C–O groups of *a*-CD, would interact with the new acceptor water molecule from the second coordination shell to form an enhanced hydrogen bond. [193] Due to this arrangement, more bulk water molecules are involved in the formation of hydrogen bonds, leading to the increased absorption of the pre-edge feature. This strong interaction between the *a*-CD and water molecules can also be confirmed by the pronounced C–O features shown in the *in-situ* XA spectra at carbon edge (**Figure 4.6**a).

For *g*-CD, XA spectra exhibit a prominent increase at the main- and post-edges with increasing concentration, while the pre-edge feature is only slightly changed (**Figure 4.11**b). The quenching of the pre-edge feature may result from the small size of *g*-CD (3.6 ± 1.0 nm), resulting in a higher amount of interfacial water, poorly contributing to the pre-edge. It should be noted that the *g*-CD samples were synthesized using the same precursor as *a*-CD, but at a higher calcination temperature to induce graphitization. The amorphous structures generally possess larger sizes with a non-uniform distribution than well-graphitized samples. For *g*-N-CD, the presence of nitrogen doping facilitates the emission of electrons and thus induces strong polarization of the CDs surface. Because the water molecule has a strong dipole moment, the surface polarization orients water molecules with oxygen sites pointing toward the CDs surface, leaving two hydrogen atoms available for the dual hydrogen bond motif. As such, our results suggest that a more structured long-range change of water organization (resembling amorphous ice) is formed around CDs with nitrogen doping. The changes of the hydrogen bonding network of the water molecules around the CDs induced by hydration may also be important for the effective charge transfer shown in *g*-N-CD as compared to *g*-CD. From these spectroscopic studies, it appears that Lewis basic carbon sites and structured interfacial water layer are generated by the graphitization and nitrogen doping of the CDs core. Together with the enhanced light absorption and the facilitated electrons transfer, *g*-N-CD exhibits superiority to enhance photocatalytic hydrogen evolution by acting as conductive channels, efficiently separating the photogenerated charge carriers.

4.5 Summary

This chapter shows a direct spectroscopic evidence of the impact of carbon core structure on the charge transfer properties of CDs dispersed in water. In particular, we evidenced that

efficient charge transfer to water occurs upon excitation of C=C bonds from CDs with graphitized core but not from CDs with amorphous core. To this aim, we performed *in-situ* XAS measurements at the carbon K-edge by detecting the ionic current in aqueous CDs dispersion generated upon X-ray irradiation. Distinctive electronic structures of CDs originated from their different structural and chemical natures were confirmed by comparing XAS measured with ionic yield to transmission and electron yield detections. Furthermore, change of water hydrogen bonding network around CDs, probed at the oxygen K-edge, was also found to depend on the CDs core structure. Ionic yield detection of XAS is a promising new method to probe photoactive sites on dispersed nanoparticles with element- and site-selectivities that may facilitate the design of new photosensitizers and photocatalysts.

Chapter 5

Heteroatoms Doped Polymeric Carbon Nitride

Content

The work presented in this chapter will be rewritten into a peer-reviewed paper. Scientists from different institutes were involved in this project. Ren and Petit designed the experiments. Ren performed the spectroscopic measurements, analyzed the data. Lin synthesized all samples. Wang helped with the sample preparation and discussed the results. Lieutenant, Schulz, Wong and Petit helped with the RIXS measurements in BESSY II. Petit supervised the project and discussed the results.

5 Heteroatoms Doped Polymeric Carbon Nitride

The previous chapter exhibited an example on the electronic structure modulation by introducing heteroatoms into carbon dots. Herein, the roles of dopant in polymeric carbon nitride (PCN) materials will be uncovered using various spectroscopies. The polymeric carbon nitride consists solely of an assembly of C–N bonds with a small amount of hydrogen on the terminating edges. The simple chemical composition and bonding mode in pristine PCN characterize it as a wide-band semiconductor. As introduced in Chapter 1, doping has been a widely applied method to tune band gap of PCN materials in order to facilitate light absorption that could result in enhanced photocatalytic activity. In this chapter two types of PCN materials with different dopants (sulfur and iron) are first introduced. The investigation of their influence on the electronic structure would be then presented and discussed.

5.1 Motivation

As introduced in Chapter 1, PCN has attracted much attention as a promising metal-free photocatalyst in the past decade. However, the photocatalytic activities of pristine PCN materials remain moderate because of the large optical bandgap, low electric conductivity and rapid rate of charge-carrier recombination. [194] Introducing heteroatoms in to PCN molecules can effectively modulate the electronic structure of PCN materials and enhance their activity. So far, there have been plenty of studies on the introduction of various anions and cations into the frameworks of carbon nitrides. Previous studies on the doped PCN materials focused on their enhanced photocatalytic performance but the underlying information of electronic structure were ignored. Ultraviolet and X-ray-based spectroscopic techniques can be helpful to provide such information. The investigations would thus offer us new insight on the roles of dopants on the electronic structure of PCN materials for designing more effective visible-light-driven photocatalysts.

Sulfur-doped PCN is first prepared via the thermal treatment of pure PCN powder in gaseous H_2S atmosphere. [195] The resulting S-doped PCN exhibits an extended light absorption and enhanced H_2 evolution performance. Another way to prepare the S-doped PCN material is to make use of the polymeric nature of PCN materials by co-polymerizing melamine with a sulfur-containing precursor (e.g., trithiocyanuric acid). [66,196] The similar electronegativity of sulfur (2.58) and carbon (2.55) makes it practically favorable to substitute carbon atoms rather than nitrogen atoms in the PCN structure, resulting in the formation of S–N bonds via thermal polycondensation of thiourea. [197]

Iron-doped PCN was reported right after the emergence of PCN photocatalyst as a typical example for the heteroatom modification. [65,198,199] Fe-doped PCN was synthesized

using dicyandiamide ($C_2H_4N_4$) and ferric chloride ($FeCl_3$) as precursors in a polycondensation reaction. [65] The Fe–N bonds are homogeneously formed in the PCN matrix and result in an enhanced visible-light-absorption of the obtained Fe-doped PCN materials.

The photocatalytic performance of doped PCN materials is always enhanced with a proper amount of dopant. Take the S-doped PCN that synthesized by using trithiocyanuric acid as the precursor as an example. The S-doped PCN samples exhibited an improved activity in H_2 evolution reaction over pristine PCN, and the photocatalytic activity varied with changing the condensation temperature. The maximum of the H_2 evolution rate was 140.5 μmol h^{-1} realized at 650 °C, and then slightly decreased to 138.6 μmol h^{-1} at 700 °C. [66] The Fe-doped PCN sample has demonstrated superior photocatalytic reactivity for the oxidative degradation of various organic dyes. [65]

In the present study, four samples are discussed in two different groups. In each group, there is one PCN with S or Fe doping, the other one is the pristine PCN sample synthesized under the same condition as the doped samples. The samples were synthesized by the group led by Prof. Xinchen Wang in Fuzhou University (China) using the method described in references [65,196]. The doped samples are named as X-PCN, and the reference samples are referred to as PCN(X), where the X represents the heteroatom, i.e., S or Fe.

5.2 Identification of Dopant Species

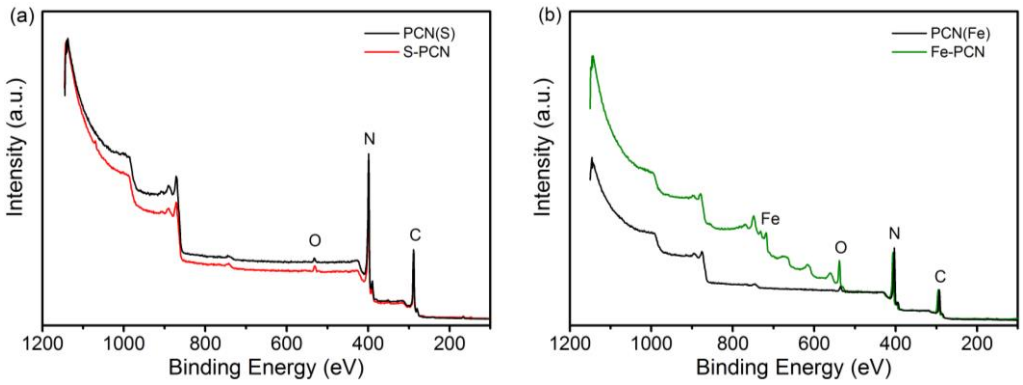

Figure 5.1 XPS survey of PCN(X) and X-PCN, X=S (a), Fe (b).

The chemical and electronic properties of doped PCN are first studied by XPS. A tiny spectral shift can also be observed in the XPS survey (**Figure 5.1**) between the doped and pristine PCN samples. From the XPS survey spectra of doped PCN samples and the corresponding references, it clearly shows that the oxygen contents are negligible except for the Fe-PCN sample. Therefore, the high-resolution XPS spectra were only measured for C and N 1s electrons. (**Figure 5.2** and **5.3**) For the undoped PCN, all C 1s core-level XPS spectra possess

one strong and two weak features which are attributed to C=C at ~284.6 eV, C–O at ~286.3 eV and C–N bonds at ~288.4 eV. In N 1s spectra of the undoped sample, the fitting also yields three features, which are the N in the triazine ring (C–N=C) centered at ~398.2 eV, the N–C_3 structure at ~399.8 eV, and pyrrolic N structure at 401.4 eV.

Figure 5.2 shows the C 1s and N 1s XPS spectra of S-PCN and its reference sample PCN(S). In C 1s spectra, a C–S feature can be clearly observed for S-PCN. The identification of C–S bond is maintained since this structure is inherited from the precursor, trithiocyanuric acid. Additionally, the –SH groups in trithiocyanuric acid can act as the leaving groups just like –NH_2 in melamine during the polycondensation, and thus the sulfur atoms involve in the polycyclization joining the heterocyclic rings or the tri-*s*-triazine moieties and partially take the place of nitrogen atoms. As a result, the percentage of N–C_3 feature is accordingly decreased in the N 1s spectrum of S-PCN.

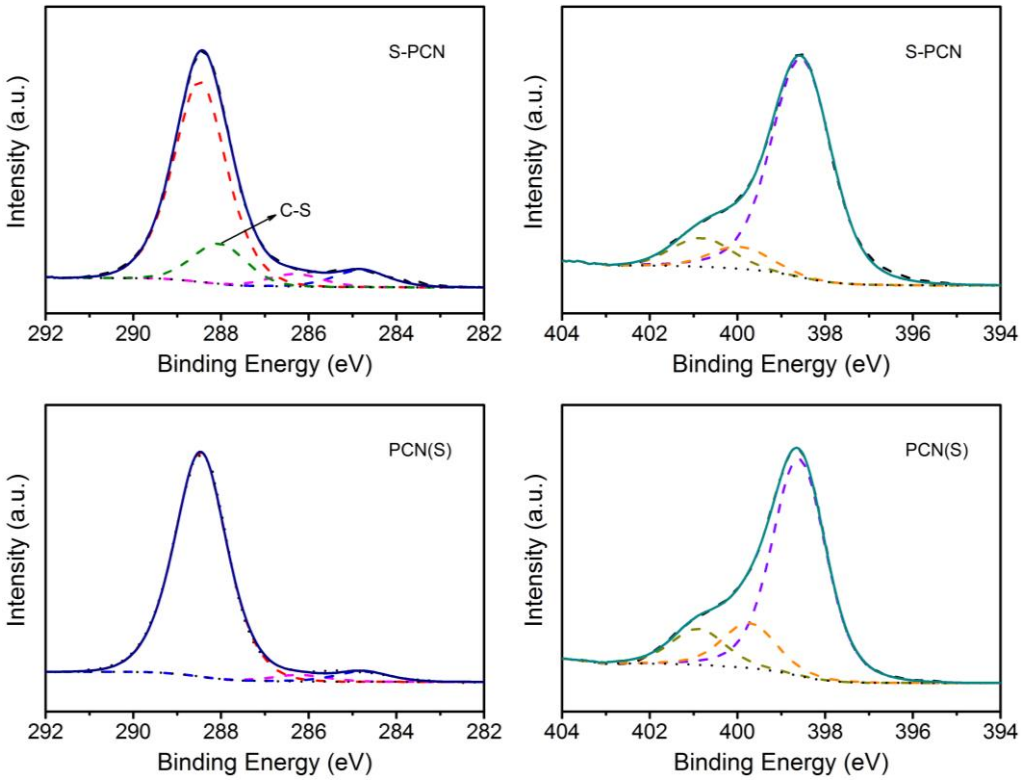

Figure 5.2 (a) C1s and (b) N1s XPS of PCN and S-doped PCN. The dotted line and dash-doted line indicate the fitted result and the Shirley-type background, respectively. The dashed curve is fitted using Voigt-shaped (30% Gaussian) function after background subtraction.

Figure 5.3 shows the high resolution XPS spectra of Fe-PCN and PCN(Fe). The precursors are different for the preparation of PCN(Fe) and PCN(S), but the XPS results are quite similar, especially in C 1s spectra. These results indicate that, the obtained PCN are also very similar in their molecular structures. One extra feature is shown in both C 1s and N 1s

XPS spectra of Fe-PCN compared with pristine PCN materials. The one shown in N 1s XPS can be attributed to Fe–N, thus leading to the destruction of the existing C–N bonds. Therefore, one more C–N configuration is generated in PCN(Fe). In addition, the cleaved ring forms energetically unfavorable dangling bonds that easily interacts with oxygen. In the C 1s XPS of Fe-PCN, the feature around 286 eV becomes more intense in Fe-PCN, which is the overlain of C–NH_2 (286.3 eV) and C–O (286.2 eV). This result coincides with the high oxygen content shown in the XPS survey spectrum.

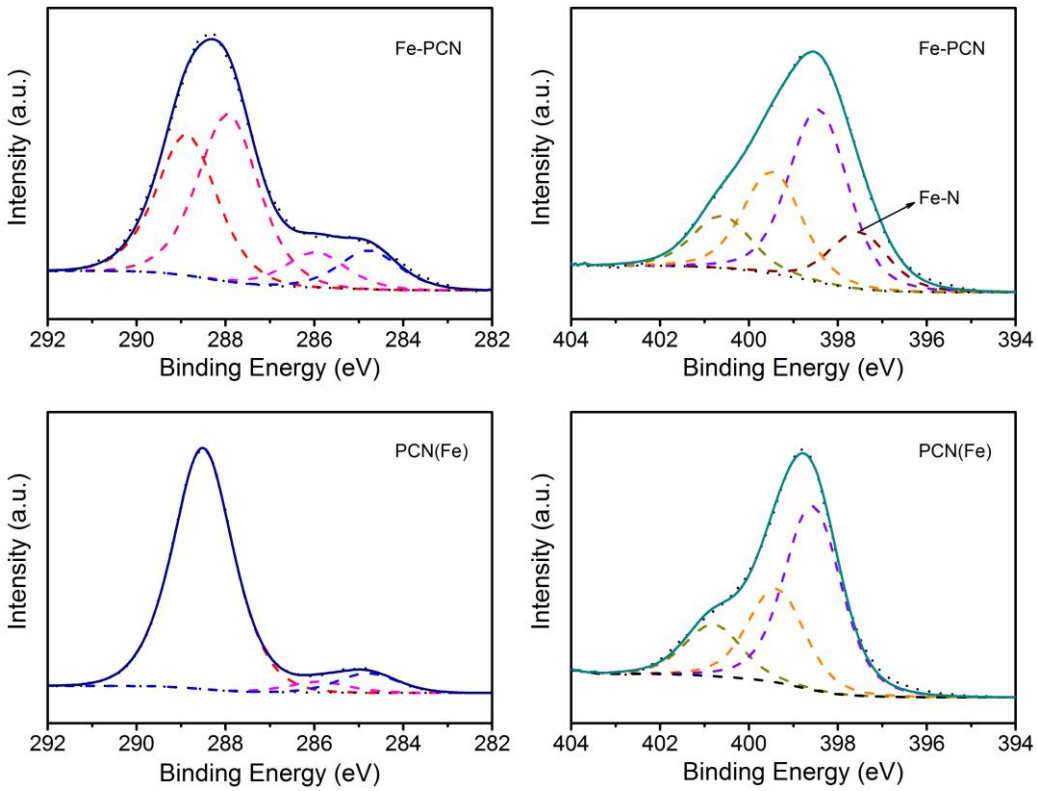

Figure 5.3 (a) C1s and (b) N1s XPS of PCN and Fe-doped PCN. The line types in the spectra are same as that shown in Figure 5.2.

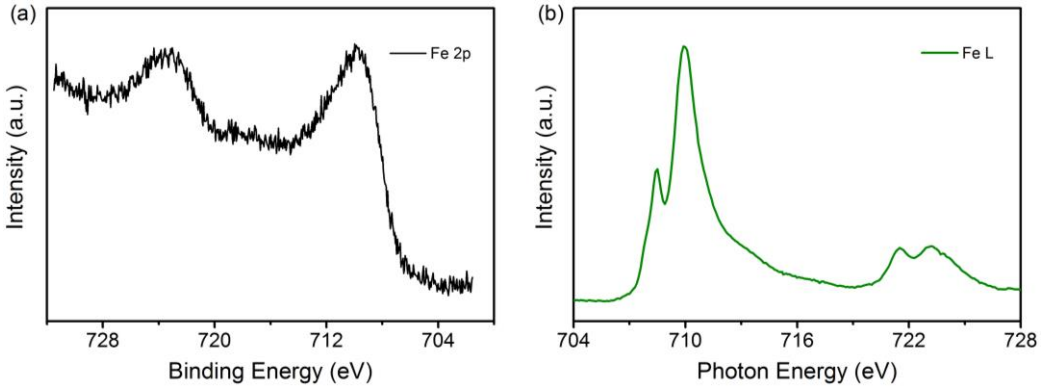

Figure 5.4 Fe 2p XPS and L-edge XAS of Fe-PCN.

Due to the low photon flux, it is difficult to measure the high resolution XPS for sulfur,

especially with a low concentration in the doped PCN materials. Iron, however, can be easily detected by XPS on Fe-PCN sample (**Figure 5.4**a). The XPS spectra of Fe^{2+} and Fe^{3+} are very similar, but the Fe L-edge XA spectra show highly distinctive features for Fe^{2+} and Fe^{3+}. The oxidation state of Fe species was determined as +3 by measuring the XAS at Fe L-edge (**Figure 5.4**b). Fe^{3+} ions can trap the photogenerated electrons, which can reduce O_2 to $\cdot O_2^-$. Meanwhile, Fe^{3+} ion can serve as a mediator to facilitate the oxidation of OH^- and H_2O molecules to ·OH by valence holes. [198] However, it should be noted that excessive doping in polymeric carbon nitride molecules can promote the photogenerated electron-hole recombination and is therefore not favorable for their photocatalytic activities.

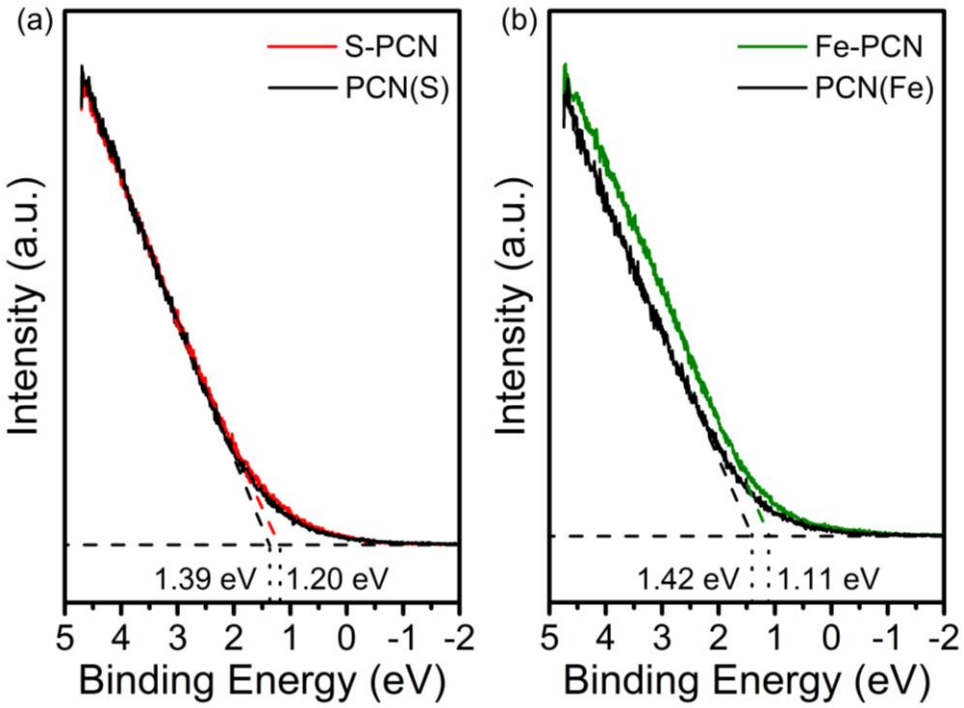

Figure 5.5 High-resolution UPS measurement at valence band of X-PCN and the corresponding reference PCN (X), X = S and Fe. The valence band maximum of each sample was estimated using the intercept on the abscissa obtained by extrapolating the slope of the spectrum to the baseline.

As introduced in Chapter 1, the band edge potential of a semiconductor photocatalyst is of vital importance, which decides the possible pathway of photoredox reactions. Upon the doping, a small red-shift of valence band edge is evident in the UPS measurement (**Figure 5.5**). The valence band maximum, which was originally located at approximately 1.4 eV below the Fermi level, is shifted to 1.20 eV for S doped and 1.11 eV for Fe doped, i.e., the valence band edge is raised. The higher the valence band edge is, the weaker oxidation power the photocatalyst possesses. There is no doubt that the significance of the changes in the valence band position is influenced by the doping concentration. However, in general, the dopant with

a similar ionic radius would adjust the electronic band structure more gently than the dopant that would lead to a local structural distortion. In this study, sulfur has a more similar atomic radius with carbon and nitrogen than iron, which leads to a uniform incorporation in the PCN molecules.

5.3 Electronic Structure Modified by Dopants

The new chemical bonds formed with the dopant incorporation leads to the modification in the electronic structure of PCN materials, which can be characterized by X-ray spectroscopy. First, the unoccupied states are detected by XAS at carbon and nitrogen K-edges. Then the occupied states are measured using resonant inelastic X-ray scattering (RIXS).

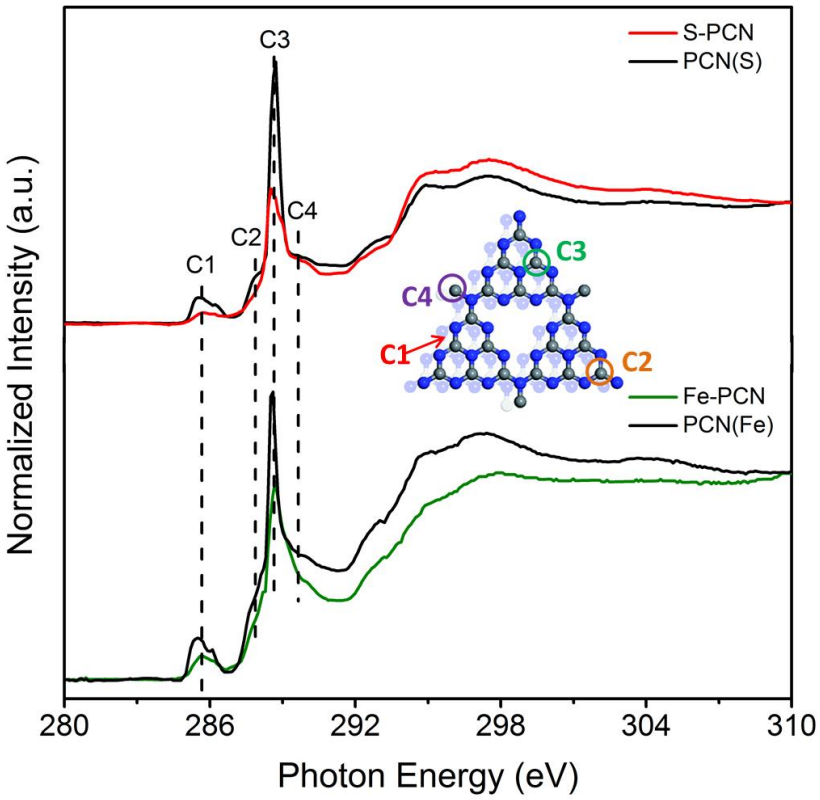

Figure 5.6 C 1 s XA spectra of X-PCN and the corresponding reference PCN (X), X = S and Fe. The insert shows the simplified PCN structural unit indicating all the carbon species as observed in the XA spectra, C1 is targeted to the bonding between two layers.

Figure 5.6 displays the normalized C K-edge XA spectra of doped PCN and reference samples. The introduction of heteroatoms significantly changes the spectral features and line-shapes of PCN. The main features are the transitions from C 1s electron to $\pi^*_{C=C}$ at ~285.6 eV (C1), to $\pi^*_{C-H/C-NH2}$ at ~287.9 eV (C2), to $\pi^*_{N-C=N}$ at ~288.6 eV (C3), and to π^*_{C-N} at ~289.6 eV (C4). The spectra have been normalized to the non-resonant region before and after the main

features, where the intensity is independent with the sample. The feature C1 is characteristic of the interlayered C=C bonding configuration. The feature C2 represents the excitation to the carbon atoms at the edge of the structure. The feature C3 and C4 are the contributions from the carbon at the aromatic tri-*s*-triazine structure, which is the basic structural in PCN materials. In case of sulfur doping, pronounced changes are the decrease in the intensity and the broadening of C3 feature, which indicates the existence of C–S bonds, consistent with the appearance in XPS (**Figure 5.2**). As same as shown in the above XPS results, the XA spectra for PCN(S) and PCN(Fe) also exhibits very similar spectral features. Due to the introduction of iron, the original N=C–N bonds break and new type of C–N is formed. The features C2 and C3 vary upon the change in the tri-*s*-triazine structure. In addition, the oxygen content is significantly increased and oxygen-containing groups are generated as shown in the XPS (**Figure 5.3**). As a result, C2 and C3 features are broadened due to the formation of epoxy group and C=O bond, respectively.

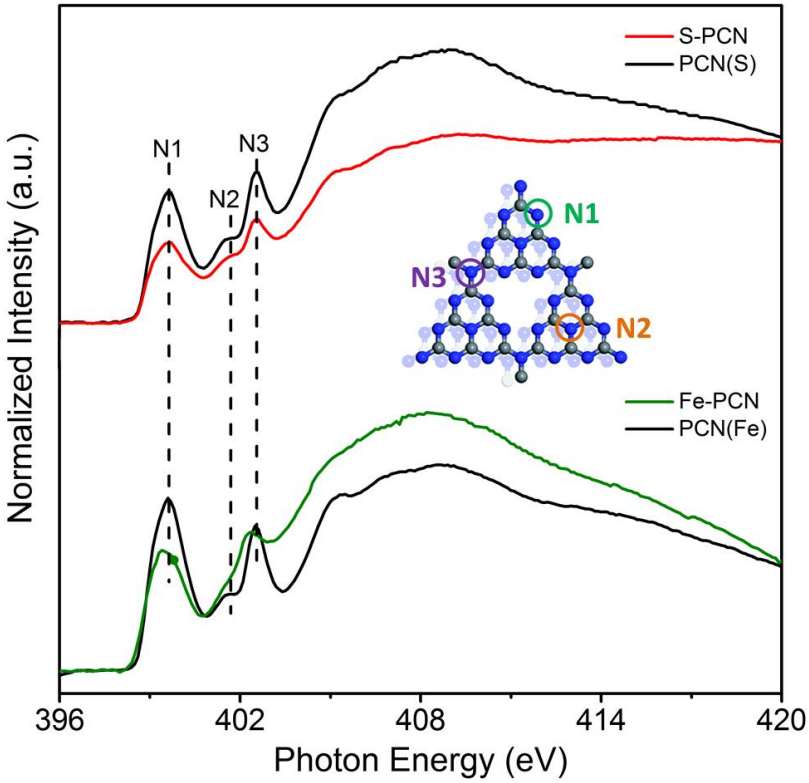

Figure 5.7 N 1s XA spectra of X-PCN and the corresponding reference PCN (X), X = S and Fe. The insert shows the simplified PCN structural unit indicating all the nitrogen species as observed in the XA spectra.

Figure 5.7 shows the normalized N K-edge XAS spectra providing local electronic structures of nitrogen atoms in various PCN samples. There are three features shown in the pre-edge region at 399.6 eV, 401.8 eV and 402.6 eV, which are assigned to the 1s → π*

transition in aromatic nitrogen atoms of heterocyclic rings ($\pi^*_{C=N-C}$, N1), graphitic three-fold nitrogen atoms (π^*_{N-3C}, N2), and sp^3 N–C bridging among tri-*s*-triazine moieties (π^*_{N-C}, N3), respectively. [200,201] Since the sulfur doping is realized by the copolymerization of melamine and trithiocyanuric acid, the nitrogen concentration in S-PCN are lower than that in PCN(S), and leading to the overall decrease in the N K-edge XA spectra. The intensity of the features in Fe-PCN also changes compared with the pristine PCN, the intensity of N1 decreases, whereas those of features in σ* region (above 405 eV) significantly increases. The peaks of three pre-edge features are also shifted to a lower energy. These results are consistent with the C K-edge XA spectra, demonstrating the fractional damage of the tri-*s*-triazine moieties by the incorporation of iron atoms into PCN.

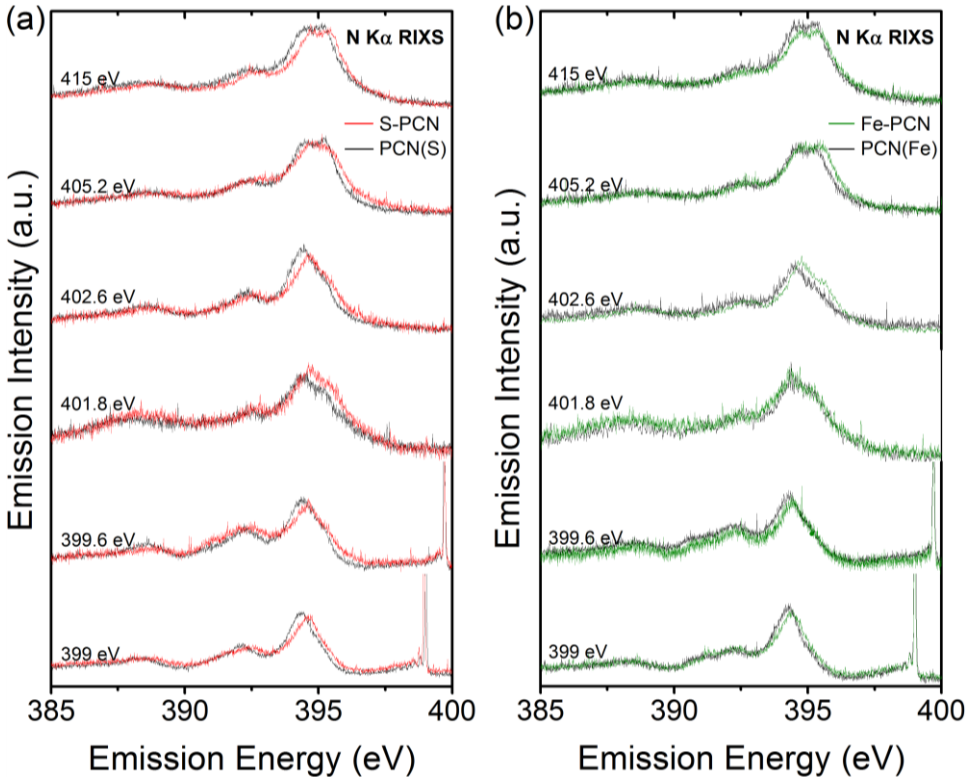

Figure 5.8 N Kα RIXS spectra of X-PCN and the corresponding reference PCN (X), X = S and Fe, with the X-ray excitation energy of 399 eV, 399.6 eV, 401.8 eV, 402.6 eV, 405.2 eV and 415 eV.

To directly verify the change in the localized electronic states in PCN materials upon doping, the density of the states in the occupied states of nitrogen atoms was probed using RIXS. RIXS is powerful in the element-specific investigation of the incident coherent excitation and emission-energy dependence, which is also capable of probing the symmetry points of the Brillouin zone. [163,202,203] **Figure 5.8** shows the N Kα RIXS spectra of the doped and pristine PCN materials, obtained by X-ray excitation at various incident energies. The excitations were selected from the absorption edge in XA spectra. All RIXS spectra were

measured at a constant excitation time and were normalized to the intensity of the inelastic emission peak.

As shown in **Figure 5.8**, there are several common features observed in the N Kα RIXS spectra: a strong emission centered at 394.6 eV, two small features located around 392 and 395.2 eV and a broad feature centered at about 388 eV. The exact position of each feature varies with different sample but is distributed in a narrow range of 0.3 eV. At the same excitation, the dispersive features and their line shapes are very similar in four PCN samples. The incorporation of heteroatoms only leads to the shift in the peak position. The features below 396 eV primarily reflect the effect of core hole on the unoccupied states of nitrogen atoms.

The emission line at 394.5 eV was assigned to the pyridinic N in the previous research [204] on the carbon nitride thin films, and the emission pattern in **Figure 5.8** is very similar to the previous results observed in polypyridine samples. [205] In addition, this emission is the dominating contributor at 399 eV and 399.6 eV excitations, where the N1 nitrogen atom of PCN should be excited. All these discussion supports the assignment of the pyridinic N. Note that the pyridinic N gives multiple peaks in the RIXS spectra, the broad feature below 389 eV is also originated from pyridinic N. [204] As the excitation energy is increased, the emission at 395.2 eV becomes more and more pronounced. This feature can be attributed to the graphitic nitrogen atoms according to the literatures [147,200]. The emission located at 392 eV is identical to the shown in the study on the amino acid film.

There is no extra emission peak shown in the RIXS spectra upon the incorporation of sulfur and iron atoms. For the S-doped PCN sample, the vast majority of sulfur atoms are bonded with carbon, which has little influence on the local structure of nitrogen, and thus induces few changes in the N Kα RIXS spectra. For the Fe-doped PCN sample, the changes in spectral feature are shows in XAS and XPS results, but not detected in RIXS. One possible reason is the difference in the detected signal among the three techniques. RIXS measures photon, whereas XAS and XPS detect electrons. The fluorescence yield is very low for N compared to electron. However, the influence of heteroatoms doping can still be observed in the RIXS spectra, where there is a small shift to the higher energy. This is also shown in the UPS measurements (**Figure 5.5**) with the valence band edge uplift due to the sulfur and iron doping.

Figure 5.9a shows Fe L_3-edge RIXS spectra of Fe-PCN recorded at selected photon energies. At the resonant excitations, 708–713.1 eV, pronounced energy-loss features below the strong elastic peak can be observed. When the incident energy is detuned away from the resonance at 715.4 eV, the Fe RIXS spectrum mainly reflects the characteristics of the Fe 3d

orbitals near the Fermi level, which can be interpreted simply as revealing the density of the occupied states. The occupied states at 707.4 eV can be assigned to Fe–N. [206] In **Figure 5.9**b, RIXS spectra are plotted as a function of the energy loss, where constant energy-loss features are recognized. In addition to the elastic peak, two energy loss features (I and II), attributed to d–d excitations can be observed. [207,208] Peak I is very weak at 708 eV excitation, but can be clearly observed with the other three incident excitation energies. Charge transfer excitation results in a tail located at 5 eV lower the energy loss feature, whose intensity is much weaker than that of d–d excitations.

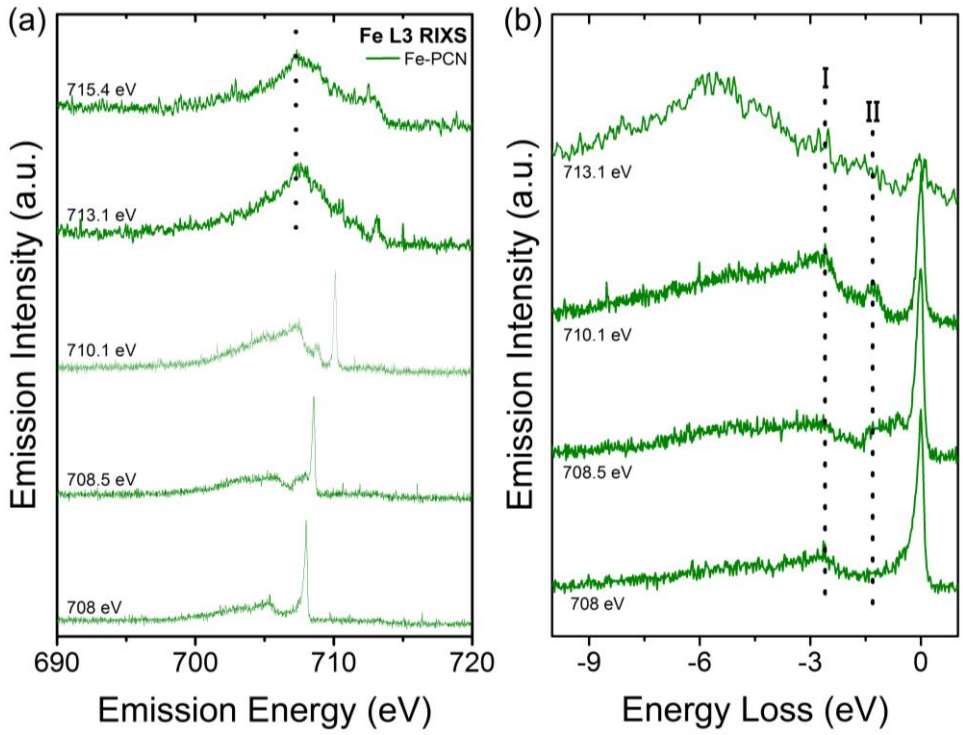

Figure 5.9 Fe L_3 RIXS spectra of Fe-PCN, with the excitation energy of 708 eV, 708.5 eV, 710.1 eV, 713.1 eV and 715.4 eV.

5.4 Vibronic Structure in Carbon Nitride Molecules

Interestingly, as seen in **Figure 5.10**, the excitation into the unoccupied states of nitrogen atoms yields well-separated vibrational excitations next to the elastic line, which can be used to distinguish the vibronic structure. The profile of each vibrational peak is approximately symmetric, and can be therefore fitted to a Gaussian curve. These fitted Gaussians possess a fixed energy width that represents its vibrational energy. The RIXS spectra of S-PCN and PCN(S) (**Figure 5.10**) show a progression of about 0.7 eV with a fundamental frequency of 190 meV. The vibrational progressions shown in the spectra of Fe-PCN and PCN(Fe) are shorter, but the frequencies still remain 190 meV (**Figure 5.10**). Since these vibrational features

were obtained as measuring the N Kα RIXS spectra, it becomes plausible that there is no obvious difference among different PCN samples. It is noteworthy that this is the first time to our knowledge that C-N vibrations are detected by RIXS.

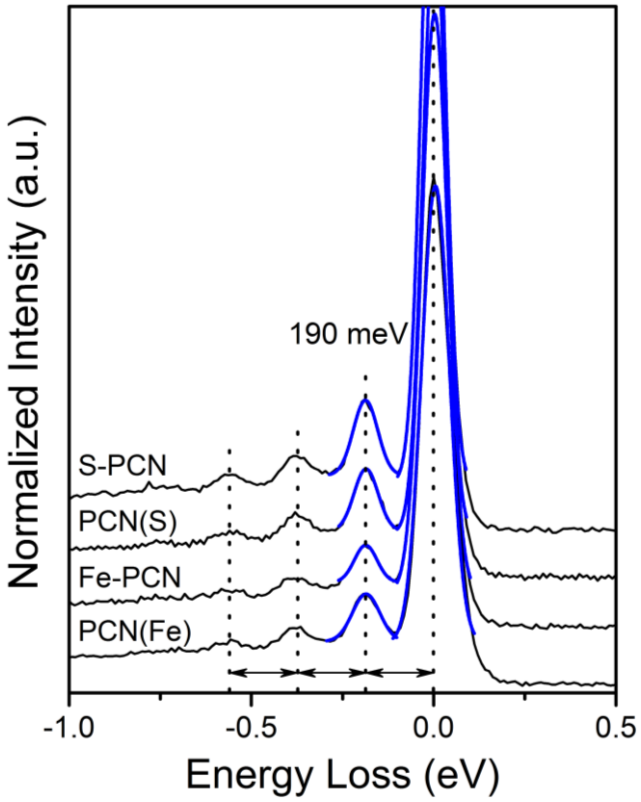

Figure 5.10 Energy loss feature detected from N Kα RIXS experiment. Zero energy loss (*E*=0 eV) is found from elastic line, excitation at the resonance of N1 feature shown in N K-edge XAS.

By tuning the incident photon energy over the resonance, the core electron is excited into the unoccupied states with the distribution of vibrational states. In this state the excited electron remains localized in the resonantly excited unoccupied states with a longer lifetime than that of the core hole (6 fs for the N 1s core level), [110,209] which increases the likelihood of participating in its decay process. During the motion of the excited electron, the potential energy surface of the core-excited state varies and may overlap with ground vibrational levels, which leads to the vibrational progression observed in the RIXS spectrum, as described by Franck–Condon Principle (**Figure 5.11**). [112] In general, the intensity and the number of vibrational progression are decided by the overlap of the vibrational wave function in the ground and excited state. The vibrational progression becomes visible in the spectrum only if the overlap is large enough. And, the larger overlap leads to the more vibrational progressions shown in the RIXS spectra. Using high-resolution RIXS, the vibrational features in the low-energy tail of the elastic line at the pre-edge resonance can be well-isolated resolved, permitting direct comparison to the result obtained from IR or Raman measurement.

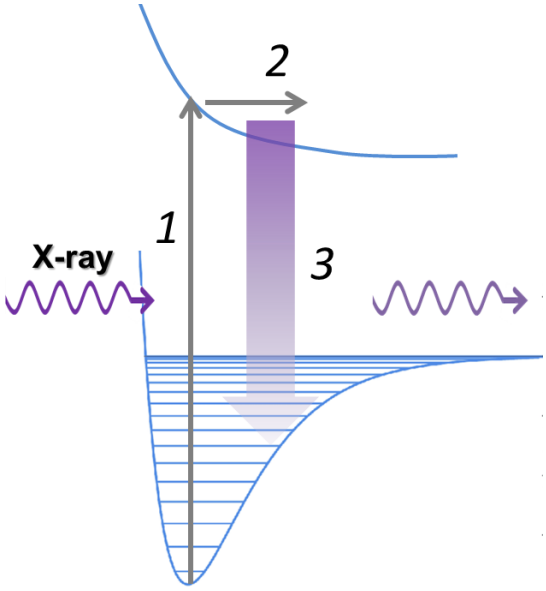

Figure 5.11 Schematic illustration of the vibrational excitation in a RIXS process. 1: excitation of the core electron, 2: motion of the excited electron, 3: decay back to the original electronic ground state.

For PCN materials, the energy separation of the vibrational progressions shown in the N Kα RIXS spectra is 190 meV corresponding to the peak at 1532–1540 cm^{-1} of the vibrational spectroscopy, where PCN is Raman inactive but IR active. [210] **Figure 5.12** shows that there is band at 1538 cm^{-1} in the IR spectrum of PCN(S). Since the RIXS measurement is performed at the resonant excitation of N1 feature (**Figure 5.7**), it is no doubt that the vibronic structure is attributed to the C=N–C structure. Due to the symmetry selection rule for the RIXS process [211,212], other C–N vibrations are not visible by RIXS. IR and Raman remain much easier to access and operate, and possess better spectral resolution than RIXS, however the

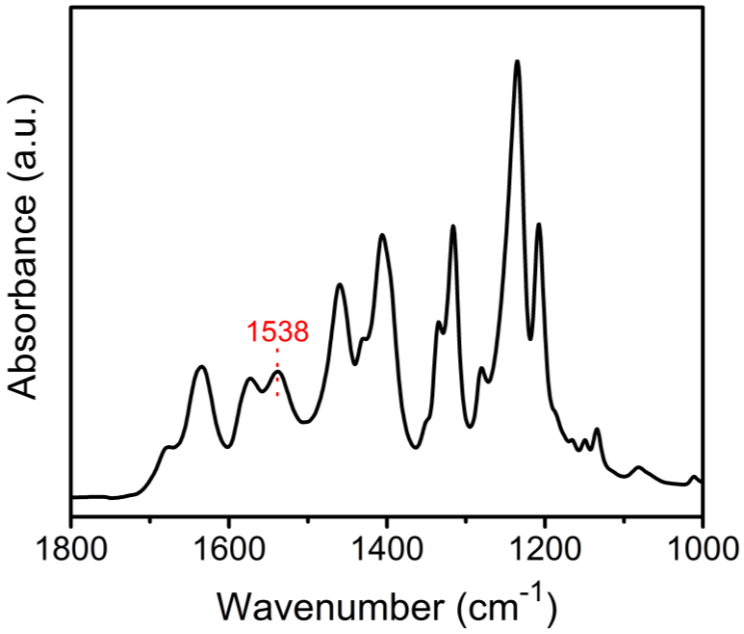

Figure 5.12 ATR-FTIR spectrum of PCN(S).

identification of the molecular vibronic structure is always not easy for such vibrational spectroscopy without element-selectivity and site-selectivity, especially in this case, IR shows many bands in the same region. Furthermore, the spectral resolution of RIXS is improving through the technological development.

5.5 Summary

In this chapter, the influence of two different types of heteroatoms, sulfur and iron on the PCN materials are investigated using various spectroscopic techniques. Despite the small amount of dopants, slight modifications of the electronic structure are detected by combining different spectroscopic techniques. The incorporation of the heteroatoms into PCN molecules were first identified by XPS and UPS. The local structures of unoccupied and occupied states were respectively compared using XAS and RIXS. Furthermore, the vibronic structure in PCN materials was observed using high-resolution RIXS measurement for the first time, to the best of our knowledge. This study suggests that RIXS scheme can also be successfully applied on the solid materials with polymeric nature in advanced studies of vibrational levels of the molecular electronic ground states.

Chapter 6

Highly Efficient Polymeric Carbon Nitride photocatalyst

Content

Large part of this chapter is taken from the published work Meng and Ren et al. [69], edits have been made to match the flow of the dissertation. Scientists from different institutes were involved in the published paper. Meng, Ren, Petit and Zhang designed the experiments. Meng synthesized all samples, performed TEM, SEM and AFM characterizations of the synthesized samples, and evaluated their photocatalytic and photoelectrochemical performance. Ren performed XAS, UPS and IR measurements, analyzed the data, and wrote the manuscript of the journal paper. Liu conducted the surface area and pore analysis. Huang helped with the evaluation of the photocatalytic performance. Petit helped with the XAS experiment in BESSY II and the data analysis. Zhang supervised the project.

6 Highly Efficient Polymeric Carbon Nitride Photocatalyst

In Chapter 5, several types of doped polymeric carbon nitride (PCN) materials have been investigated using various X-ray spectroscopic methods. However, for the practical application, the doping strategy alone is not enough to obtain the optimized PCN photocatalysts. Chemists continue to be interested in trying to develop highly efficient PCN-based materials for photocatalytic H_2 evolution and CO_2 reduction. Here, a bifunctionalized PCN photocatalyst with oxygen doping and amino groups grafting is presented. This photocatalyst is synthesized from a facile two-step continuous thermal treatment and shows a superior efficiency for photocatalytic hydrogen evolution reaction (HER). To understand the origin of the high activity, the comprehensive spectroscopic analysis is feasible and reliable, as shown previously in this dissertation. This chapter proposes an example for studying the structure–performance relationship of a state-of-the-art PCN photocatalyst.

6.1 Motivation

In addition to the electronic structure modulation using co-polymerization and heteroatom doping strategy that is showed in Chapter 5, the structure modification of PCN is another method to optimize its photocatalytic performance. The nanostructure engineering of PCN, including the surface functionalization, morphology and crystallinity changes, can increase the solvent accessible surface area, improve the hydrophilicity and facilitate charge transfer. [64]

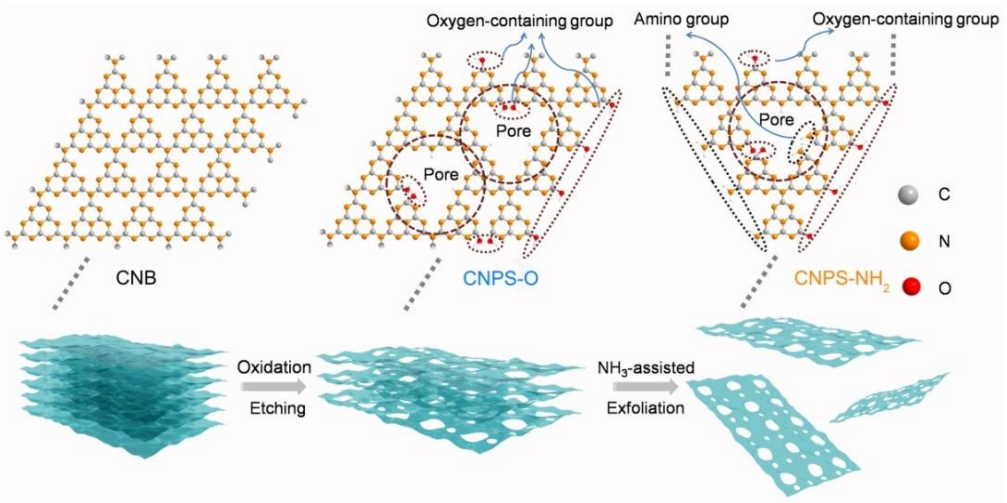

Figure 6.1 Schematic illustration of the preparation process of CNPS-NH_2. Reproduced from ref. [68] with permission from the Royal Society of Chemistry.

The group led by Prof. Bin Zhang in Tianjin University developed a continuous thermal treatment process to prepare modified PCN nanosheets **(Figure 6.1)**, which involves the thermal treatment of bulk PCN in air and the subsequent exfoliation under NH_3 atmosphere (see the Appendix for details). [69] The calcination in air can oxidize the pristine

PCN, leading to the introduction of oxygen into the PCN frameworks. Meanwhile, a porous structure can be formed by the thermal oxidation-etching. [213] Furthermore, the thermal treatment in NH_3 atmosphere has been demonstrated to be an effective way to weaken the interlayer bonding and exfoliate PCN bulk materials. [214]

Figure 6.2 is the photograph of three samples. The bulk PCN (CNB) is synthesized by the thermal-polymerization of melamine, and the other two samples, CNPS-O and CNPS-NH_2, are the products obtained from the different stages of the two-step thermal treatment process. As can be seen from the **Figure 6.2**, three samples of the same quality (80 mg) have different volumes. CNPS-NH_2 sample is looser and lighter, indicating it has a larger surface area. From the surface area analysis and microscopic characterization, it has confirmed that the CNPS-NH_2 possesses a unique ultrathin morphology and rich pores. [69] Another obvious difference of the three samples is their colors (**Figure 6.2**). The yellow CNB powder converts to yellowish-white sample after the thermal treatment, which might be attributed to quantum confinement effect in the (nano)domains of the ultrathin CNPS-NH_2 nanosheets. [215]

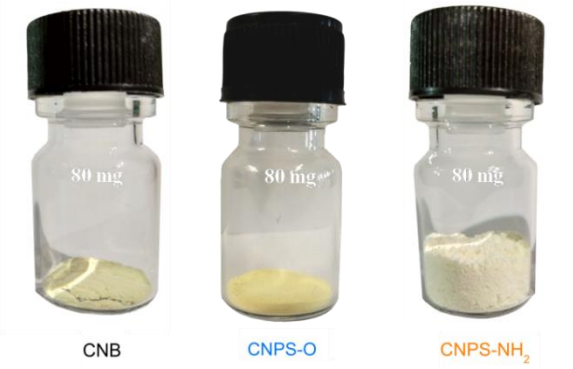

Figure 6.2 The photographs of CNB, CNPS-O and CNPS-NH_2. Reproduced from ref. [69] with permission from the Royal Society of Chemistry.

Normally, the white color of a photocatalyst is a reflection of the large bandgap between its occupied valence band and empty conduction band and the fact that less visible light can be absorbed than that with yellow color. However, the pale-colored CNPS-NH_2 exhibits a much higher performance in photocatalytic reaction than the other two samples. It is impressive that the H_2 evolution rate of CNPS-NH_2 is up to 20.9 mmol h^{-1} g^{-1} under simulated sunlight (AM 1.5 G) irradiation using Pt as a cocatalyst, which is one of the most robust PCN/Pt systems. [69] To understand this unusual performance, spectroscopic investigations are needed.

It should be pointed out that some results obtained from the collaborators in Tianjin University, namely, the UV-Visible absorption spectra and the contact angle measurement, are also introduced here for clarity and for discussion with our experiments.

6.2 Bifunctionalized Polymeric Carbon Nitride Nanosheets

The optical absorption properties of the samples were first studied by UV–Vis absorption spectra (**Figure 6.3**a). The light absorption edge of the CNPS-O is red-shifted relative to that of CNB, mainly owning to the presence of oxygen-containing group. [216] The blue-shift in the absorption edge of CNPS-NH_2, compatible with its white color. From Kubelka-Munk function versus the energy of exciting wavelength derived from UV–Vis spectra, [44,217] the band gaps of these samples are calculated to be 2.75, 2.70, and 2.96 eV for CNB, CNPS-O, and CNPS-NH_2, respectively (**Figure 6.3**b). The result is in agreement with the variation of the steady state photoluminescence emission peak. [69]

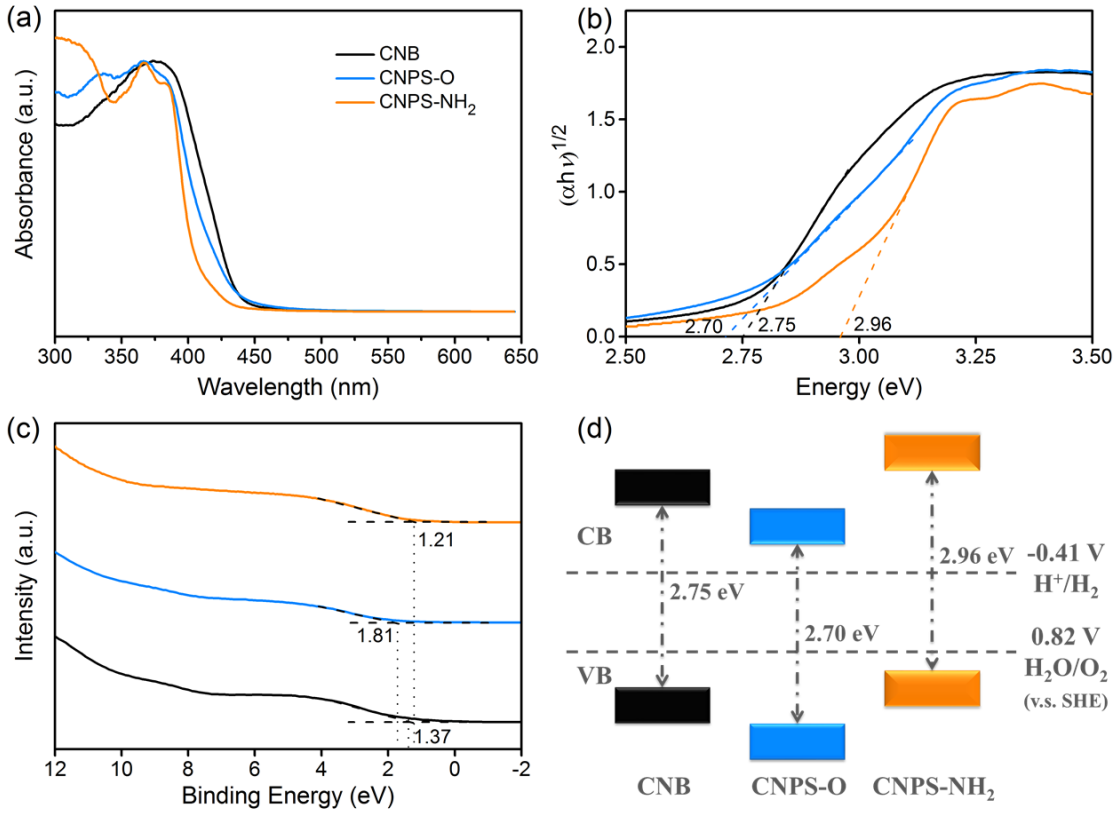

Figure 6.3 (a) UV-Visible absorption spectra, (b) The plot of the transformed Kubelka–Munk function versus the gap energy, (c) UPS spectra and (d) Schematic band structures of CNB (black), CNPS-O (azure) and CNPS-NH_2 (orange). Reproduced from ref. [69] with permission from the Royal Society of Chemistry.

As previously mentioned in this dissertation, the position of valence band edge can be measured from UPS. **Figure 6.3**c shows the UPS results of the three samples. They have quite similar electron density distributions in the vicinity of the Fermi level, but different positions for the valence band edge, 1.37 eV for CNB, 1.81 eV for CNPS-O and 1.21 eV for CNPS-NH_2. As a result, the positions of the band edge of the three PCN samples can be consequently

deduced (**Figure 6.3**d). [44,218] For all three samples, the thermodynamic requirement is satisfied for both hydrogen and oxygen evolution. It should be noted that the potential of conduction-band edge of CNPS-NH_2 is much higher than those of other sample, which can provide a greater driving force for the H_2 evolution reaction.

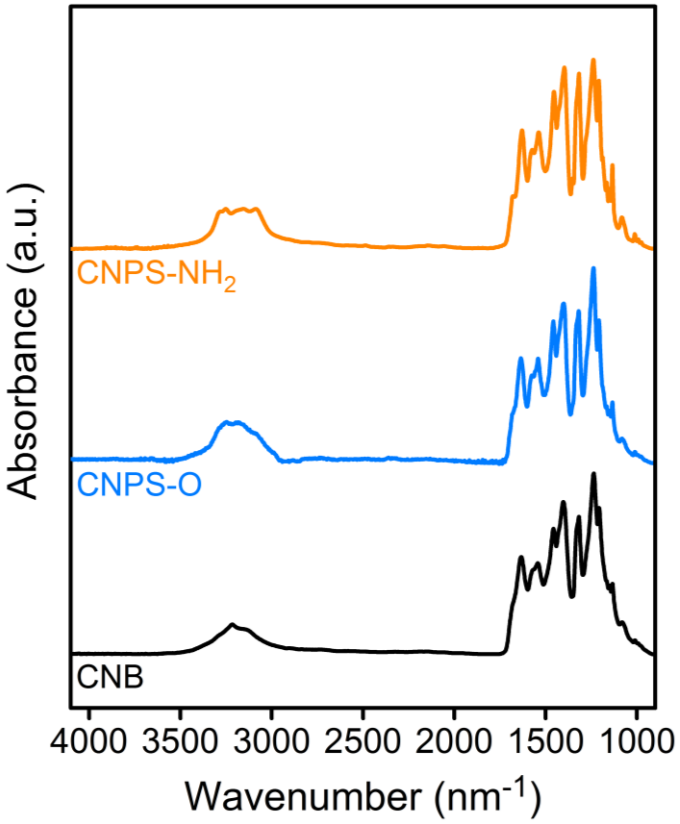

Figure 6.4 ATR-FTIR spectra of CNB (black), CNPS-O (azure) and CNPS-NH_2 (orange). Reproduced from ref. [69] with permission from the Royal Society of Chemistry.

The difference in the chemical composition for three PCN samples can be characterized by the attenuated total reflectance Fourier transform infrared spectra (ATR-FTIR). **Figure 6.4** presents the typical infrared absorption bands in the as-prepared PCN samples. The increased intensity of the C–O stretching at 1062 and 1134 cm^{-1} from CNB to CNPS-NH_2 indicates the richer oxygen-containing groups in CNPS-NH_2. The peaks between 1200 and 1700 cm^{-1} are mostly from the stretching and bending modes of heptazine heterocyclic ring, and the broad feature at 3000–3350 cm^{-1} is assigned to stretching modes of amine group, alcohol hydroxyl group and sp/sp^2 C–H. [219] There are distinct shapes for the amine group, which is in agreement with the bending mode in the range of 1550–1640 cm^{-1}. Primary amino groups with two N–H stretch absorptions (3252 and 3285 cm^{-1}) are observed in CNPS-NH_2, while the two other samples mostly present secondary amino groups (only one peak around 3250 cm^{-1}). [220] The distinct change of Zeta potential from –14.0 to +19.1 mV

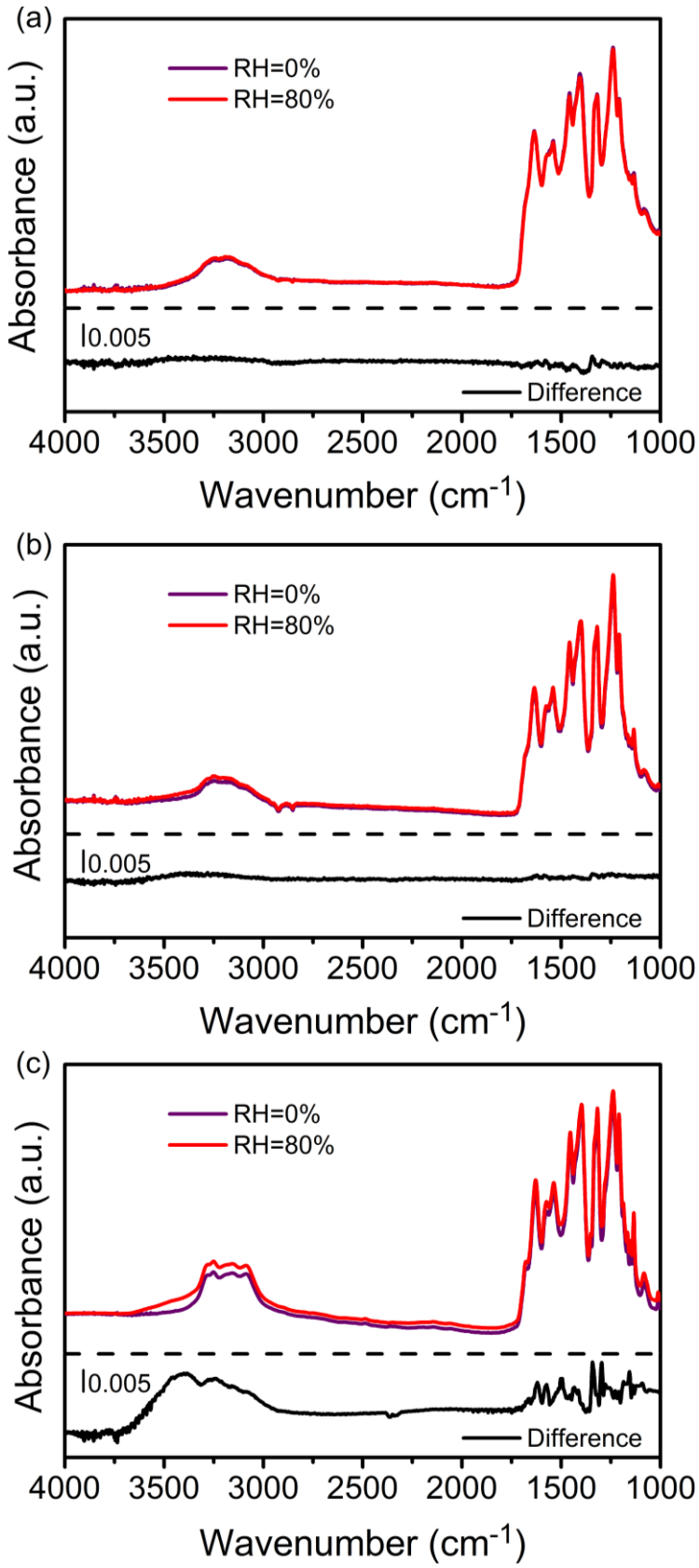

Figure 6.5 FTIR spectra of three samples recorded from dry state (RH=0%, purple) and that from humid atmosphere (RH=80%, red), (a) CNB, (b) CNPS-O and (c) CNPS-NH_2; the lower panel shows the corresponding difference spectrum. Reproduced from ref. [69] with permission from the Royal Society of Chemistry.

before and after NH_3 thermal treatment of CNPS-O further proves the introduction of primary amino groups. [69] These results suggest that not only the ultrathin structure but primary amino groups (–NH_2) also formed during the NH_3-assisted exfoliation treatment. The earlier reports confirms that –NH_2 groups can act as hole-stabilizers and thus prolong the lifetime of the excited states in photocatalysts. [221,222] In addition,–NH_2 group possesses a strong Lewis basicity, which is also favorable for the photoreduction of water to hydrogen.

Both oxygen containing groups and amino groups have favorable interaction with water molecules, therefore the bifunctionalized sample, CNPS-NH_2, is supposed to have an enhanced hydrophilicity. After measuring the infrared spectra in dry states, the equipped environmental cell of infrared spectrometer endows the *in-situ* surface chemistry investigations on three PCN samples. **Figure 6.5** shows the ATR-FTIR spectra measured on each sample at different relative humidities (RH). As expected, the changes of infrared signature induced by water absorption can be clearly observed in CNPS-NH_2 sample. The *in-situ* IR results demonstrate that the hydrophilicity of the samples can be stepwise improved by the successive two-step thermal treatment. In addition, the same conclusion can be reached from the contact angle measurement. The water contact angles of CNB, CNPS-O and CNPS-NH_2 are 55.61°, 40.90° and 28.45°, respectively (**Figure 6.6**). The smaller the contact angle is, the wetting tendency is larger. [223] The improved hydrophilicity and increased solvent accessible surface area are beneficial to the hydrogen evolution reaction over CNPS-NH_2 sample.

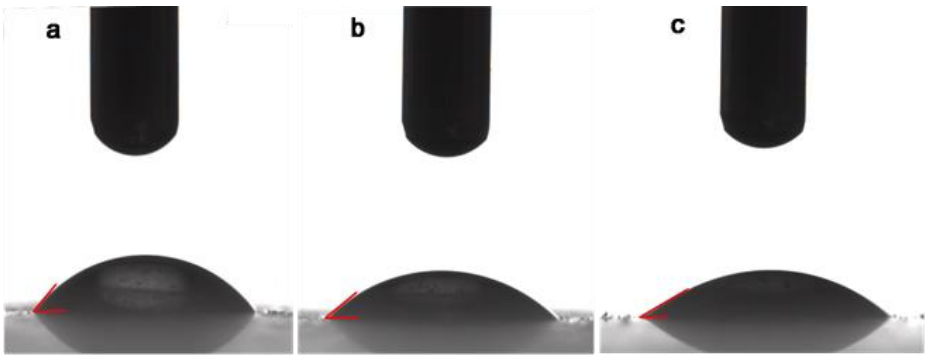

Figure 6.6 The contact angle measurements of (a) CNB, (b) CNPS-O and (c) CNPS-NH_2. Reproduced from ref. [69] with permission from the Royal Society of Chemistry.

6.3 Influence of Chemical Bonding Configuration on Photocatalysis

Despite an increase in defects sites and functional groups, the atomic structure of the PCN semiconductor has to remain stable for efficient photocatalytic activity. To further investigate the local electronic configuration and chemical structure of PCN-based photocatalysts, X-ray absorption spectroscopy (XAS) and X-ray photoelectron spectroscopy (XPS) were adopted.

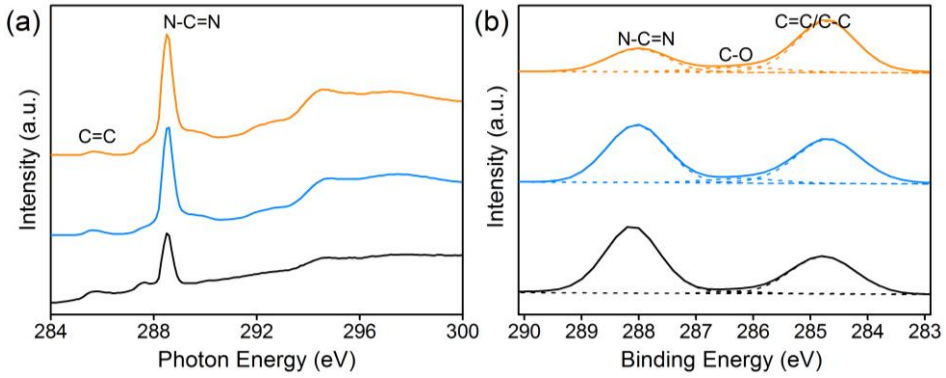

Figure 6.7 (a) C K-edge XAS and (b) C 1s high-resolution XPS spectra of CNB (black), CNPS-O (azure) and CNPS-NH_2 (orange). Reproduced from ref. [69] with permission from the Royal Society of Chemistry.

The C K-edge XAS spectra of these samples are presented in **Figure 6.7**a. XAS probes unoccupied electronic states, and is particularly sensitive to the local electronic configuration. The C K-edge XAS spectra consist of contributions from transitions from 1s to π* at 285.7, 287.5, 288.6, 289.9 eV and σ* at 293–298 eV, which are similar to the spectra shown in Chapter 5. The π* feature at 285.7 eV is typical of the out-of-plane C=C bond, related to interlayer bonding. [224] The intensity of this feature decreases from CNB to CNPS-NH_2 because the delocalized π bonds existing in the interlayer of the stacked CNB are weakened after the sequence of calcination treatments. Together with the decrease of a percentage of the feature at 288.6 eV that originate from the aromatic carbon atoms in the ring (N–C=N), it confirms that CNB has been exfoliated and converted to ultrathin sheets, as determined by the above-mentioned results. This phenomenon can be more clearly seen from the C 1s XPS spectra (**Figure 6.7**b). Moreover, the enhancement of the features at 287.5 and 289.9 eV in the C K-edge XAS spectrum, which are attributed to the carbon species in different carbon–oxygen functional groups, [151] appears after the thermal treatment in air.

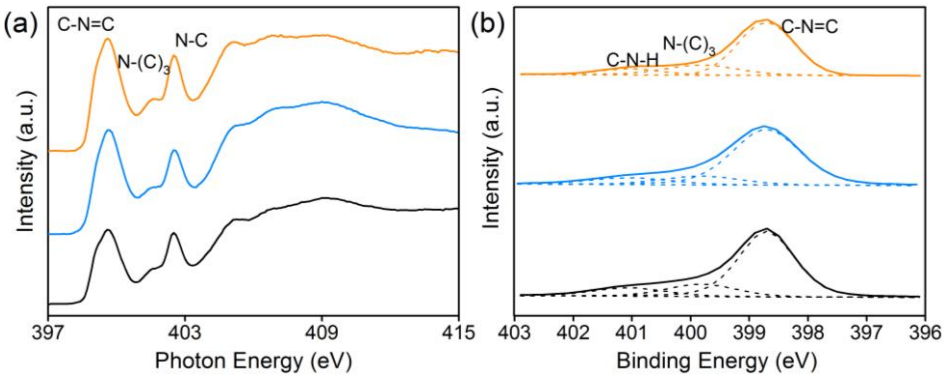

Figure 6.8 (a) N K-edge XAS and (b) N 1s high-resolution XPS spectra of CNB (black), CNPS-O (azure) and CNPS-NH_2 (orange). Reproduced from ref. [69] with permission from the Royal Society of Chemistry.

At the nitrogen K-edge XA spectra (**Figure 6.8**a), four main characteristic resonances are observed at 399.6, 401.7, 402.5, and 404–412 eV. The first three features are respectively correspond to the 1s → π* transition in the pyridinic nitrogen atoms of heterocyclic rings ($\pi^*_{C=N-C}$), graphitic three-fold nitrogen atoms (π^*_{N-3C}) and the bridge nitrogen atoms among tri-*s*-triazine moieties (π^*_{N-C}), as discussed in the previous chapter. The broad features in the range of 404–412 eV are originated from the 1s → σ^*_{N-C} transition. [225] The large similarities among three PCN samples imply that the electronic structure surrounding the nitrogen atom are only little influenced by the changes in the surface chemistry. In other words, this nicely demonstrates the local probing character of XAS. The spectral characters of the tri-*s*-triazine moieties shown at both C K-edge and N K-edge, together with the N 1s XPS (**Figure 6.8**b), reveal the preservation of the tri-*s*-triazine structures in CNPS-NH_2. This microstructural integrity is favorable for channeling photogenerated charge transfer in CNPS-NH_2 to participate in the photocatalysis process.

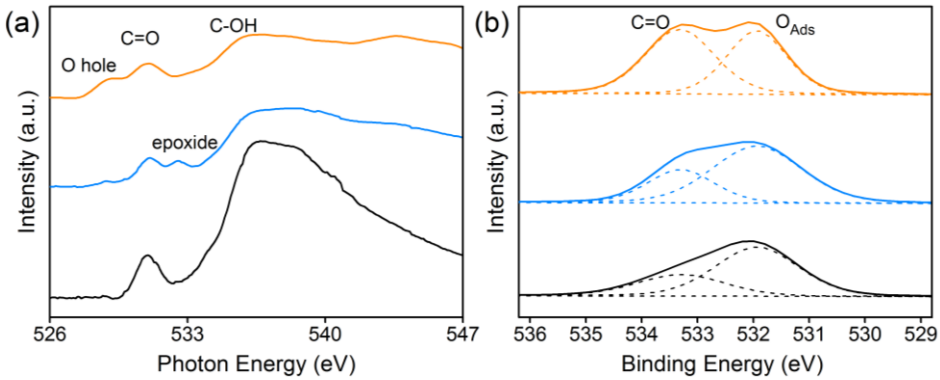

Figure 6.9 (a) O K-edge XA spectra and (b) O 1s high-resolution XPS spectra of CNB (black), CNPS-O (azure) and CNPS-NH_2 (orange). Reproduced from ref. [69] with permission from the Royal Society of Chemistry.

The O K-edge XAS and O 1s XPS spectra (**Figure 6.9**) further reveal the changes of surface chemistry during successive thermal treatments. Significantly, new features appear in the pre-edge region of O K-edge XAS for CNPS-O and CNPS-NH_2. The feature at 533.6 eV on CNPS-O is assigned to the 1s → π* transition in epoxide structure, [145] which is weakened after the treatment in NH_3 atmosphere, probably due to the replacement of related oxygen atoms by nitrogen atoms. The feature at around 529 eV could refer to the electronic transition from O 1s to O 2p holes. [226] During the successive thermal treatments, the characters around 536 and 538 eV for 1s → σ^*_{C-O-H} transition and 1s → σ^*_{O-C} gradually disappear from CNB to CNPS-NH_2. [227] In addition, some bonds involving oxygen atoms are broken due to defect formation, thus leading to the appearance of O 2p holes. In fact, if photogenerated charge carriers are efficiently trapped at these defective sites, the probability that they react with

adsorbed species largely increases, with a parallel decrease of the undesired electron–hole recombination, which have been confirmed by the photoelectrochemical measurement and time-resolved photoluminescence spectra. These results reveal that the mobility of the photo-generated charge carriers is promoted in CNPS-NH_2, and thus a better photocatalytic performance can be anticipated.

6.4 Summary

In this chapter, a structure–performance relationship of highly efficient PCN photocatalysts have been comprehensively investigated using various spectroscopic methods. First, combining UV–Vis spectroscopy and UPS, the band edges position of PCN samples were estimated, which confirmed the feasibility and favorability for photocatalytic hydrogen evolution reaction over CNPS-NH_2 from the thermodynamic aspect. Then the ATR-FTIR results showed the Lewis basic –NH_2 groups were generated with the thermal treatment in NH_3 atmosphere. Finally, the preservation of the tri-*s*-triazine moieties and the formation of oxygen holes were detected by X-ray spectroscopies, which played an essential role in charge transfer and separation. These findings suggest that the nanostructuring of PCN materials with oxygen doping, surface functionalization and exfoliation endow the PCN nanosheets with atomically-thin structure, hydrophilic surfaces, strong Lewis basic sites, and long lifetime of charge carrier, the efficient charge utilization can be significantly improved from respects of its generation, diffusion and reaction, and thus synergistically leading to highly efficient H_2 evolution. Additionally, this research highlights the contribution of various spectroscopic techniques to the characterization of PCN-based photocatalytic materials.

Chapter 7

Conclusions and Perspectives

This dissertation has been an effort to advance the fundamental knowledge about carbon nanomaterials for energy applications. Carbon dots and polymeric carbon nitride represent two typical carbon nanomaterials for artificial photosynthesis. A unique approach coupling various spectroscopic techniques, including synchrotron soft X-ray spectroscopies, infrared spectroscopy and photoelectron spectroscopy has been successfully applied to provide detailed information about the electronic and chemical structures behind their photocatalytic performance. From the results presented in this dissertation, it is becoming increasingly clear that research on carbon nanomaterials requires not only rational design but also accurate characterization.

7.1 Conclusions

In the beginning, many literatures were reviewed in **Chapter 1** to find out the current development of novel photocatalysts based on carbon nanomaterials and also the obstacle which limits their performance in artificial photosynthesis. Advanced characterization techniques were then introduced in **Chapter 2** from both the fundamental and experimental perspectives. Finally, studies on different carbon nanomaterials were then presented.

Carbon dots (CDs) possess abundant surface active centers and adjustable core structures which can be effectively tuned by modulating elemental compositions and surface functionalities. This modification-flexibility endows CDs versatile applications, such as fluorescence bioimaging and energy harvesting. However, as a young member in the family of carbon nanomaterials, some fundamental knowledge of CDs is still missing. The electronic structures of CDs, the hydrogen bonding network of CDs aqueous dispersion and the charge transfer properties between CDs and solvent molecules remain poorly investigated.

In **Chapter 3**, the role of the surface chemistry played on CDs' optical, chemical and electronic properties was investigated on three different CDs samples functionalized with carboxyl, amino and hydroxyl groups. The first experimental result on electronic structure of CDs studied by synchrotron-based XA and XE spectroscopies is shown. It suggested that

CDs have an electronic signature which differ significantly from that of previously investigated carbon nanomaterials (graphene, nanodiamonds…) due to the presence of a strong C=O bonds signature. Surface-dependent hydrogen bonding between CDs surface and water molecules was also demonstrated using *in-situ* FTIR spectroscopy measurements on CDs for the first time, and particularly showed that the hydrogen bonding interaction between water molecules and C=O bond varied in different chemical environment. Based on the X-ray and infrared spectroscopic results, the impact of the C=O bonds environment on the blue luminescence was further discussed. It demonstrated that that for CDs, the stronger hydrogen bond is formed with water, the narrower emission energy level is generated.

In **Chapter 4**, the charge transfer between CDs photosensitizer and water was characterized by *in-situ* ionic yield XAS for the first time. Due to the progress made in the previous chapter, the features shown in the XA spectra can be interpreted. By comparing with transmission XAS in liquid and electron yield XAS measured in vacuum, it was demonstrated that ionic yield XAS could identify chemical sites inducing charge transfer in solution. The dependence of the core properties of CDs on the charge transfer was also observed among the CDs with amorphous, graphitic and nitrogen-doped graphitic cores. The excitation of C=C bonds in CDs with graphitic core was found to be beneficial for the charge transfer to water, which is not the case for amorphous CDs. This result is in full agreement with the photocatalytic activity of these CDs previously reported. Additionally, extended hydration shells around CDs were evidenced by the strong changes of the transmission XA spectra of CDs dispersions at oxygen K edge.

In parallel, polymeric carbon nitride (PCN) was also shown to be a promising metal-free photocatalyst with visible-light activity. Much effort on the novel synthetic methods and modification techniques of PCN materials have been devoted by chemists and material scientists since its discovery in 2009, yet few studies focus on how its chemical composition influences on the electronic structure. In addition, many emerging photocatalytic applications of PCN materials rely on the accessible surface functionalization.

In **Chapter 5**, the influence of heteroatoms incorporation in PCN materials was studied. Two types of doped PCN materials with sulfur and iron were compared. The C–S and Fe–N bonds were identified as the doping species in two doped materials by XPS. The negative shifts of the valence band potential upon doping were observed by UPS and RIXS. The slight modifications of the unoccupied states due to the small amount of dopants were detected by XAS. Furthermore, the first observation of the vibronic structure in PCN materials was realized using high-resolution RIXS measurement. It suggests that RIXS

scheme can be successfully applied on the solid materials with polymeric nature in advanced studies of vibrational levels of the molecular electronic ground states, which makes the RIXS technique an efficacious complementary method to IR and Raman spectroscopies in studies of molecular vibrations.

In **Chapter 6**, various spectroscopic techniques were applied to reveal how the changes on chemical and electronic structure of PCN materials affect its photocatalytic performance. The superior activity was reported on the modified PCN materials successively treated by oxidation etching in air and exfoliating in NH_3 atmosphere. The generation of strong Lewis basic $–NH_2$ groups during the thermal treatment was demonstrated by ATR-FTIR. The enhanced hydrophilicity from surface oxygen groups was also observed in the *in-situ* FTIR measurement. The preservation of the tri-*s*-triazine moieties and the formation of oxygen holes were detected by X-ray spectroscopies, which plays an essential role in charge transfer and separation. Moreover, the conduction-band edge was found to be more negative after the thermal treatment by combining UV–Vis spectroscopy and UPS.

7.2 Perspectives

The main goals set out for this dissertation has been achieved, gaining new knowledge for the carbon nanomaterials towards artificial photosynthesis. With these progresses presented above, the studies presented in this dissertation could also be considered as providing a basis for future research, and therefore inspires some possible follow-up experiments that could be conducted in order to enrich our understanding on carbon nanomaterials and improve their performance in corresponding application.

Combination with other novel spectroscopic techniques can be useful in providing a complete picture of carbon nanomaterials. One example is the study of electron transfer in carbon nanomaterials using time-resolved spectroscopy. Most applications of carbon nanomaterials stem from their unique electron property and are realized upon the charge transfer in the materials. Therefore, the studies on the electronic structure and the charge transfer process are of importance. In this dissertation the efforts we devoted by using X-ray spectroscopy were shown. The investigation using time-resolved spectroscopy in carbon nanomaterials can however provide information on dynamic phenomena. Time-resolved spectroscopic technique for charge-transfer investigation includes, but is not limit to, transient-absorption spectroscopy, time-resolved fluorescence spectroscopy, time-resolved photoemission spectroscopy and time-resolved X-ray absorption spectroscopy. In addition, the development of ultrafast laser technology would facilitate the research of time-resolved

spectroscopic technique. The recent progress of femtosecond spectroscopy make it possible to probe all elementary reactions occurring in the photocatalytic process, which includes charge generation at 10^{-15} seconds, charge separation at 10^{-12}–10^{-8} seconds, recombination at 10^{-7}–10^{-5} seconds, and the interfacial reactions at 10^{-3}–1 seconds.

***In-situ* and *operando* characterization** are paramount to provide a precise picture of carbon nanomaterials. Despite there is significance of their existence of *ex-situ* spectroscopic techniques, the developments of *in-situ* and *operando* characterizations lead the future direction and advance our comprehension of carbon nanomaterials in energy applications. As shown in this dissertation, CDs have already been studied by *in-situ* FTIR and XAS. The charge transfer at the interface between CDs and water has also been investigated using *in-situ* XAS. However, in a real photocatalytic process, CDs, the photosensitizer, are always incorporated with a photocatalyst to realize the reaction. Although the photosensitizer and photocatalyst can be studied independently, it is their interplay, in a realistic photocatalytic reaction, that decides the overall performance. It should be emphasized that, sometime the possibilities for *operando* characterizations, especially in the presence of gases or solvents, are limited by the operational constraints which require the development of new experimental approaches.

Appendix

This part presented here helps clarify the research shown in the previous chapters. The common infrared absorption frequencies in carbon nanomaterials shown in Appendix I are summarized based on my experimental findings and the published literatures. The spectra and table shown in Appendix II and V are obtained from my experiments. The descriptions on the experimental setup in Appendix III are quoted from the various sources [98, 228–232]. And the details on the sample preparation in Appendix IV are provided by the collaborators.

Appendix I Infrared Spectroscopy Absorption Table

Table A1 Summary of common infrared absorption frequencies in carbon nanomaterials.

Functional groups	Frequency (cm^{-1})
O–H stretch, free water	3600–3650
N–H stretch	3100–3500
O–H stretch, alcohols, phenols	3200–3640
O–H stretch, carboxylic acid	2400–3560
C–H stretch, aromatics	3050–3150
C–H stretch, alkanes	2850–3000
C–H stretch, anhydrides	2800–2900
C=O stretch, aldehydes	1720–1740
C=O stretch, ketones	1705–1725
C=O stretch, carboxylic acids	1700–1725
C=O stretch, conjugated	1680–1690
C=O stretch, amides	1640–1670
N–H bend, amides	1550–1650
C=N stretch	1570–1700
C=C stretch, aromatics	1450–1650
$–CH_2–$ bend	1465
$–CH_3$ bend	1375, 1450
C–N stretch, 1 amides	1400–1420
C–N stretch, 2 amides	1200–1350
C–O–H bend (in-plane)	1390–1440
O–H bend (in-plane)	1310–1430
C–OH stretch, 3 alcohos	1150–1220
C–OH stretch, 2 alcohos	1090–1120
C–OH stretch, 1 alcohos	1040–1060
C–O stretch, carboxylic acids, ethers	1100–1300

Appendix II Background at Carbon K-edge

The carbon contamination of optics in the beamline results in a strong background appearing in the raw XA spectrum collected at carbon K-edge. This background can be corrected using the TEY-XA spectra at the C K-edge measured from the beamline (**Figure A1**). Since the photocurrent measured from the carbon contamination at the beamline is usually higher than that measured from the sample, all TEY-XA spectra from the sample are first scaled to the first peak appearing at 280.2 eV. The background measured from the beamline is subsequently subtracted from the scaled spectrum of the sample in order to remove any contribution from the carbon contamination of the beamline.

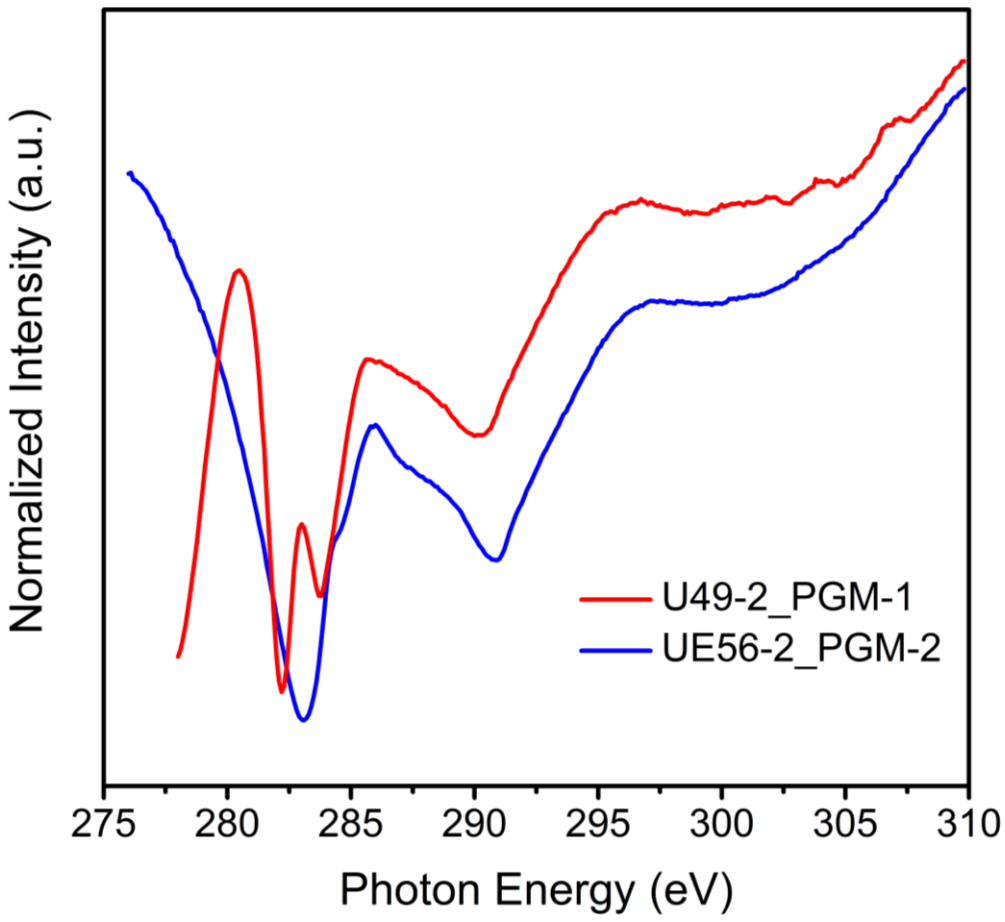

Figure A1 TEY-XA spectrum at C K-edge measured from the GaAs photodiode, representing the carbon contamination of optics in the beamline.

Appendix III Beamlines and Experimental Stations

The U49-2_PGM-1 Beamline at BESSY II is connected to the U49-2 undulator and equipped with a plane grating monochromator (PGM) that offers high-flux soft X-ray photons with the energy range from 85 to 1600 eV. In this dissertation, LiXEdrom end station was adopted. The TEY-XAS results presented in Chapter 3, 4 and 6, and the XES results in Chapter 3 were collected at this beamline. [228]

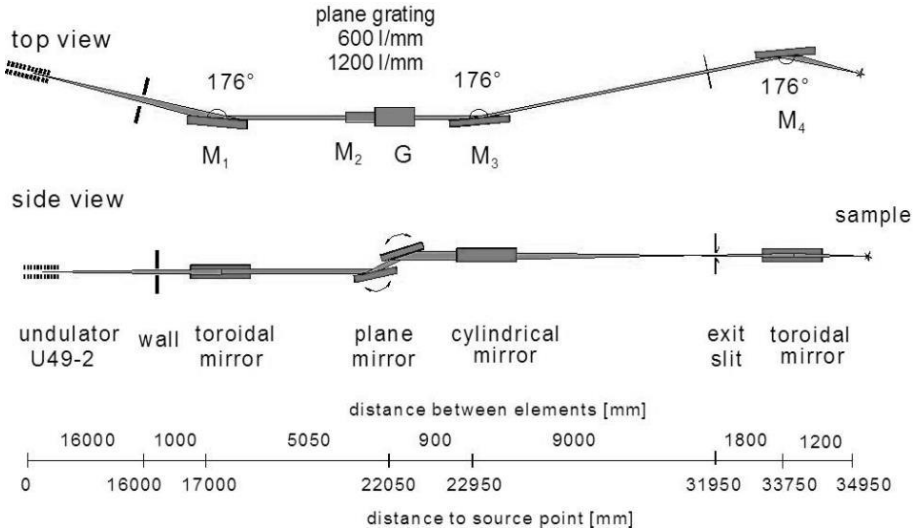

Figure A2 Optical layout of U49-2_PGM-1 beamline at BESSY II synchrotron facility. Downloaded from [228].

The UE56-2_PGM-2 Beamline at BESSY II is one of two PGM beamlines situated at the double undulator UE56-2, which provides soft X-ray with the photon energy ranging from 60 to 1300 eV. The XAS and XES data of doped PCN samples shown in Chapter 5 were collected at this beamline using LiXEdrom station. [98]

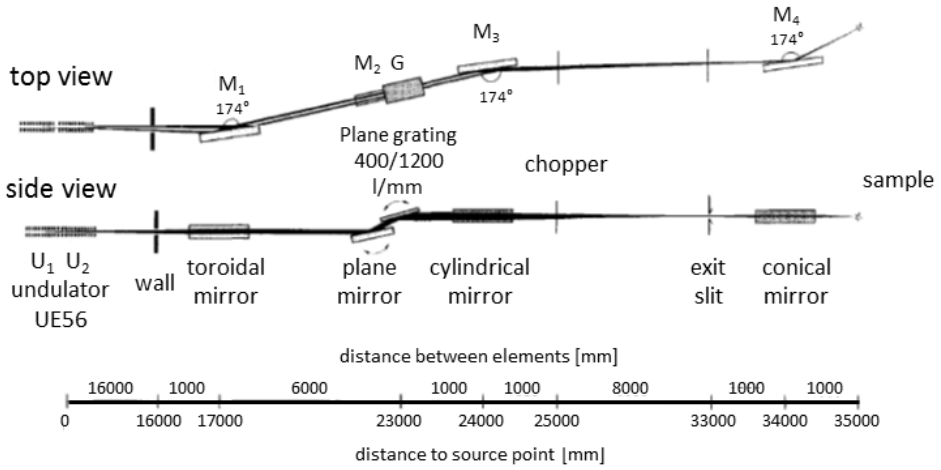

Figure A3 Optical layout of UE56-2_PGM-2 beamline at BESSY II synchrotron facility. Reproduced from [98] with permission from Elsevier.

The U41-PEAXIS beamline at BESSY II is a newly-built beamline specifically for the fixed end station PEAXIS, which provides high-flux soft X-ray photons in the energy range between 180 and 1600 eV. The RIXS spectra of doped PCN samples shown in Chapter 5 were measured at this beamline. [229]

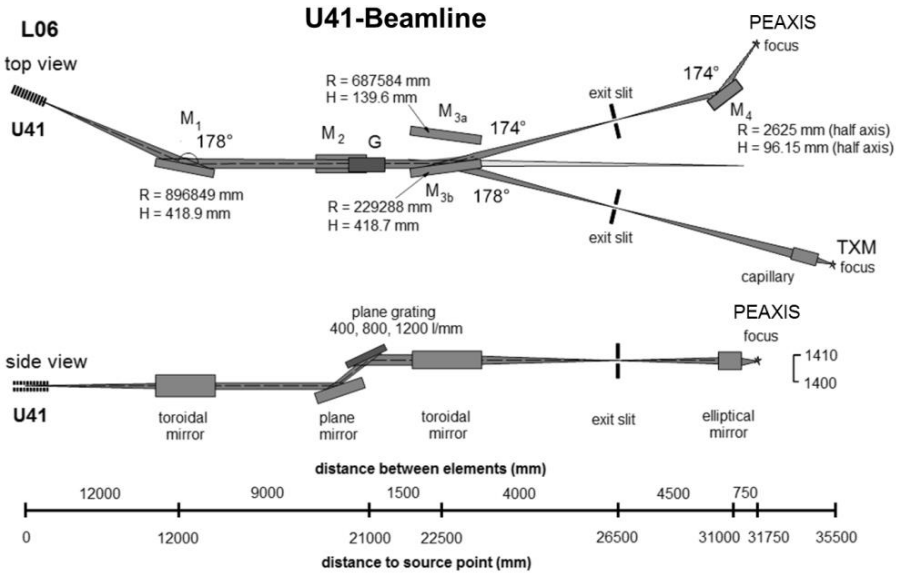

Figure A4 Optical layout of U41-PEAXIS beamline at BESSY II synchrotron facility. Downloaded from [229].

The BL3U beamline at UVSOR III is an undulator beamline equipped with a varied-line-spacing (VLS) PGM for various spectroscopic investigations in the soft X-ray range. Photon energies range from 60 to 800 eV can be provided. The beamline has two experimental stations, XES setup and multi-purpose setup. The transmission mode XAS of CDs aqueous dispersions shown in Chapter 4 were measured at the experimental stage of the multi-purpose setup. [230]

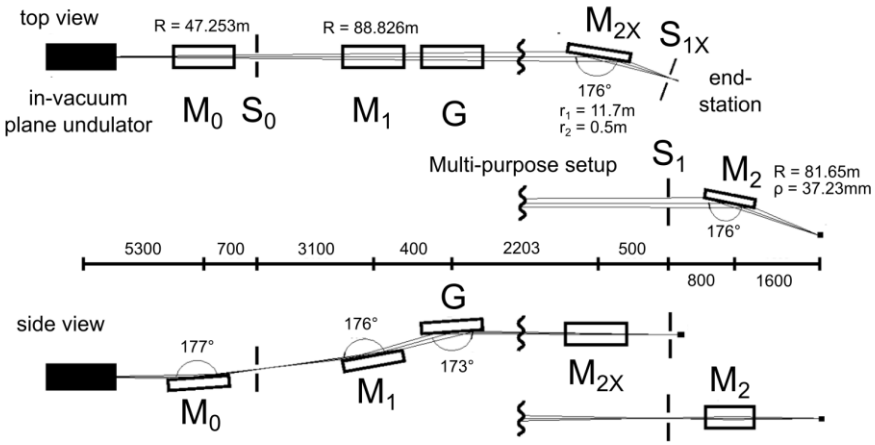

Figure A5 Optical layout of the BL3U beamline at UVSOR-III synchrotron facility. S1X and M2X can be replaced with the other exit slit S1 so that experiments can be carried out at different end stations. Downloaded from [230].

Appendix

LiXEdrom station at BESSY II[*] is designed to perform XAS, XES and RIXS on the materials in both solid states and liquid environment. The solid measurements and liquid flow-cell experiment using LiXEdrom have already been introduced in this dissertation.

"To preserve the ultra-high vacuum conditions required for soft X-ray experiments the LiXEdrom station is equipped with multi-stage pumping, liquid nitrogen cryo-traps and pinholes that reduce the effective pressure by several orders of magnitude. In the main chamber the vacuum of 1×10^{-5}–5×10^{-7} mbar is normally maintained, in the detector chamber is 1×10^{-8}, while at the connection to the beamline the pressure is 5×10^{-9} mbar.

The X-ray spectrometer operates at grazing incidence angle and Rowland circle geometry. It is equipped with four gratings that cover the whole soft X-ray energy range from 30 to 1200 eV. To increase further the energy resolution, the spectrometer is operated at higher diffraction orders. The detector consists of a stack of micro-channel plates (MCP), a phosphorous screen, and a charge coupled device (CCD). The MCP plates have a very small pore size of 5 μm and a small bias angle in order to increase spatial/energy resolution and detection efficiency at the CCD. They are coated with a thin film of cesium iodide to increase the number of secondary electrons and to enhance the overall detection efficiency."

Figure A6 LiXEdrom station in BESSY II synchrotron facility for XAS and RIXS measurements on solids as well as in liquids. Photo was taken by Ronny Golnak, and the permission to use is acknowledged.

[*] The text in italics in the quotation marks is copied from HZB web page [231].

PEAXIS station at BESSY II * is a new experimental station for XPS and RIXS measurements on samples in both liquid and solid states. The RIXS results on solid PCN materials has already discussed in this dissertation.

"The RIXS setup combines high energy resolution with a wide range of momentum transfers. A continuous range of momentum transfers is made possible thanks to the continuous sweep of the five-meter analyzer arm in a range of 106.5 degrees. Two precision spherical gratings (2400 lines/mm) with variable line separations allow measurement of photon energies over a range of 200–1200 eV. Two manipulators that facilitate RIXS and ARPES over temperature ranges of 20–300 K or 300–1000 K are available.

Moreover, utilization of photonic and electronic microfluidic cells in the sample chamber of PEAXIS permits advanced development of technologies mirroring actual applications. To increase the efficiency of photocatalytic and electrocatalytic water splitting, it is necessary for example to study local chemical reactions at the interfaces. To accomplish this, transient molecular states over different timescales must be identified and followed."

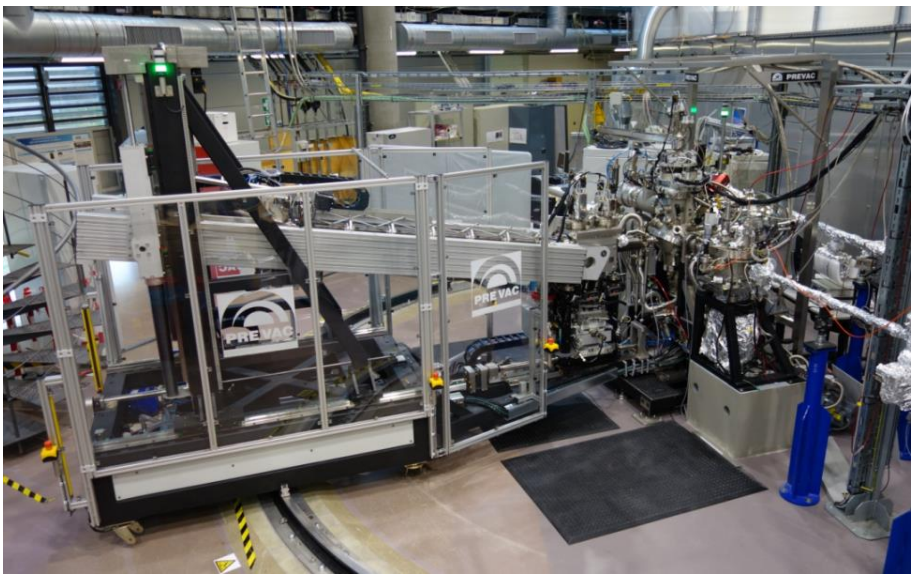

Figure A7 PEAXIS station in BESSY II synchrotron facility for RIXS and ARPES measurements on solids as well as in liquids. Photo was taken by Christian Schulz, and the permission to use is acknowledged.

* The text in italics in the quotation marks is copied from HZB web page [232].

Appendix IV Materials Preparation

Samples studied in Chapter 4 were provided by Reisner's group in University of Cambridge and the synthesis has been performed according to ref. [51,141]. "*Three CDs were synthesized by pyrolysis of organic precursors. g-N-CD were synthesized by the thermal decomposition of aspartic acid in air at 320°C for 100 h. Dissolution in water with addition of NaOH aqueous solution (5 mol/L) produced a dark brown solution. The solid product was isolated as a brown powder by freeze-drying.*"‡ "*Citric acid was used to synthesize the undoped CDs. Citric acid was pyrolyzed in air at 180°C for 40 h producing a-CD. If further increased the temperature to 320°C and maintained for 100 h, g-CD would be synthesized. The purification steps before freeze-drying were similar to that for g-N-CD preparation.*"§

Samples studied in Chapter 5 were provided by Wang's group in Fuzhou University and the synthesis has been performed according to ref. [65,196]. "*S-PCN were prepared via the co-polymerization of melamine and trithiocyanuric acid. 0.75 g melamine and 1 g trithiocyanuric acid were added in 10 mL deionized water and then stirred for 10 min. The mixture was heated to 600°C at a rate of 6°C/min, and maintained for 4 h under the flowing nitrogen atmosphere. The reference samples PCN(S) were synthesized using melamine in the same condition.*"** "*To synthesis of Fe-PCN, 1 g dicyandiamide and 0.1 g $FeCl_3$ mixed with 5 mL deionized water was heated and stirred at 80°C. The reddish mixtures were then heated to 600°C at a rate of 6°C/min, and maintained at this temperature for 4 h in a flowing-nitrogen atmosphere. This was followed by cooling the sample naturally to room temperature with nitrogen gas. The corresponding reference PCN(Fe) were synthesized from the thermal-polymerization of dicyandiamide with the same calcining conditions.*" ††

Samples studied in Chapter 6 were provided by Zhang's group in Tianjin University and the synthesis has been performed according to ref. [69]. "*CNB was first synthesized by the thermal-polymerization of melamine. 5 g of melamine powder was placed in a porcelain boat with a cover and subsequently heated to 500°C for 2 h, then to 520°C for another 2 h at the heating rate of 2°C/min. The obtained product was ground into powder using an agate mortar and then transfer transferred into a tube furnace. The sample was first heated to 520°C at a rate of 2°C/min and held for 8 h under the flowing air (200 SCCM), and then flowed NH_3 (200 SCCM) for another 1 h. After cooling to the room temperature, the final product was obtained and named as CNPS-NH_2. The porous oxygen-rich carbon nitride nanosheets (CNPS-O) were synthesized under the same procedure as CNPS-NH_2 without the NH_3 treatment stage.*"‡‡

‡ The text in italics in the quotation marks is copied from the supporting information of ref. [51].
§ The text in italics in the quotation marks is copied from the supporting information of ref. [141].
** The text in italics in the quotation marks is copied from the supporting information of ref. [196].
†† The text in italics in the quotation marks is copied from the supporting information of ref. [65].
‡‡ The text in italics in the quotation marks is copied from the supporting information of ref. [69].

Appendix V Fitting Details of Oxygen K-edge Transmission-XA Spectra

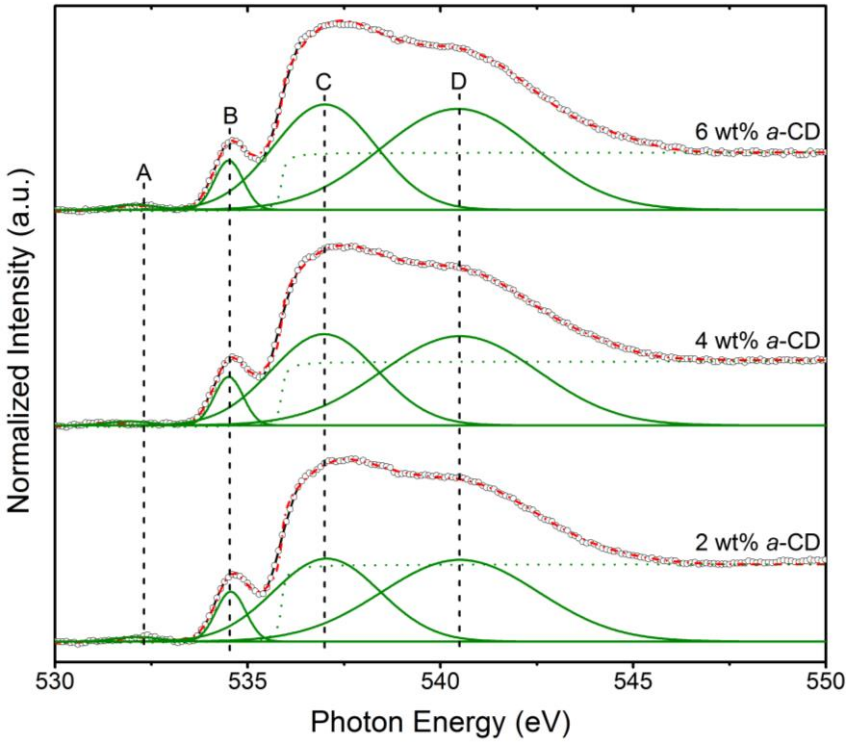

Figure A8 Deconvolution of the O K-edge transmission mode XA spectra of *a*-CD dispersions at different concentration. The different Gaussian peaks (solid), the resulting fit (dash dot) and the background (dot) are shown below the experimental spectra.

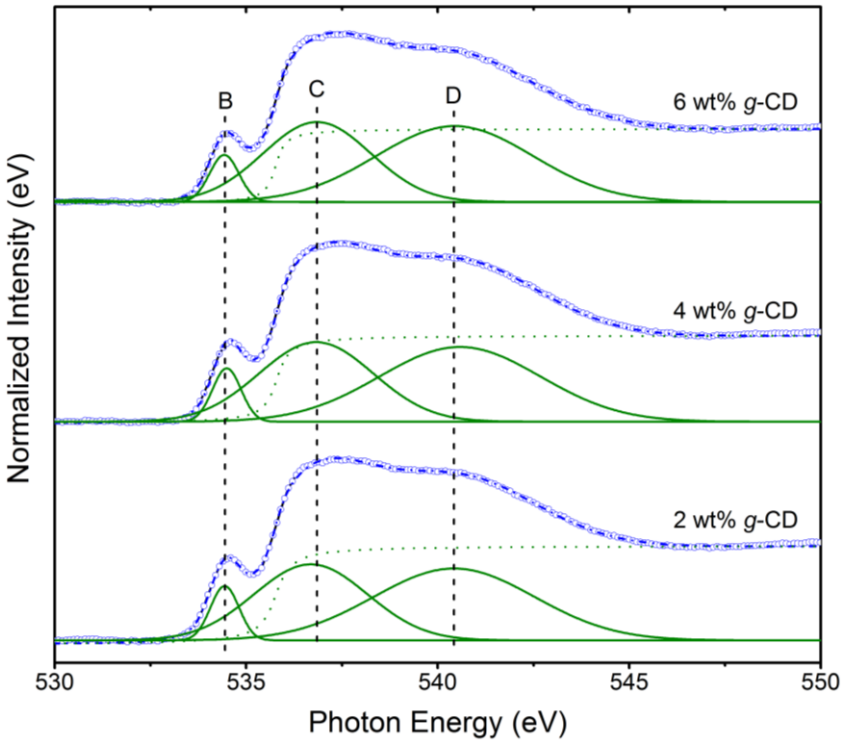

Figure A9 Deconvolution of the O K-edge transmission mode XA spectra of *g*-CD dispersions at different concentration. The line types in the spectra are same as that shown in Figure A8.

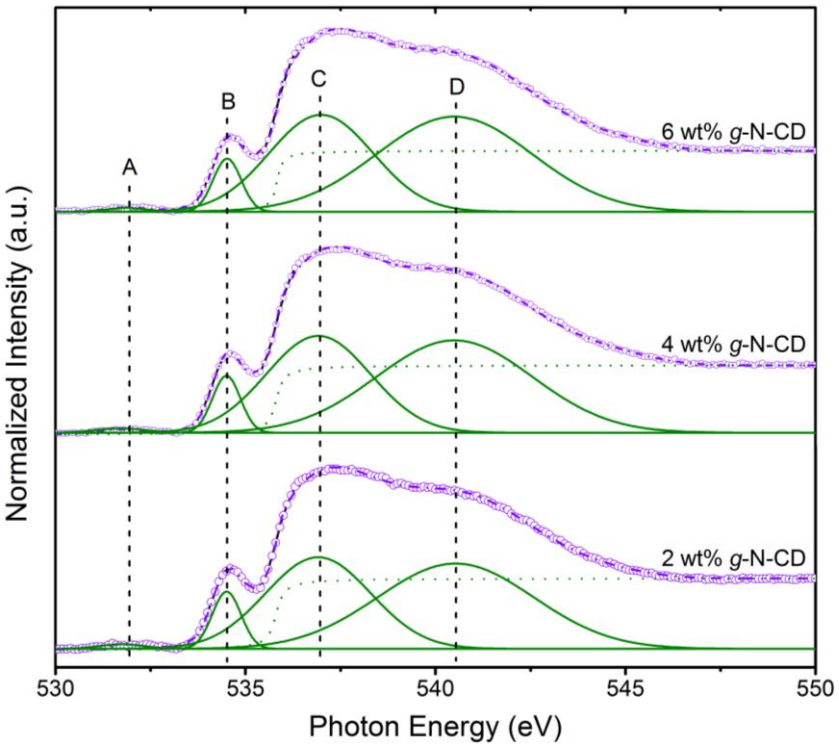

Figure A10 Deconvolution of the O K-edge transmission mode XA spectra of *g*-N-CD dispersions at different concentration. The line types in the spectra are same as that shown in Figure A8.

Table A2 Fitting details of the O K edge transmission mode XA spectra of CDs samples and water.[a)]

Sample	Peak A			Peak B			Peak C			Peak D			Pre/Main edge [%][b)]
	Energy [eV]	FWHM [eV]	Area	Energy [eV]	FWHM [eV]	Area	Energy [eV]	FWHM [eV]	Area	Energy [eV]	FWHM [eV]	Area	
8 wt% *a*-CD	532.16	1.14	0.0160	534.50	0.87	0.0982	536.96	3.28	0.7982	540.48	4.95	1.1271	12.3
6 wt% *a*-CD	532.15	1.15	0.0183	534.50	0.87	0.1130	536.96	3.28	0.8612	540.48	4.95	1.2471	13.1
4 wt% *a*-CD	532.11	1.21	0.0156	534.50	0.87	0.1213	536.96	3.28	0.8381	540.49	4.94	1.2156	14.5
2 wt% *a*-CD	532.16	1.17	0.0159	534.51	0.88	0.1183	536.96	3.27	0.7030	540.49	4.97	1.0217	16.8
8 wt% *g*-CD		/		534.51	0.86	0.1524	536.99	3.28	1.0030	540.50	4.95	1.5256	15.2
6 wt% *g*-CD		/		534.50	0.87	0.1621	536.99	3.29	1.0153	540.49	4.96	1.3988	15.9
4 wt% *g*-CD		/		534.50	0.87	0.2132	536.96	3.30	1.2699	540.51	4.95	1.6776	16.8
2 wt% *g*-CD		/		534.51	0.87	0.2284	536.96	3.29	1.2685	540.49	4.95	1.6976	18.0
8 wt% *g*-N-CD	532.15	1.14	0.0318	534.51	0.87	0.2156	536.98	3.26	1.5294	540.51	4.95	2.2405	14.1
6 wt% *g*-N-CD	532.16	1.15	0.0311	534.51	0.87	0.1440	536.98	3.27	0.9756	540.50	4.95	1.4360	14.8
4 wt% *g*-N-CD	532.15	1.14	0.0303	534.51	0.87	0.1426	536.96	3.27	0.9036	540.49	4.95	1.2879	15.8
2 wt% *g*-N-CD	532.15	1.14	0.0304	534.51	0.87	0.1473	536.97	3.28	0.8636	540.49	4.95	1.1898	17.1
water		/		534.51	0.87	0.1366	536.98	3.28	0.7007	540.49	4.94	1.0723	19.5

[a)] This table contains all samples shown in Chapter 4.

[b)] This is calculated from the area ratio of Peak B and Peak C.

Bibliography

[1] C. F. Shih, T. Zhang, J. Li, and C. Bai, Powering the Future with Liquid Sunshine. Joule **2**, 1925 (2018).

[2] N. S. Lewis, Artificial Photosynthesis. American Scientist **83**, 534 (1995).

[3] D. Gust, T. A. Moore, and A. L. Moore, Solar Fuels via Artificial Photosynthesis. Acc. Chem. Res. **42**, 1890 (2009).

[4] K. Sivula and R. van de Krol, Semiconducting Materials for Photoelectrochemical Energy Conversion. Nat. Rev. Mater. **1**, 15010 (2016).

[5] F. E. Osterloh, Inorganic Nanostructures for Photoelectrochemical and Photocatalytic Water Splitting. Chem. Soc. Rev. **42**, 2294 (2013).

[6] K. Ariga, Q. Ji, T. Mori, M. Naito, Y. Yamauchi, H. Abe, and J. P. Hill, Enzyme Nanoarchitectonics: Organization and Device Application. Chem. Soc. Rev. **42**, 6322 (2013).

[7] A. J. Bard and M. A. Fox, Artificial Photosynthesis: Solar Splitting of Water to Hydrogen and Oxygen. Acc. Chem. Res. **28**, 141 (1995).

[8] N. S. Lewis and D. G. Nocera, Powering the Planet: Chemical Challenges in Solar Energy Utilization. Proc. Natl. Acad. Sci. U. S. A. **103**, 15729 (2006).

[9] J. Barber, Photosynthetic Energy Conversion: Natural and Artificial. Chem. Soc. Rev. **38**, 185 (2009).

[10] R. E. Blankenship, D. M. Tiede, J. Barber, G. W. Brudvig, G. Fleming, M. Ghirardi, M. R. Gunner, W. Junge, D. M. Kramer, A. Melis, T. A. Moore, C. C. Moser, D. G. Nocera, A. J. Nozik, D. R. Ort, W. W. Parson, R. C. Prince, and R. T. Sayre, Comparing Photosynthetic and Photovoltaic Efficiencies and Recognizing the Potential for Improvement. Science **332**, 805 (2011).

[11] C.-Z. Ning, L. Dou, and P. Yang, Bandgap Engineering in Semiconductor Alloy Nanomaterials with Widely Tunable Compositions. Nat. Rev. Mater. **2**, 17070 (2017).

[12] H. Tong, S. Ouyang, Y. Bi, N. Umezawa, M. Oshikiri, and J. Ye, Nano-photocatalytic Materials: Possibilities and Challenges. Adv. Mater. **24**, 229 (2012).

[13] S. Rau, M. G. Pfeffer, and R. Staehle, *Chemical Photocatalysis* (2013).

[14] S. Xie, Q. Zhang, G. Liu, and Y. Wang, Photocatalytic and Photoelectrocatalytic Reduction of CO_2 using Heterogeneous Catalysts with Controlled Nanostructures. Chem. Commun. **52**, 35 (2016).

[15] J. Ran, M. Jaroniec, and S.-Z. Qiao, Cocatalysts in Semiconductor-based Photocatalytic CO_2 Reduction: Achievements, Challenges, and Opportunities. Adv. Mater. **30**, 1704649 (2018).

[16] K. Woan, G. Pyrgiotakis, and W. Sigmund, Photocatalytic Carbon Nanotube–TiO_2 Composites. Adv. Mater. **21**, 2233 (2009).

[17] Q. Xiang, J. Yu, and M. Jaroniec, Graphene-based Semiconductor Photocatalysts. Chem. Soc. Rev. **41**, 782 (2012).

[18] A. A. Popov, S. Yang, and L. Dunsch, Endohedral Fullerenes. Chem. Rev. **113**, 5989 (2013).

[19] D. Zhu, L. Zhang, R. E. Ruther, and R. J. Hamers, Photo-illuminated Diamond as a Solid-state Source of Solvated Electrons in Water for Nitrogen Reduction. Nat. Mater. **12**, 836 (2013).

[20] A. K. Geim and K. S. Novoselov, The Rise of Graphene. Nat. Mater. **6**, 183 (2007).

[21] Y. Zhu, S. Murali, W. Cai, X. Li, J. W. Suk, J. R. Potts, and R. S. Ruoff, Graphene and Graphene Oxide: Synthesis, Properties, and Applications. Adv. Mater. **22**, 3906 (2010).

[22] X.-Y. Zhang, H.-P. Li, X.-L. Cui, and Y. Lin, J. Graphene/TiO_2 Nanocomposites: Synthesis, Characterization and Application in Hydrogen Evolution from Water Photocatalytic Splitting. Mater. Chem. **20**, 2801 (2010).

[23] W. Tu, Y. Zhou, Q. Liu, S. Yan, S. Bao, X. Wang, M. Xiao, and Z. Zou, An *in situ* Simultaneous Reduction-hydrolysis Technique for Fabrication of TiO_2–Graphene 2D Sandwich-like Hybrid Nanosheets: Graphene-promoted Selectivity of Photocatalytic-Driven Hydrogenation and Coupling of CO_2 into Methane and Ethane. Adv. Funct. Mater. **23**, 1743 (2013).

[24] Q. Xiang, J. Yu, and M. Jaroniec, Synergetic Effect of MoS_2 and Graphene as Cocatalysts for Enhanced Photocatalytic H_2 Production Activity of TiO_2 Nanoparticles. J. Am. Chem. Soc. **134**, 6575 (2012).

[25] K. A. S. Fernando, S. Sahu, Y. Liu, W. K. Lewis, E. A. Guliants, A. Jafariyan, P. Wang, C. E. Bunker, and Y.-P. Sun, Carbon Quantum Dots and Applications in Photocatalytic Energy Conversion. ACS Appl. Mater. Interfaces **7**, 8363 (2015).

[26] H. Yu, R. Shi, Y. Zhao, G. I. N. Waterhouse, L.-Z. Wu, C.-H. Tung, and T. Zhang, Smart Utilization of Carbon Dots in Semiconductor Photocatalysis. Adv. Mater. **28**, 9454 (2016).

[27] G. A. M. Hutton, B. C. M. Martindale, and E. Reisner, Carbon Dots as Photosensitisers for Solar-driven Catalysis. Chem. Soc. Rev. **46**, 6111 (2017).

[28] E. L. Wolf, Graphene: A New Paradigm in Condensed Matter and Device Physics. **7**,

320 (2013).

[29] J. Zhang, Z. Xia, and L. Dai, Carbon-based Electrocatalysts for Advanced Energy Conversion and Storage. Sci. Adv. **1**, e1500564 (2015).

[30] H.-X. Wang, Q. Wang, K.-G. Zhou, and H.-L. Zhang, Graphene in Light: Design, Synthesis and Applications of Photo-active Graphene and Graphene-like Materials. Small **9**, 1266 (2013).

[31] Q. Tang, Z. Zhou, and Z. Chen, Graphene-related Nanomaterials: Tuning Properties by Functionalization. Nanoscale **5**, 4541 (2013).

[32] S. N. Baker and G. A. Baker, Luminescent Carbon Nanodots: Emergent Nanolights. Angew. Chemie Int. Ed. **49**, 6726 (2010).

[33] H. Li, Z. Kang, Y. Liu, and S.-T. Lee, Carbon Nanodots: Synthesis, Properties and Applications. J. Mater. Chem. **22**, 24230 (2012).

[34] S. Zhu, Y. Song, X. Zhao, J. Shao, J. Zhang, and B. Yang, The Photoluminescence Mechanism in Carbon Dots (Graphene Quantum Dots, Carbon Nanodots, and Polymer Dots): Current State and Future Perspective. Nano Res. **8**, 355 (2015).

[35] L. Xiao and H. Sun, Novel Properties and Applications of Carbon Nanodots. Nanoscale Horiz. **3**, 565 (2018).

[36] S. Zhu, Y. Song, J. Shao, X. Zhao, and B. Yang, Non-conjugated Polymer Dots with Crosslink-Enhanced Emission in the Absence of Fluorophore Units. Angew. Chemie Int. Ed. **54**, 14626 (2015).

[37] X. Xu, R. Ray, Y. Gu, H. J. Ploehn, L. Gearheart, K. Raker, and W. A. Scrivens, Electrophoretic Analysis and Purification of Fluorescent Single-walled Carbon Nanotube Fragments. J. Am. Chem. Soc. **126**, 12736 (2004).

[38] K. Holá, Y. Zhang, Y. Wang, E. P. Giannelis, R. Zboril, and A. L. Rogach, Carbon Dots—Emerging Light Emitters for Bioimaging, Cancer Therapy and Optoelectronics. Nano Today **9**, 590 (2014).

[39] S. Zhu, Q. Meng, L. Wang, J. Zhang, Y. Song, H. Jin, K. Zhang, H. Sun, H. Wang, and B. Yang, Highly Photoluminescent Carbon Dots for Multicolor Patterning, Sensors, and Bioimaging. Angew. Chemie Int. Ed. **52**, 3953 (2013).

[40] A. M. Chizhik, S. Stein, M. O. Dekaliuk, C. Battle, W. Li, A. Huss, M. Platen, I. A. T. Schaap, I. Gregor, A. P. Demchenko, C. F. Schmidt, J. Enderlein, and A. I. Chizhik, Super-resolution Optical Fluctuation Bio-imaging with Dual-color Carbon Nanodots. Nano Lett. **16**, 237 (2016).

[41] W. F. Zhang, H. Zhu, S. F. Yu, and H. Y. Yang, Observation of Lasing Emission from Carbon Nanodots in Organic Solvents. Adv. Mater. **24**, 2263 (2012).

[42] X. Zhang, Y. Zhang, Y. Wang, S. Kalytchuk, S. V Kershaw, Y. Wang, P. Wang, T. Zhang, Y. Zhao, H. Zhang, T. Cui, Y. Wang, J. Zhao, W. W. Yu, and A. L. Rogach, Color-switchable Electroluminescence of Carbon Dot Light-emitting Diodes. ACS Nano **7**, 11234 (2013).

[43] S. Ghosh, A. M. Chizhik, N. Karedla, M. O. Dekaliuk, I. Gregor, H. Schuhmann, M. Seibt, K. Bodensiek, I. A. T. Schaap, O. Schulz, A. P. Demchenko, J. Enderlein, and A. I. Chizhik, Photoluminescence of Carbon Nanodots: Dipole Emission Centers and Electron–Phonon Coupling. Nano Lett. **14**, 5656 (2014).

[44] J. Liu, Y. Liu, N. Liu, Y. Han, X. Zhang, H. Huang, Y. Lifshitz, S.-T. Lee, J. Zhong, and Z. Kang, Metal-free Efficient Photocatalyst for Stable Visible Water Splitting via a Two-electron Pathway. Science **347**, 970 (2015).

[45] G. A. M. Hutton, B. Reuillard, B. C. M. Martindale, C. A. Caputo, C. W. J. Lockwood, J. N. Butt, and E. Reisner, Carbon Dots as Versatile Photosensitizers for Solar-driven Catalysis with Redox Enzymes. J. Am. Chem. Soc. **138**, 16722 (2016).

[46] H. Li, X. He, Z. Kang, H. Huang, Y. Liu, J. Liu, S. Lian, C. H. A. Tsang, X. Yang, and S.-T. Lee, Water-soluble Fluorescent Carbon Quantum Dots and Photocatalyst Design. Angew. Chemie Int. Ed. **49**, 4430 (2010).

[47] H. Li, R. Liu, Y. Liu, H. Huang, H. Yu, H. Ming, S. Lian, S.-T. Lee, and Z. Kang, Carbon Quantum Dots/Cu_2O Composites with Protruding Nanostructures and Their Highly Efficient (Near) Infrared Photocatalytic Behavior. J. Mater. Chem. **22**, 17470 (2012).

[48] J. Wang, Y.-F. Lim, and G. Wei Ho, Carbon-ensemble-manipulated ZnS Heterostructures for Enhanced Photocatalytic H_2 Evolution. Nanoscale **6**, 9673 (2014).

[49] L. Cao, S. Sahu, P. Anilkumar, C. E. Bunker, J. Xu, K. A. S. Fernando, P. Wang, E. A. Guliants, K. N. Tackett, and Y.-P. Sun, Nanoparticles as Visible-light Photocatalysts for Efficient CO_2 Conversion and Beyond. J. Am. Chem. Soc. **133**, 4754 (2011).

[50] T.-F. Yeh, C.-Y. Teng, S.-J. Chen, and H. Teng, Nitrogen-doped Graphene Oxide Quantum Dots as Photocatalysts for Overall Water-splitting under Visible Light Illumination. Adv. Mater. **26**, 3297 (2014).

[51] B. C. M. Martindale, G. A. M. Hutton, C. A. Caputo, S. Prantl, R. Godin, J. R. Durrant, and E. Reisner, Enhancing Light Absorption and Charge Transfer Efficiency in Carbon Dots through Graphitization and Core Nitrogen Doping. Angew. Chemie **129**, 6559 (2017).

[52] X. Wang, K. Maeda, A. Thomas, K. Takanabe, G. Xin, J. M. Carlsson, K. Domen, and M. Antonietti, A Metal-free Polymeric Photocatalyst for Hydrogen Production from

Water under Visible Light. Nat. Mater. **8**, 76 (2009).

[53] X. Wang, K. Maeda, X. Chen, K. Takanabe, K. Domen, Y. Hou, X. Fu, and M. Antonietti, Polymer Semiconductors for Artificial Photosynthesis: Hydrogen Evolution by Mesoporous Graphitic Carbon Nitride with Visible Light. J. Am. Chem. Soc. **131**, 1680 (2009).

[54] K. Maeda, X. Wang, Y. Nishihara, D. Lu, M. Antonietti, and K. Domen, Photocatalytic Activities of Graphitic Carbon Nitride Powder for Water Reduction and Oxidation under Visible Light. J. Phys. Chem. C **113**, 4940 (2009).

[55] H. Wang, L. Zhang, Z. Chen, J. Hu, S. Li, Z. Wang, J. Liu, and X. Wang, Semiconductor Heterojunction Photocatalysts: Design, Construction, and Photocatalytic Performances. Chem. Soc. Rev. **43**, 5234 (2014).

[56] F. Su, S. C. Mathew, G. Lipner, X. Fu, M. Antonietti, S. Blechert, and X. Wang, *mpg*-C_3N_4-catalyzed Selective Oxidation of Alcohols Using O_2 and Visible Light. J. Am. Chem. Soc. **132**, 16299 (2010).

[57] F. Su, S. C. Mathew, L. Möhlmann, M. Antonietti, X. Wang, and S. Blechert, Aerobic Oxidative Coupling of Amines by Carbon Nitride Photocatalysis with Visible Light. Angew. Chemie Int. Ed. **50**, 657 (2011).

[58] J. Qin, S. Wang, H. Ren, Y. Hou, and X. Wang, Photocatalytic Reduction of CO_2 by Graphitic Carbon Nitride Polymers Derived from Urea and Barbituric Acid. Appl. Catal. B Environ. **179**, 15146 (2015).

[59] R. Kuriki, K. Sekizawa, O. Ishitani, and K. Maeda, Visible-light-driven CO_2 Reduction with Carbon Nitride: Enhancing the Activity of Ruthenium Catalysts. Angew. Chemie Int. Ed. **54**, 2406 (2015).

[60] P. Huang, J. Huang, S. A. Pantovich, A. D. Carl, T. G. Fenton, C. A. Caputo, R. L. Grimm, A. I. Frenkel, and G. Li, Selective CO_2 Reduction Catalyzed by Single Cobalt Sites on Carbon Nitride under Visible-Light Irradiation. J. Am. Chem. Soc. **140**, 16042 (2018).

[61] G. Zhang, Z.-A. Lan, L. Lin, S. Lin, and X. Wang, Overall Water Splitting by Pt/*g*-C_3N_4 Photocatalysts without Using Sacrificial Agents. Chem. Sci. **7**, 3062 (2016).

[62] D. Zheng, X.-N. Cao, and X. Wang, Precise Formation of a Hollow Carbon Nitride Structure with a Janus Surface to Promote Water Splitting by Photoredox Catalysis Angew. Chemie Int. Ed. **55**, 11512 (2016).

[63] Z. Pan, Y. Zheng, F. Guo, P. Niu, and X. Wang, Decorating CoP and Pt Nanoparticles on Graphitic Carbon Nitride Nanosheets to Promote Overall Water Splitting by Conjugated Polymers. ChemSusChem **1**, 87(2017).

[64] F. K. Kessler, Y. Zheng, D. Schwarz, C. Merschjann, W. Schnick, X. Wang, and M. J. Bojdys, Functional Carbon Nitride Materials—Design Strategies for Electrochemical Devices. Nat. Rev. Mater. **2**, 17030 (2017).

[65] X. Wang, X. Chen, A. Thomas, X. Fu, and M. Antonietti, Metal-containing Carbon Nitride Compounds: A New Functional Organic–Metal Hybrid Material. Adv. Mater. **21**, 1609 (2009).

[66] J. Zhang, J. Sun, K. Maeda, K. Domen, P. Liu, M. Antonietti, X. Fu, and X. Wang, Sulfur-mediated Synthesis of Carbon Nitride: Band-gap Engineering and Improved Functions for Photocatalysis. Energy Environ. Sci. **4**, 675 (2011).

[67] P. Niu, L. Zhang, G. Liu, and H.-M. Cheng, Graphene-like Carbon Nitride Nanosheets for Improved Photocatalytic Activities. Adv. Funct. Mater. **22**, 4763 (2012).

[68] G. Liu, T. Wang, H. Zhang, X. Meng, D. Hao, K. Chang, P. Li, T. Kako, and J. Ye, Nature-inspired Environmental "Phosphorylation" Boosts Photocatalytic H_2 Production over Carbon Nitride Nanosheets under Visible-light Irradiation. Angew. Chemie Int. Ed. **54**, 13561 (2015).

[69] N. Meng, J. Ren, Y. Liu, Y. Huang, T. Petit, and B. Zhang, Engineering Oxygen-containing and Amino Groups into Two-dimensional Atomically-thin Porous Polymeric Carbon Nitride for Enhanced Photocatalytic Hydrogen Production. Energy Environ. Sci. **11**, 566 (2018).

[70] F. de Groot and A. Kotani, *Core Level Spectroscopy of Solids* (CRC Press, 2008).

[71] M. A. Bañares, M. O. Guerrero-Pérez, J. L. G. Fierro, and G. G. Cortez, Raman Spectroscopy during Catalytic Operations with Online Activity Measurement (*Operando* Spectroscopy): A Method for Understanding the Active Centres of Cations Supported on Porous Materials. J. Mater. Chem. **12**, 3337 (2002).

[72] A. Chakrabarti, M. E. Ford, D. Gregory, R. Hu, C. J. Keturakis, S. Lwin, Y. Tang, Z. Yang, M. Zhu, M. A. Bañares, and I. E. Wachs, A Decade of *Operando* Spectroscopy studies. Catal. Today **283**, 27 (2017).

[73] J. Dou, Z. Sun, A. A. Opalade, N. Wang, W. Fu, and F. (Feng) Tao, *Operando* Chemistry of Catalyst Surfaces during Catalysis. Chem. Soc. Rev. **46**, 2001 (2017).

[74] J.-M. Andanson and A. Baiker, Exploring Catalytic Solid/Liquid Interfaces by *in situ* Attenuated Total Reflection Infrared Spectroscopy. Chem. Soc. Rev. **39**, 4571 (2010).

[75] B. L. Mojet, S. D. Ebbesen, and L. Lefferts, Light at the Interface: The Potential of Attenuated Total Reflection Infrared Spectroscopy for Understanding Heterogeneous Catalysis in Water. Chem. Soc. Rev. **39**, 4643 (2010).

[76] F. Zaera, New Advances in the Use of Infrared Absorption Spectroscopy for the

Characterization of Heterogeneous Catalytic Reactions. Chem. Soc. Rev. **43**, 7624 (2014).

[77] Sapling Learning. Electromagnetic Spectrum. Available at: http://sites.google.com/site/chempendix/em-spectrum.

[78] G. Kirchhoff and R. Bunsen, Chemische Analyse durch Spectralbeobachtungen. Ann. Der Phys. Und Chemie **110**, 161 (1860).

[79] D. B. Brace, P. Prévost, B. Stewart, G. Kirchhoff, and R. Bunsen, *The Laws of Radiation and Absorption: Memoirs by Prévost, Stewart, Kirchhoff and Bunsen* (American Book Company, 1901).

[80] W. C. Röntgen, Ueber eine neue Art von Strahlen. Ueber eine neue Art von Strahlen. Ann. Phys. **300**, 12 (1898).

[81] A. Lindegaard-Andersen and L. Gerward, Röntgen centenary—100 years of X-rays. Radiat. Phys. Chem. **46**, 299 (1995).

[82] A. H. Compton, Quantum Theory of the Scattering of X-rays by Light Elements. Phys. Rev. **21**, 483 (1923).

[83] Y. H. Woo, The Distribution of Energy between the Modified and the Unmodified Rays in the Compton Effect. Phys. Rev. **27**, 119 (1926).

[84] M. F. L'Annunziata, *Radioactivity: Introduction and History, From the Quantum to Quarks* (Elsevier Science, 2016).

[85] H. Hertz, Ueber einen Einfluss des ultravioletten Lichtes auf die electrische Entladung. Ann. Phys. **267**, 983 (1887).

[86] W. Hallwachs, Ueber den Einfluss des Lichtes auf electrostatisch geladene Körper. Ann. Phys. **269**, 301 (1888).

[87] S. Hüfner, *Photoelectron Spectroscopy: Principles and Applications* (Springer, 2003).

[88] M. P. Seah and W. A. Dench, Quantitative Electron Spectroscopy of Surfaces: A Standard Data Base for Electron Inelastic Mean Free Paths in Solids. Surf. Interface Anal. **1**, 2 (1979).

[89] M. Tasumi, *Introduction to Experimental Infrared Spectroscopy: Fundamentals and Practical Methods* (Wiley, 2014).

[90] H. Wiedemann, *Synchrotron Radiation* (Springer, 2003).

[91] F. Lin, Y. Liu, X. Yu, L. Cheng, A. Singer, O. G. Shpyrko, H. L. Xin, N. Tamura, C. Tian, T.-C. Weng, X.-Q. Yang, Y. S. Meng, D. Nordlund, W. Yang, and M. M. Doeff, Synchrotron X-ray Analytical Techniques for Studying Materials Electrochemistry in Rechargeable Batteries. Chem. Rev. **117**, 13123 (2017).

[92] The Center for X-ray Optics. X-ray Attenuation Length. Available at: http://henke.lbl.gov/optical_constants/atten2.html.

[93] J. Stöhr, *NEXAFS Spectroscopy* (Springer-Verlag: New York, New York, 1992).

[94] Wikipedia. Comparison of Auger yield and fluorescence yield as a function of atomic number. Available at: http:// https://en.wikipedia.org/wiki/File:Auger_Yield.svg.

[95] A. Kotani and S. Shin, Resonant Inelastic X-ray Scattering Spectra for Electrons in Solids. Rev. Mod. Phys. **73**, 203 (2001).

[96] R. Jenkins, R. Manne, R. Robin, and C. Senemaud, IUPAC—Nomenclature System for X-ray Spectroscopy. X-ray Spectrom. **20**, 149 (1991).

[97] Helmholtz-zentrum Berlin für Materialien und Energie, The Plane Grating Monochromator Beamline U49-2_PGM-1 at BESSY II. J. Large-Scale Res. Facil. **72**, 2 (2016).

[98] K. J. S. Sawhney, F. Senf, M. Scheer, F. Schäfers, J. Bahrdt, A. Gaupp, and W. Gudat, A Novel Undulator-based PGM Beamline for Circularly Polarised Synchrotron Radiation at BESSY II. Nucl. Instruments Methods Phys. Res. Sect. A Accel. Spectrometers, Detect. Assoc. Equip. **390**, 395 (1997).

[99] R. Seidel, B. Winter, and S. E. Bradforth, Valence Electronic Structure of Aqueous Solutions: Insights from Photoelectron Spectroscopy. Annu. Rev. Phys. Chem. **67**, 283 (2016).

[100] T. Fransson, Y. Harada, N. Kosugi, N. A. Besley, B. Winter, J. J. Rehr, L. G. M. Pettersson, and A. Nilsson, X-ray and Electron Spectroscopy of Water. Chem. Rev. **116**, 7551 (2016).

[101] J. W. Smith and R. J. Saykally, Soft X-ray Absorption Spectroscopy of Liquids and Solutions. Chem. Rev. **117**, 13909 (2017).

[102] M. F. Tesch, S. A. Bonke, T. E. Jones, M. N. Shaker, J. Xiao, K. Skorupska, R. Mom, J. Melder, P. Kurz, A. Knop-Gericke, R. Schlögl, R. K. Hocking, and A. N. Simonov, Evolution of Oxygen–Metal Electron Transfer and Metal Electronic States during Manganese Oxide Catalyzed Water Oxidation Revealed with *in situ* Soft X-ray Spectroscopy. Angew. Chemie Int. Ed. **58**, 3426 (2019).

[103] D. Schön, J. Xiao, R. Golnak, M. F. Tesch, B. Winter, J.-J. Velasco-Velez, and E. F. Aziz, Introducing Ionic-current Detection for X-ray Absorption Spectroscopy in Liquid Cells. J. Phys. Chem. Lett. **8**, 2087 (2017).

[104] D. Schön, R. Golnak, M. F. Tesch, B. Winter, J.-J. Velasco-Velez, E. F. Aziz, and J. Xiao, Bulk-sensitive Detection of the Total Ion Yield for X-ray Absorption Spectroscopy in Liquid Cells. J. Phys. Chem. Lett. **8**, 5136 (2017).

[105] M. Nagasaka, T. Hatsui, T. Horigome, Y. Hamamura, and N. Kosugi, Development of a Liquid Flow Cell to Measure Soft X-ray Absorption in Transmission Mode: A Test for

Liquid Water. J. Electron Spectros. Relat. Phenomena **177**, 130 (2010).

[106] N. Yamamoto, H. Zen, M. Hosaka, T. Konomi, M. Adachi, K. Hayashi, J. Yamazaki, Y. Takashima, and M. Katoh, Beam Injection with Pulsed Multipole Magnet at UVSOR-III. Nucl. Instruments Methods Phys. Res. Sect. A Accel. Spectrometers, Detect. Assoc. Equip. **767**, 26 (2014).

[107] T. Hatsui, E. Shigemasa, and N. Kosugi, Design of a Transmission Grating Spectrometer and an Undulator Beamline for Soft X-ray Emission Studies. AIP Conf. Proc. **705**, 921 (2004).

[108] M. Nagasaka, K. Mochizuki, V. Leloup, and N. Kosugi, Local Structures of Methanol–Water Binary Solutions Studied by Soft X-ray Absorption Spectroscopy. J. Phys. Chem. B **118**, 4388 (2014).

[109] M. Nagasaka, H. Yuzawa, T. Horigome, and N. Kosugi, Reliable Absorbance Measurement of Liquid Samples in Soft X-ray Absorption Spectroscopy in Transmission Mode. J. Electron Spectros. Relat. Phenomena **224**, 93 (2018).

[110] Y. Harada, T. Tokushima, Y. Horikawa, O. Takahashi, H. Niwa, M. Kobayashi, M. Oshima, Y. Senba, H. Ohashi, K. T. Wikfeldt, A. Nilsson, L. G. M. Pettersson, and S. Shin, Selective Probing of the OH or OD Stretch Vibration in Liquid Water Using Resonant Inelastic Soft X-ray Scattering. Phys. Rev. Lett. **111**, 193001 (2013).

[111] A. Pietzsch, F. Hennies, P. S. Miedema, B. Kennedy, J. Schlappa, T. Schmitt, V. N. Strocov, and A. Föhlisch, Snapshots of the Fluctuating Hydrogen Bond Network in Liquid Water on the Sub-femtosecond Timescale with Vibrational Resonant Inelastic X-ray Scattering. Phys. Rev. Lett. **114**, 88302 (2015).

[112] S. Schreck, A. Pietzsch, B. Kennedy, C. Såthe, P. S. Miedema, S. Techert, V. N. Strocov, T. Schmitt, F. Hennies, J.-E. Rubensson, and A. Föhlisch, Ground State Potential Energy Surfaces Around Selected Atoms from Resonant Inelastic X-ray Scattering. Sci. Rep. **6**, 20054 (2016).

[113] N. Ignatova, V. V da Cruz, R. C. Couto, E. Ertan, M. Odelius, H. Ågren, F. F. Guimarães, A. Zimin, S. P. Polyutov, F. Gel'mukhanov, and V. Kimberg, Infrared-pump–X-ray-probe Spectroscopy of Vibrationally Excited Molecules. Phys. Rev. A **95**, 42502 (2017).

[114] K. M. Lange, R. Könnecke, S. Ghadimi, R. Golnak, M. A. Soldatov, K. F. Hodeck, A. Soldatov, and E. F. Aziz, High Resolution X-ray Emission Spectroscopy of Water and Aqueous Ions Using the Micro-jet Technique. Chem. Phys. **377**, 1 (2010).

[115] Helmholtz-zentrum Berlin für Materialien und Energie, LiXEdrom: High Energy Resolution RIXS Station Dedicated to Liquid Investigation at BESSY II. J. Large-Scale

Res. Facil. **2**, 1 (2016).

[116] K. Lieutenant, T. Hofmann, C. Schulz, M. V Yablonskikh, K. Habicht, and E. F. Aziz, Design Concept of the High-resolution End-station PEAXIS at BESSY II: Wide-Q-range RIXS and XPS Measurements on Solids, Solutions, and Interfaces. J. Electron Spectros. Relat. Phenomena **210**, 54 (2016).

[117] K. Lieutenant, T. Hofmann, C. Zendler, C. Schulz, E. F. Aziz, and K. Habicht, Numerical Optimization of a RIXS Spectrometer Using Raytracing Simulations. J. Phys. Conf. Ser. **738**, 12104 (2016).

[118] F. Reinert and S. Hüfner, Photoemission Spectroscopy—from Early Days to Recent Applications. New J. Phys. **7**, 97 (2005).

[119] G. Svehla, *Ultraviolet Photoelectron and Photoion Spectroscopy, Auger Electron Spectroscopy, Plasma Excitation in Spectrochemical Analysis* (1979).

[120] Helmholtz-zentrum Berlin für Materialien und Energie, CISSY : A Station for Preparation and Surface/Interface Analysis of Thin Film Materials and Devices. J. Large-Scale Res. Facil. **2**, 4 (2016).

[121] Helmholtz-zentrum Berlin für Materialien und Energie, Schematic drawing of the CISSY machine. Available at: https://www.helmholtz-berlin.de/pubbin/igama_output?modus=datei&did=629.

[122] N. B. Colthup, L. H. Daly, and S. E. Wiberley, *Introduction to Infrared and Raman Spectroscopy (Third Edition)* (1990).

[123] P. R. Griffiths and J. A. de Haseth, *Fourier Transform Infrared Spectrometry* (John Wiley & Sons, 2007).

[124] K. A. Ritter and J. W. Lyding, The Influence of Edge Structure on the Electronic Properties of Graphene Quantum Dots and Nanoribbons. Nat. Mater. **8**, 235 (2009).

[125] S. Zhu, J. Zhang, S. Tang, C. Qiao, L. Wang, H. Wang, X. Liu, B. Li, Y. Li, W. Yu, X. Wang, H. Sun, and B. Yang, Surface Chemistry Routes to Modulate the Photoluminescence of Graphene Quantum Dots: From Fluorescence Mechanism to Up-Conversion Bioimaging Applications. Adv. Funct. Mater. **22**, 4732 (2012).

[126] Y. Wang, S. Kalytchuk, Y. Zhang, H. Shi, S. V Kershaw, and A. L. Rogach, Thickness-dependent Full-color Emission Tunability in a Flexible Carbon Dot Ionogel. J. Phys. Chem. Lett. **5**, 1412 (2014).

[127] S. K. Cushing, M. Li, F. Huang, and N. Wu, Origin of Strong Excitation Wavelength Dependent Fluorescence of Graphene Oxide. ACS Nano **8**, 1002 (2014).

[128] D. Qu, M. Zheng, J. Li, Z. Xie, and Z. Sun, Tailoring Color Emissions from N-doped Graphene Quantum Dots for Bioimaging Applications. Light Sci. Appl. **4**, e364 (2015).

[129] Q. Songnan, Z. Ding, L. Di, J. Wenyu, J. Pengtao, H. Dong, L. Lei, Z. Haibo, and S. Dezhen, Toward Efficient Orange Emissive Carbon Nanodots through Conjugated sp^2-Domain Controlling and Surface Charges Engineering. Adv. Mater. **28**, 3516 (2016).

[130] V. Strauss, J. T. Margraf, C. Dolle, B. Butz, T. J. Nacken, J. Walter, W. Bauer, W. Peukert, E. Spiecker, T. Clark, and D. M. Guldi, Carbon Nanodots: Toward a Comprehensive Understanding of Their Photoluminescence. J. Am. Chem. Soc. **136**, 17308 (2014).

[131] D. Pan, J. Zhang, Z. Li, and M. Wu, Hydrothermal Route for Cutting Graphene Sheets into Blue-Luminescent Graphene Quantum Dots. Adv. Mater. **22**, 734 (2010).

[132] S. Wang, I. S. Cole, D. Zhao, and Q. Li, The Dual Roles of Functional Groups in the Photoluminescence of Graphene Quantum Dots. Nanoscale **8**, 7449 (2016).

[133] J. Zhong, H. Zhang, X. Sun, and S.-T. Lee, Synchrotron Soft X-ray Absorption Spectroscopy Study of Carbon and Silicon Nanostructures for Energy Applications. Adv. Mater. **26**, 7786 (2014).

[134] H. Ding, S.-B. Yu, J.-S. Wei, and H.-M. Xiong, Full-color Light-emitting Carbon Dots with a Surface-state-controlled Luminescence Mechanism. ACS Nano **10**, 484 (2016).

[135] T. Zhang, J. Zhu, Y. Zhai, H. Wang, X. Bai, B. Dong, H. Wang, and H. Song, A Novel Mechanism for Red Emission Carbon Dots: Hydrogen Bond Dominated Molecular States Emission. Nanoscale **9**, 13042 (2017).

[136] T. Petit, L. Puskar, T. A. Dolenko, S. Choudhury, E. Ritter, S. Burikov, K. Laptinskiy, Q. Brzustowski, U. Schade, H. Yuzawa, M. Nagasaka, N. Kosugi, M. Kurzyp, A. Venerosy, H. A. Girard, J.-C. Arnault, E. Osawa, N. Nunn, O. Shenderova, and E. F. Aziz, Unusual Water Hydrogen Bond Network around Hydrogenated Nanodiamonds. J. Phys. Chem. C **121**, 5185 (2017).

[137] J. Ren, F. Weber, F. Weigert, Y. Wang, S. Choudhury, J. Xiao, I. Lauermann, U. Resch-Genger, A. Bande, and T. Petit, Influence of Surface Chemistry on Optical, Chemical and Electronic Properties of Blue Luminescent Carbon Dots. Nanoscale **11**, 2056 (2019).

[138] H. Ding and H.-M. Xiong, Exploring the Blue Luminescence Origin of Nitrogen-doped Carbon Dots by Controlling the Water Amount in Synthesis. RSC Adv. **5**, 66528 (2015).

[139] J.-J. Max and C. Chapados, Infrared Spectroscopy of Aqueous Carboxylic Acids: Comparison between Different Acids and Their Salts. J. Phys. Chem. A **108**, 3324 (2004).

[140] F. Wang, Z. Xie, H. Zhang, C. Liu, and Y. Zhang, Highly Luminescent Organosilane-functionalized Carbon Dots. Adv. Funct. Mater. **21**, 1027 (2011).

[141] B. C. M. Martindale, G. A. M. Hutton, C. A. Caputo, and E. Reisner, Solar Hydrogen Production Using Carbon Quantum Dots and a Molecular Nickel Catalyst. J. Am. Chem.

Soc. **137**, 6018 (2015).

[142] B. Nie, J. Stutzman, and A. Xie, Biophys. A Vibrational Spectral Maker for Probing the Hydrogen-Bonding Status of Protonated Asp and Glu Residues. J. **88**, 2833 (2005).

[143] F. Weber, J. Ren, T. Petit, and A. Bande, A. Theoretical X-ray Absorption Spectroscopy Database Analysis for Oxidised 2D Carbon Nanomaterials. Phys. Chem. Chem. Phys. **21**, 6999 (2019).

[144] C.-H. Chuang, Y.-F. Wang, Y.-C. Shao, Y.-C. Yeh, D.-Y. Wang, C.-W. Chen, J. W. Chiou, S. C. Ray, W. F. Pong, L. Zhang, J. F. Zhu, and J. H. Guo, The Effect of Thermal Reduction on the Photoluminescence and Electronic Structures of Graphene Oxides. Sci. Rep. **4**, 4525 (2014).

[145] V. Lee, L. Whittaker, C. Jaye, K. M. Baroudi, D. A. Fischer, and S. Banerjee, Large-area Chemically Modified Graphene Films: Electrophoretic Deposition and Characterization by Soft X-ray Absorption Spectroscopy. Chem. Mater. **21**, 3905 (2009).

[146] H.-K. Jeong, H.-J. Noh, J.-Y. Kim, M. H. Jin, C. Y. Park, and Y. H. Lee, X-ray Absorption Spectroscopy of Graphite Oxide. EPL (Europhysics Lett.) **82**, 67004 (2008).

[147] C.-H. Chuang, S. C. Ray, D. Mazumder, S. Sharma, A. Ganguly, P. Papakonstantinou, J.-W. Chiou, H.-M. Tsai, H.-W. Shiu, C.-H. Chen, H.-J. Lin, J. Guo, and W.-F. Pong, Chemical Modification of Graphene Oxide by Nitrogenation: An X-ray Absorption and Emission Spectroscopy Study. Sci. Rep. **7**, 42235 (2017).

[148] R. P. Gandhiraman, D. Nordlund, C. Javier, J. E. Koehne, B. Chen, and M. Meyyappan, X-ray Absorption Study of Graphene Oxide and Transition Metal Oxide Nanocomposites. J. Phys. Chem. C **118**, 18706 (2014).

[149] D. Pacilé, M. Papagno, A. F. Rodríguez, M. Grioni, L. Papagno, Ç. Ö. Girit, J. C. Meyer, G. E. Begtrup, and A. Zettl, Near-edge X-ray Absorption Fine-structure Investigation of Graphene. Phys. Rev. Lett. **101**, 66806 (2008).

[150] D. A. Outka, J. Stöhr, R. J. Madix, H. H. Rotermund, B. Hermsmeier, and J. Solomon, NEXAFS Studies of Complex Alcohols and Carboxylic Acids on the Si(111)(7×7). Surf. Sci. **185**, 53 (1987).

[151] A. Ganguly, S. Sharma, P. Papakonstantinou, and J. Hamilton, Probing the Thermal Deoxygenation of Graphene Oxide Using High-resolution *in situ* X-ray-based Spectroscopies. J. Phys. Chem. C **115**, 17009 (2011).

[152] D. Pacilé, J. C. Meyer, A. Fraile Rodríguez, M. Papagno, C. Gómez-Navarro, R. S. Sundaram, M. Burghard, K. Kern, C. Carbone, and U. Kaiser, Electronic Properties and Atomic Structure of Graphene Oxide Membranes. Carbon **49**, 966 (2011).

[153] J. MacNaughton, A. Moewes, and E. Z. Kurmaev, Electronic Structure of the

Nucleobases. J. Phys. Chem. B **109**, 7749 (2005).

[154] X. Liang, Y. Wang, H. Zheng, and Z. Wu, X-ray Absorption Spectroscopy Study on the Thermal and Hydrazine Reduction of Graphene Oxide. J. Electron Spectros. Relat. Phenomena **196**, 89 (2014).

[155] H. Ding, J.-S. Wei, N. Zhong, Q.-Y. Gao, and H.-M. Xiong, Highly Efficient Red-Emitting Carbon Dots with Gram-Scale Yield for Bioimaging. Langmuir **33**, 12635 (2017).

[156] Y.-L. Huang, H.-W. Tien, C.-C. M. Ma, S.-Y. Yang, S.-Y. Wu, H.-Y. Liu, and Y.-W. Mai, Effect of Extended Polymer Chains on Properties of Transparent Graphene Nanosheets Conductive Film. J. Mater. Chem. **21**, 18236 (2011).

[157] D. Yang, A. Velamakanni, G. Bozoklu, S. Park, M. Stoller, R. D. Piner, S. Stankovich, I. Jung, D. A. Field, C. A. Ventrice, and R. S. Ruoff, Chemical Analysis of Graphene Oxide Films after Heat and Chemical Treatments by X-ray Photoelectron and Micro Raman Spectroscopy. Carbon **47**, 145 (2009).

[158] E. Desimoni, G. I. Casella, A. Morone, and A. M. Salvi, XPS Determination of Oxygen-containing Functional Groups on Carbon-fibre Surfaces and the Cleaning of These Surfaces. Surf. Interface Anal. **15**, 627 (1990).

[159] S. D. Gardner, C. S. K. Singamsetty, G. L. Booth, G.-R. He, and C. U. Pittman, Surface Characterization of Carbon Fibers Using Angle-resolved XPS and ISS. Carbon **33**, 587 (1995).

[160] H. Ding, J.-S. Wei, and H.-M. Xiong, Nitrogen and Sulfur Co-doped Carbon Dots with Strong Blue Luminescence. Nanoscale **6**, 13817 (2014).

[161] H. Liu, T. Ye, and C. Mao, Fluorescent Carbon Nanoparticles Derived from Candle Soot. Angew. Chemie Int. Ed. **46**, 6473 (2007).

[162] E. J. McDermott, E. Z. Kurmaev, T. D. Boyko, L. D. Finkelstein, R. J. Green, K. Maeda, K. Domen, and A. Moewes, Structural and Band Gap Investigation of GaN:ZnO Heterojunction Solid Solution Photocatalyst Probed by Soft X-ray Spectroscopy. J. Phys. Chem. C **116**, 7694 (2012).

[163] L. Zhang, N. Schwertfager, T. Cheiwchanchamnangij, X. Lin, P.-A. Glans-Suzuki, L. F. J. Piper, S. Limpijumnong, Y. Luo, J. F. Zhu, W. R. L. Lambrecht, and J.-H. Guo, Electronic Band Structure of Graphene from Resonant Soft X-ray Spectroscopy: The Role of Core-hole Effects. Phys. Rev. B **86**, 245430 (2012).

[164] W. T. Hong, K. A. Stoerzinger, B. Moritz, T. P. Devereaux, W. Yang, and Y. Shao-Horn, Probing $LaMO_3$ Metal and Oxygen Partial Density of States Using X-ray Emission, Absorption, and Photoelectron Spectroscopy. J. Phys. Chem. C **119**, 2063 (2015).

[165] K. Holá, M. Sudolská, S. Kalytchuk, D. Nachtigallová, A. L. Rogach, M. Otyepka, and R. Zbořil, Graphitic Nitrogen Triggers Red Fluorescence in Carbon Dots. ACS Nano **11**, 12402 (2017).

[166] D. Usachov, O. Vilkov, A. Grüneis, D. Haberer, A. Fedorov, V. K. Adamchuk, A. B. Preobrajenski, P. Dudin, A. Barinov, M. Oehzelt, C. Laubschat, and D. V Vyalikh, Nitrogen-Doped Graphene: Efficient Growth, Structure, and Electronic Properties. Nano Lett. **11**, 5401 (2011).

[167] M. Laporta, M. Pegoraro, and L. Zanderighi, Perfluorosulfonated Membrane (Nafion): FTIR Study of the State of Water with Increasing Humidity. Phys. Chem. Chem. Phys. **1**, 4619 (1999).

[168] D. B. Asay and S. H. Kim, Evolution of the Adsorbed Water Layer Structure on Silicon Oxide at Room Temperature. J. Phys. Chem. B **109**, 16760 (2005).

[169] J.-B. Brubach, A. Mermet, A. Filabozzi, A. Gerschel, and P. Roy, Signatures of the Hydrogen Bonding in the Infrared Bands of Water. J. Chem. Phys. **122**, 184509 (2005).

[170] D. B. Asay, A. L. Barnette, and S. H. Kim, Effects of Surface Chemistry on Structure and Thermodynamics of Water Layers at Solid−Vapor Interfaces. J. Phys. Chem. C **113**, 2128 (2009).

[171] A. Anderson and W. R. Ashurst, Interfacial Water Structure on a Highly Hydroxylated Silica Film. Langmuir **25**, 11549 (2009).

[172] P. Hobza and Z. Havlas, Blue-Shifting Hydrogen Bonds. Chem. Rev. **100**, 4253 (2000).

[173] L. George and W. Sander, Matrix Isolation Infrared and ab initio Study of the Hydrogen Bonding between Formic Acid and Water. Spectrochim. Acta Part A Mol. Biomol. Spectrosc. **60**, 3225 (2004).

[174] X. Miao, D. Qu, D. Yang, B. Nie, Y. Zhao, H. Fan, and Z. Sun, Synthesis of Carbon Dots with Multiple Color Emission by Controlled Graphitization and Surface Functionalization. Adv. Mater. **30**, 1704740 (2017).

[175] Q.-L. Zhao, Z.-L. Zhang, B.-H. Huang, J. Peng, M. Zhang, and D.-W. Pang, Facile Preparation of Low Cytotoxicity Fluorescent Carbon Nanocrystals by Electrooxidation of Graphite. Chem. Commun. 5116 (2008).

[176] A. Sciortino, E. Marino, B. van Dam, P. Schall, M. Cannas, and F. Messina, Solvatochromism Unravels the Emission Mechanism of Carbon Nanodots. J. Phys. Chem. Lett. **7**, 3419 (2016).

[177] S. Bai, W. Jiang, Z. Li, and Y. Xiong, Surface and Interface Engineering in Photocatalysis. ChemNanoMat **1**, 223 (2015).

[178] M. Freiwald, S. Cramm, W. Eberhardt, and S. Eisebitt, Soft X-ray Absorption

Spectroscopy in Liquid Environments. J. Electron Spectros. Relat. Phenomena **137–140**, 413 (2004).

[179] T. Petit, J. Ren, S. Choudhury, R. Golnak, S. S. N. Lalithambika, M. F. Tesch, J. Xiao, and E. F. Aziz, Absorption Spectroscopy of TiO_2 Nanoparticles in Water Using a Holey Membrane-based Flow Cell. Adv. Mater. Interfaces **4**, 1700755 (2017).

[180] J. Ren, D. S. Achilleos, R. Golnak, H. Yuzawa, J. Xiao, M. Nagasaka, E. Reisner and T. Petit, Uncovering the Charge Transfer between Carbon Dots and Water by *in situ* Soft X-ray Absorption Spectroscopy. J. Phys. Chem. Lett. **14**, 3843 (2019).

[181] C. D. Cappa, J. D. Smith, K. R. Wilson, and R. J. Saykally, Revisiting the Total Ion Yield X-ray Absorption Spectra of Liquid Water Microjets. J. Phys. Condens. Matter **20**, 205105 (2008).

[182] L. Xi, M. Schellenberger, R. F. Präg, R. Golnak, G. Schuck, and K. M. Lange, Ionic Current Mn K-edge X-ray Absorption Spectra Obtained in a Flow Cell. J. Phys. Chem. C **122**, 15588 (2018).

[183] P. Wernet, D. Nordlund, U. Bergmann, M. Cavalleri, M. Odelius, H. Ogasawara, L. Å. Näslund, T. K. Hirsch, L. Ojamäe, P. Glatzel, L. G. M. Pettersson, and A. Nilsson, The Structure of the First Coordination Shell in Liquid Water. Science **304**, 995 (2004).

[184] J. D. Smith, C. D. Cappa, K. R. Wilson, B. M. Messer, R. C. Cohen, and R. J. Saykally, Energetics of Hydrogen Bond Network Rearrangements in Liquid Water. Science **306**, 851 (2004).

[185] C. D. Cappa, J. D. Smith, K. R. Wilson, B. M. Messer, M. K. Gilles, R. C. Cohen, and R. J. Saykally, Effects of Alkali Metal Halide Salts on the Hydrogen Bond Network of Liquid Water. J. Phys. Chem. B **109**, 7046 (2005).

[186] T. Petit, H. Yuzawa, M. Nagasaka, R. Yamanoi, E. Osawa, N. Kosugi, and E. F. Aziz, Probing Interfacial Water on Nanodiamonds in Colloidal Dispersion. J. Phys. Chem. Lett. **6**, 2909 (2015).

[187] S. C. Ray, H. M. Tsai, J. W. Chiou, B. Bose, J. C. Jan, K. Kumar, W. F. Pong, D. Dasgupta, and M.-H. Tsai, X-ray Absorption Spectroscopy (XAS) Study of Dip Deposited a-C:H(OH) Thin Films. J. Phys. Condens. Matter **16**, 5713 (2004).

[188] W. Ding, Z. Wei, S. Chen, X. Qi, T. Yang, J. Hu, D. Wang, L.-J. Wan, S. F. Alvi, and L. Li, Space-confinement-Induced Synthesis of Pyridinic- and Pyrrolic-nitrogen-doped Graphene for the Catalysis of Oxygen Reduction. Angew. Chemie Int. Ed. **52**, 11755 (2013).

[189] D. Guo, R. Shibuya, C. Akiba, S. Saji, T. Kondo, and J. Nakamura, Active Sites of Nitrogen-doped Carbon Materials for Oxygen Reduction Reaction Clarified Using

Model Catalysts. Science **351**, 361 (2016).

[190] S. Bhattacharyya, F. Ehrat, P. Urban, R. Teves, R. Wyrwich, M. Döblinger, J. Feldmann, A. S. Urban, and J. K. Stolarczyk, Effect of Nitrogen Atom Positioning on the Trade-off between Emissive and Photocatalytic Properties of Carbon Dots. Nat. Commun. **8**, 1401 (2017).

[191] J. S. Tse, D. M. Shaw, D. D. Klug, S. Patchkovskii, G. Vankó, G. Monaco, and M. Krisch, X-ray Raman Spectroscopic Study of Water in the Condensed Phases. Phys. Rev. Lett. **100**, 95502 (2008).

[192] A. Nilsson, D. Nordlund, I. Waluyo, N. Huang, H. Ogasawara, S. Kaya, U. Bergmann, L.-Å. Näslund, H. Öström, P. Wernet, K. J. Andersson, T. Schiros, and L. G. M. Pettersson, X-ray Absorption Spectroscopy and X-ray Raman Scattering of Water and Ice: An Experimental View. J. Electron Spectros. Relat. Phenomena **177**, 99 (2010).

[193] B. Jana, S. Pal, and B. Bagchi, Hydrogen Bond Breaking Mechanism and Water Reorientational Dynamics in the Hydration Layer of Lysozyme. J. Phys. Chem. B **112**, 9112 (2008).

[194] Y. Zheng, L. Lin, B. Wang, and X. Wang, Graphitic Carbon Nitride Polymers toward Sustainable Photoredox Catalysis. Angew. Chemie Int. Ed. **54**, 12868 (2015).

[195] G. Liu, P. Niu, C. Sun, S. C. Smith, Z. Chen, G. Q. (Max) Lu, and H.-M. Cheng, Unique Electronic Structure Induced High Photoreactivity of Sulfur-doped Graphitic C_3N_4. J. Am. Chem. Soc. **132**, 11642 (2010).

[196] L.-L. Feng, Y. Zou, C. Li, S. Gao, L.-J. Zhou, Q. Sun, M. Fan, H. Wang, D. Wang, G.-D. Li, and X. Zou, Nanoporous Sulfur-doped Graphitic Carbon Nitride Microrods: A Durable Catalyst for Visible-light-driven H_2 Evolution. Int. J. Hydrogen Energy **39**, 15373 (2014).

[197] J. Hong, X. Xia, Y. Wang, and R. Xu, Mesoporous Carbon Nitride with *in situ* Sulfur Doping for Enhanced Photocatalytic Hydrogen Evolution from Water under Visible Light. J. Mater. Chem. **22**, 15006 (2012).

[198] Y. Li, S. Ouyang, H. Xu, X. Wang, Y. Bi, Y. Zhang, and J. Ye, Constructing Solid–Gas-interfacial Fenton Reaction over Alkalinized-C_3N_4 Photocatalyst to Achieve Apparent Quantum Yield of 49% at 420 nm. J. Am. Chem. Soc. **138**, 13289 (2016).

[199] L.-F. Gao, T. Wen, J.-Y. Xu, X.-P. Zhai, M. Zhao, G.-W. Hu, P. Chen, Q. Wang, and H.-L. Zhang, Iron-doped Carbon Nitride-type Polymers as Homogeneous Organocatalysts for Visible Light-Driven Hydrogen Evolution. ACS Appl. Mater. Interfaces **8**, 617 (2016).

[200] W. T. Zheng, J. H. Guo, Y. Sakamoto, M. Takaya, X. T. Li, P. J. Chao, Z. S. Jin, K. Z.

Xing, and J.-E. Sundgren, Diam. Chemical Bonding in Carbon Nitride Films Studied by X-ray Spectroscopies. Relat. Mater. **10**, 1897 (2001).

[201] S. C. Ray, C. W. Pao, J. W. Chiou, H. M. Tsai, J. C. Jan, W. F. Pong, R. McCann, S. S. Roy, P. Papakonstantinou, and J. A. McLaughlin, Electronic properties of a-CN_x Thin Films: An X-ray Absorption and Photoemission Spectroscopy Study. J. Appl. Phys. **98**, 33708 (2005).

[202] L. J. P. Ament, M. van Veenendaal, T. P. Devereaux, J. P. Hill, and J. van den Brink, Resonant Inelastic X-ray Scattering Studies of Elementary Excitations. Rev. Mod. Phys. **83**, 705 (2011).

[203] J. A. Carlisle, E. L. Shirley, E. A. Hudson, L. J. Terminello, T. A. Callcott, J. J. Jia, D. L. Ederer, R. C. C. Perera, and F. J. Himpsel, Probing the Graphite Band Structure with Resonant Soft X-ray Fluorescence. Phys. Rev. Lett. **74**, 1234 (1995).

[204] N. Hellgren, J. Guo, Y. Luo, C. Såthe, A. Agui, S. Kashtanov, J. Nordgren, H. Ågren, and J.-E. Sundgren, Electronic Structure of Carbon Nitride Thin Films Studied by X-ray Spectroscopy Techniques. Thin Solid Films **471**, 19 (2005).

[205] M. Magnuson, L. Yang, J.-H. Guo, C. Såthe, A. Agui, J. Nordgren, Y. Luo, H. Ågren, N. Johansson, W. R. Salaneck, L. E. Horsburgh, and A. P. Monkman, Resonant Inelastic Soft X-ray Scattering Spectra at the Nitrogen and Carbon K-edges of Poly(pyridine-2,5-diyl). J. Electron Spectros. Relat. Phenomena **101–103**, 573 (1999).

[206] N. Engel, S. I. Bokarev, E. Suljoti, R. Garcia-Diez, K. M. Lange, K. Atak, R. Golnak, A. Kothe, M. Dantz, O. Kühn, and E. F. Aziz, Chemical Bonding in Aqueous Ferrocyanide: Experimental and Theoretical X-ray Spectroscopic Study. J. Phys. Chem. B **118**, 1555 (2014).

[207] L.-C. Duda, J. Nordgren, G. Dräger, S. Bocharov, and T. Kirchner, Polarized Resonant Inelastic X-ray Scattering from Single-crystal Transition Metal Oxides. J. Electron Spectros. Relat. Phenomena **110–111**, 275 (2000).

[208] J. Miyawaki, S. Suga, H. Fujiwara, M. Urasaki, H. Ikeno, H. Niwa, H. Kiuchi, and Y. Harada, Dzyaloshinskii-Moriya interaction in α-Fe_2O_3 Measured by Magnetic Circular Dichroism In Resonant Inelastic Soft X-ray Scattering. Phys. Rev. B **96**, 214420 (2017).

[209] B. Kempgens, A. Kivimäki, M. Neeb, H. M. Köppe, A. M. Bradshaw, and J. Feldhaus, A High-resolution N 1s Photoionization Study of the Molecule in the Near-threshold Region. J. Phys. B At. Mol. Opt. Phys. **29**, 5389 (1996).

[210] C. Fan, J. Miao, G. Xu, J. Liu, J. Lv, and Y. Wu, Graphitic Carbon Nitride Nanosheets Obtained by Liquid Stripping as Efficient Photocatalysts under Visible Light. RSC Adv. **7**, 37185 (2017).

[211] R. C. Couto, V. V Cruz, E. Ertan, S. Eckert, M. Fondell, M. Dantz, B. Kennedy, T. Schmitt, A. Pietzsch, F. F. Guimarães, H. Ågren, F. Gel'mukhanov, M. Odelius, V. Kimberg, and A. Föhlisch, Selective Gating to Vibrational Modes through Resonant X-ray Scattering. Nat. Commun. **8**, 14165 (2017).

[212] V. Vaz da Cruz, E. Ertan, R. C. Couto, S. Eckert, M. Fondell, M. Dantz, B. Kennedy, T. Schmitt, A. Pietzsch, F. F. Guimarães, H. Ågren, F. Gel'mukhanov, M. Odelius, A. Föhlisch, and V. Kimberg, A Study of the Water Molecule Using Frequency Control over Nuclear Dynamics in Resonant X-ray Scattering. Phys. Chem. Chem. Phys. **19**, 19573 (2017).

[213] Q. Han, B. Wang, J. Gao, Z. Cheng, Y. Zhao, Z. Zhang, and L. Qu, Atomically Thin Mesoporous Nanomesh of Graphitic C_3N_4 for High-efficiency Photocatalytic Hydrogen Evolution. ACS Nano **10**, 2745 (2016).

[214] P. Yang, H. Ou, Y. Fang, and X. Wang, A Facile Steam Reforming Strategy to Delaminate Layered Carbon Nitride Semiconductors for Photoredox Catalysis. Angew. Chemie Int. Ed. **56**, 3992 (2017).

[215] X. Zhang, X. Xie, H. Wang, J. Zhang, B. Pan, and Y. Xie, Enhanced Photoresponsive Ultrathin Graphitic-Phase C_3N_4 Nanosheets for Bioimaging. J. Am. Chem. Soc. **135**, 18 (2013).

[216] S. Guo, Y. Zhu, Y. Yan, Y. Min, J. Fan, and Q. Xu, Holey Structured Graphitic Carbon Nitride Thin Sheets with Edge Oxygen Doping via Photo-Fenton Reaction with Enhanced Photocatalytic Activity. Appl. Catal. B Environ. **185**, 315 (2016).

[217] W. Ma, D. Han, M. Zhou, H. Sun, L. Wang, X. Dong, and L. Niu, Ultrathin *g*-C_3N_4/TiO_2 Composites as Photoelectrochemical Elements for the Real-time Evaluation of Global Antioxidant Capacity. Chem. Sci. **5**, 3946 (2014).

[218] Y. Wang, M. K. Bayazit, S. J. A. Moniz, Q. Ruan, C. C. Lau, N. Martsinovich, and J. Tang, Linker-controlled Polymeric Photocatalyst for Highly Efficient Hydrogen Evolution from Water. Energy Environ. Sci. **10**, 1643 (2017).

[219] D. J. Martin, K. Qiu, S. A. Shevlin, A. D. Handoko, X. Chen, Z. Guo, and J. Tang, Highly Efficient Photocatalytic H_2 Evolution from Water Using Visible Light and Structure-controlled Graphitic Carbon Nitride. Angew. Chemie Int. Ed. **53**, 9240 (2014).

[220] J. Chen, Z. Mao, L. Zhang, D. Wang, R. Xu, L. Bie, and B. D. Fahlman, Nitrogen-deficient Graphitic Carbon Nitride with Enhanced Performance for Lithium Ion Battery Anodes. ACS Nano **11**, 12650 (2017).

[221] J. G. Santaclara, M. A. Nasalevich, S. Castellanos, W. H. Evers, F. C. M. Spoor, K. Rock, L. D. A. Siebbeles, F. Kapteijn, F. Grozema, A. Houtepen, J. Gascon, J. Hunger, and M.

A. van der Veen, Organic Linker Defines the Excited-state Decay of Photocatalytic MIL-125(Ti)-type Materials. ChemSusChem **9**, 388 (2016).

[222] M. B. Chambers, X. Wang, L. Ellezam, O. Ersen, M. Fontecave, C. Sanchez, L. Rozes, and C. Mellot-Draznieks, Maximizing the Photocatalytic Activity of Metal-organic Frameworks with Aminated-functionalized Linkers: Substoichiometric Effects in MIL-125-NH_2. J. Am. Chem. Soc. **139**, 8222 (2017).

[223] P. S. Swain and R. Lipowsky, Contact Angles on Heterogeneous Surfaces: A New Look at Cassie's and Wenzel's Laws. Langmuir **14**, 6772 (1998).

[224] Y. Zheng, Y. Jiao, Y. Zhu, L. H. Li, Y. Han, Y. Chen, A. Du, M. Jaroniec, and S. Z. Qiao, Hydrogen Evolution by a Metal-free Electrocatalyst. Nat. Commun. **5**, 3783 (2014).

[225] W. Che, W. Cheng, T. Yao, F. Tang, W. Liu, H. Su, Y. Huang, Q. Liu, J. Liu, F. Hu, Z. Pan, Z. Sun, and S. Wei, Fast Photoelectron Transfer in (C_{ring})–C_3N_4 Plane Heterostructural Nanosheets for Overall Water Splitting. J. Am. Chem. Soc. **139**, 3021 (2017).

[226] T. Mizokawa, Y. Wakisaka, T. Sudayama, C. Iwai, K. Miyoshi, J. Takeuchi, H. Wadati, D. G. Hawthorn, T. Z. Regier, and G. A. Sawatzky, Role of Oxygen Holes Li_xCoO_2 Revealed by Soft X-ray Spectroscopy. Phys. Rev. Lett. **111**, 56404 (2013).

[227] X. She, J. Wu, J. Zhong, H. Xu, Y. Yang, R. Vajtai, J. Lou, Y. Liu, D. Du, H. Li, and P. M. Ajayan, Oxygenated Monolayer Carbon Nitride for Excellent Photocatalytic Hydrogen Evolution and External Quantum Efficiency. Nano Energy **27**, 138 (2016).

[228] Helmholtz-zentrum Berlin für Materialien und Energie. Optical Layout of U49-2_PGM-1 beamline (2016). Available at: https://www.helmholtz-berlin.de/pubbin/igama_output?modus=einzel&sprache=en&gid=1655&typoid=35517.

[229] Helmholtz-zentrum Berlin für Materialien und Energie. Optical Layout of U41-PEAXIS beamline (2018). Available at: https://www.helmholtz-berlin.de/pubbin/igama_output?modus=einzel&sprache=en&gid=2126&typoid=37587.

[230] Institute for Molecular Science. Optical Layout of the BL3U beamline (2018). Available at: https://www.uvsor.ims.ac.jp/beamlines/3U/ebl3u.html.

[231] Helmholtz-zentrum Berlin für Materialien und Energie. LiXEdrom Station (2018). Available at: https://www.helmholtz-berlin.de/pubbin/igama_output?modus=einzel&sprache=de&gid=1867.

[232] Helmholtz-zentrum Berlin für Materialien und Energie. The PEAXIS beamline (2018). Available at: https://www.helmholtz-berlin.de/ forschung/quellen/zukunft/beamlines/peaxis_en.html.

Glossary

AFM	atomic force microscopy
ATR	attenuated total reflection
CB	conduction band
CBM	conduction band minimum
CCD	charge-coupled device
CD	carbon dots
DFT	density functional theory
EY	electron yield
FTIR	Fourier transform infrared spectroscopy
HER	hydrogen evolution reaction
HOMO	highest occupied molecular orbital
IR	infrared
IMFP	inelastic mean free path
LUMO	lowest unoccupied molecular orbital
MCP	inverse partial fluorescence yield
NMR	nuclear magnetic resonance spectroscopy
PCN	polymeric carbon nitride
PES	photoelectron spectroscopy
PFY	partial fluorescence yield
PL	photoluminescence
PGM	plane grating monochromator
RH	relative humidity
RIXS	resonant inelastic X-ray scattering
SCCM	standard cubic centimeters per minute
SECO	secondary electron cut-off
SEM	solid electrolyte interphase
SHE	standard hydrogen electrode

TEM	transmission electron microscopy
TEY	total electron yield
TIY	total ion yield
TFY	total fluorescence yield
UHV	ultra-high vacuum
UPS	ultraviolet photoelectron spectroscopy
UV	ultraviolet
VB	valence band
VBM	valence band maximum
VUV	vacuum ultraviolet
XA	X-ray absorption
XAS	X-ray absorption spectroscopy
XE	X-ray emission
XES	X-ray emission spectroscopy
XPS	X-ray photoelectron spectroscopy
XRD	X-ray diffraction

List of Figures

List of Tables

Acknowledgements

The past three years at HZB have been an unforgettable and invaluable experience to me. When I first started my doctoral project in 2016, I was a layman in the field of synchrotron soft X-ray spectroscopy. It is unbelievable that over the following years I have actually been doing research with different spectroscopic techniques and making some achievements at different synchrotron facilities. I would not have been able to make this journey without the help and support of many people and I am very grateful to them.

First and foremost, my greatest thanks go to my supervisor Dr. Tristan Petit who gave me the opportunity to work on this research project. He always has a very insightful view about the field while he is also uncommonly detail oriented and understands the nature of the problems very well. More importantly, Tristan is an extremely kind, caring and supportive supervisor that I could not have asked for more. The results and success presented herein are mostly attributed to Tristan, without whom I may have encountered many detours in this journey. I am sincerely grateful to him for his patience and kindness. It is also my great honor to have Prof. Dr. Holger Dau and Prof. Dr. Wolfgang Kuch on my thesis committee. Thanks Holger and Wolfgang for their kind interests in the topics addressed by my work. Their dedication to work and rigorous scholarship inspire me a lot. I thank Dr. Iain Wilkinson, Prof. Dr. Klaus Lips, Prof. Dr. Simone Raoux and Dr. Gabriele Lampert for their great support during the doctoral program.

Collaboration is a big lesson that I have learned, and also a fun part of this doctoral program. The doctoral dissertation is the result of a joint collaboration across Asia and Europe: Federal Institute for Materials Research and Testing (BAM), Fuzhou University (FZU), Lund University, Max Planck Institute of Colloids and Interfaces (MPI), National Institute for Materials Science (NIMS), Tianjin University (TJU), University of Cambridge and UVSOR-III synchrotron facility. I thank my collaborators for providing me high-quality samples: Carbon dots from Dr. Demetra Achilleos and Prof. Dr. Erwin Reisner (Cambridge); Polymeric carbon nitride from Dr. Lin Lihua, Prof. Dr. Wang Xinchen (FZU), Meng Nannan, Prof. Dr. Zhang Bin (TJU), Li Yunxiang and Prof. Dr. Ye Jinhua (NIMS); Nitrogen doped mesoporous carbon from Dr. Martin Oschatz (MPI). I thank Dr. Masanari Nagasaka and Dr. Hayato Yuzawa for hosting me in UVSOR-III synchrotron in Japan, Dr. Ute Resch-Genger and Florian Weigert for helping me with the measurements in BAM. I thank Dr. Guo Meiyuan (Lund) for performing the theoretical simulations for X-ray spectroscopic results of PCN materials.

Moreover, I would like to thank Dr. Ronny Golnak, Dr. Iver Lauermann, Dr. Klaus

Lieutenant, Dr. Natalia Maticiuc, Dr. Ljiljana Puskar, Dr. Eglof Ritter, Dr. Ulrich Schade, Dr. Christian Schulz, Dr. Juan Velasco Vélez, Dr. Wang Yajie, and Dr. Deniz Wong for the kind assistance during the experiment in BESSY II, in particular, Dr. Xiao Jie, who I bothered a lot on the analysis of X-ray spectroscopy data. It was the nice collaboration that made this dissertation more fruitful.

During the doctoral program, I was fortunate to work with many nice people at HZB. Thanks Sneha Choudhury, Dr. Franziska Buchner, Dr. Mailis Maria Lounasvuori, Dr. Christoph Merschjann and Ameer Al-Temimy, for providing me with a lovely experience in the Nanocarbon group, and also for their kind help during the experiments. Thanks Fabian Weber, Karen Mudryk, Hebatallah Ali, Sreeju Sreekantan Nair Lalithambika, Anika Haller, Nataliia Kuzkova and Isheta Majumdar for adding me a lot of fun and giving me a lot of support at various times. I also want to thank Dr. Annika Bande, Dr. Robert Seidel, Dr. Kaan Atak, Dr. Igor Kiyan and Dr. Marc Tesch who shared their profound knowledge and experience on spectroscopic techniques.

The SUCCESS-2017 research school in Les Houches School of Physics with incisive questions, discussions, interactions and the wonderful scenery of Alps was an unforgettable experience for me. I would like to thank the organizers and alumni of "SUCCESS-2017". Many of them have become my good friends afterwards: Fatima Alarab, Dai Ji, Mauro Fanciulli, Huang Sizhao, Kong Lingyuan, Li Jiemin, Natsuki Mitsuishi, Jakob Steinbauer…

Outside of the research in HZB, I have been extremely lucky to be surrounded by many great friends. Just to name a few (and forgive me for not being able to list all of them): Chang Kainan, Dong Kang, Li Qiankun, Niu Yan, Qin Ye, Sun Yuchen, Zhang Heshou, Zhang Zhiyang and Zhu Yuqiao are new friends I met after I came to Berlin, whose companionship helped me adapt to my new—exciting yet disorienting—life in the first months. And the precious friendships keep pulling me out from my stressful research life. I would like to extend my heartfelt gratitude to Xi Lifei, Sun Guoguang and their families. They regard me as a younger brother; provide me not only delicious food, and also insightful suggestions.

Lastly, a special thanks to my family for their unconditional and endless support and encouragement over the duration of my studies. Like most Chinese students in my generation, I am the only child of my parents and I have a very close relationship with them—even if they are living 6 (or 7) hours ahead of me and I can only spare 2 or 3 weeks staying with them every year. My parents made me who I am today and I never know how to pay them back. I hope that they are at least a little proud of me for what I have been through so far.

Ren Jian, August 2019

Curriculum Vitae

For reasons of data protection, the curriculum vitae is not published in the electronic version.

List of Publications

1 Petit, **Ren**, Choudhury, Golnak, Lalithambika, Tesch, Xiao, Aziz, X-Ray absorption spectroscopy of TiO_2 nanoparticles in water using a holey membrane-based flow cell. *Advanced Materials Interfaces* 2017, 4 (23): 1700755

2 Meng*, **Ren***, Liu, Huang, Petit, Zhang, Engineering oxygen-containing and amino groups into two-dimensional atomically-thin porous polymeric carbon nitrogen for enhanced photocatalytic hydrogen production. *Energy & Environmental Science* 2018 (11) 3: 566–571 (*Meng and Ren have equal contribution) **Chapter 6**

3 Choudhury, Kiendl, **Ren**, Gao, Knittel, Nebel, Venerosy, Girard, Arnault, Krueger, Larsson, Petit, Combining nanostructuration with boron doping to alter sub band gap acceptor states in diamond materials. *Journal of Materials Chemistry a* 2018, 34 (6): 16645–16654

4 **Ren**, Weber, Weigert, Wang, Choudhury, Xiao, Lauermann, Resch-Genger, Bande, Petit, Influence of surface chemistry on optical, chemical and electronic properties of blue luminescent carbon dots. *Nanoscale* 2019, (11): 2056–2064 **Chapter 3**

5 Weber, **Ren**, Petit, Bande, Theoretical X-ray absorption spectroscopy database analysis for oxidised 2D carbon nanomaterials. *Physical Chemistry Chemical Physics* 2019 (21): 6999–7008

6 **Ren**, Achilleos, Golnak, Yuzawa, Xiao, Nagasaka, Reisner, Petit, Uncovering the charge transfer between carbon dots photocatalysts with water by *in-situ* soft X-ray absorption spectroscopy. *The Journal Physical Chemistry Letters* 2019, (10): 3843–3848 **Chapter 4**

7 Li, **Ren**, Ouyang, Hou, Petit, Song, Chen, Philo, Kako, Ye, Atomic carbon chains-mediated carriers transfer over polymeric carbon nitride for efficient photocatalysis. *Applied Catalysis B-Environmental* 2019, 259 (15): 118027

Selbstständigkeitserklärung

Hiermit versichere ich, REN Jian, die vorliegende Dissertation mit dem Titel „Understanding the structure–performance relationship of carbon-based photocatalysts by soft X-ray spectroscopy“ selbständig und ohne unerlaubte Hilfe angefertigt zu haben. Bei der Verfassung der Dissertation wurden keine anderen als die im Text aufgeführten Hilfsmittel verwendet.

Ein Promotionsverfahren zu einem früheren Zeitpunkt an einer anderen Hochschule oder bei einem anderen Fachbereich wurden nicht beantragt.

Berlin, den 27.08.2019
REN Jian